

AD-A157 249

EXHAUST PLUME MEASUREMENTS OF 15-POUND BATES (BALLISTIC
TEST AND EVALUATI. (U) AIR FORCE ROCKET PROPULSION LAB
EDWARDS AFB CA J A MISENER ET AL. JUN 85

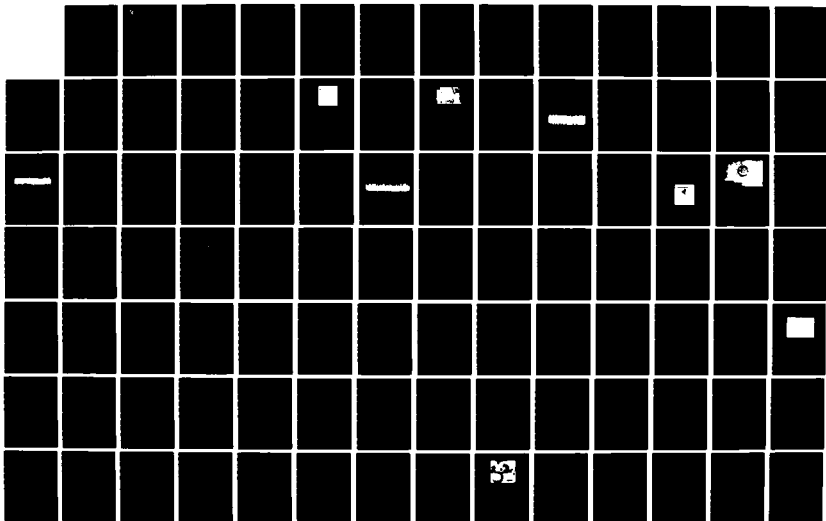
1/2

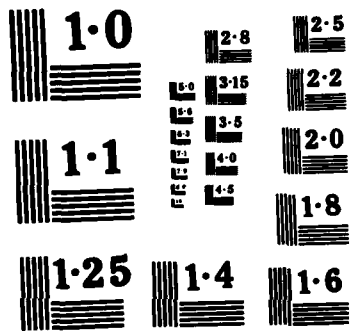
UNCLASSIFIED

AFRPL-TR-85-013

F/G 21/9.2

NL





NATIONAL BUREAU OF STANDARDS
MICROCOPY RESOLUTION TEST CHART

AFRPL TR-85-013

AD:



AD-A157 249

Final Report
for the period
June 1980 to
October 1984

Exhaust Plume Measurements of 15-pound BATES Motors

June 1985

Authors:
J. A. Misener, 1Lt, USAF
P. A. Kessel
T. W. Park

Approved for Public Release

Distribution unlimited. The AFRPL Technical Services Office has reviewed this report, and it is releasable to the National Technical Information Service, where it will be available to the general public, including foreign nationals.

DTIC FILE COPY

**Air Force
Rocket Propulsion
Laboratory**

Air Force Space Technology Center
Space Division, Air Force Systems Command
Edwards Air Force Base,
California 93523-5000



NOTICES

When U. S. Government drawings, specifications, or other data are used for any purpose other than a definitely related Government procurement operation, the Government thereby incurs no responsibility nor any obligation whatsoever, and the fact that the Government may have formulated, furnished, or in any way supplied the said drawings, specifications, or other data is not to be regarded by implication or otherwise, or in any manner licensing the holder or any other person or corporation, or conveying any rights or permission to manufacture, use or sell any patented invention that may in any way be related hereto.

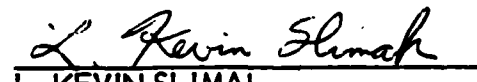
FOREWORD

This final report was submitted under Job Order Number 573010CU with the Air Force Rocket Propulsion Laboratory, Edwards AFB California. The principle author (J. A. M.), wishes to acknowledge the contributions of Drs W. K. McGregor, T. D. McCay and D. M. Mann for conceiving the project and its instrumentation. Capt G. S. Meserve and personnel at Experimental Area 1-32, primarily Sgt J. W. Clark, must be recognized for their work in instrumentation and acquiring the bulk of the data. Finally, J. A. M. wishes to thank Messrs W. D. Hesketh and C. W. Beckman for assistance in interpreting the data.

References in this report to named commercial products are not to be considered in any sense as an endorsement of the product by the United States Air Force or the Government.

This report has been reviewed and approved for publication in accordance with the distribution statement on the cover and DD Form 1473.


JAMES A. MISENER, 2Lt, USAF
Project Manager


L. KEVIN SLIMAK
Chief, Interdisciplinary Space
Technology Branch

FOR THE DIRECTOR


ROBERT L. GEISLER
Deputy Chief, Propulsion Analysis Division

UNCLASSIFIED

SECURITY CLASSIFICATION OF THIS PAGE

REPORT DOCUMENTATION PAGE

1a. REPORT SECURITY CLASSIFICATION UNCLASSIFIED		1b. RESTRICTIVE MARKINGS	
2a. SECURITY CLASSIFICATION AUTHORITY		3. DISTRIBUTION/AVAILABILITY OF REPORT Approved for Public Release. Distribution is Unlimited.	
2b. DECLASSIFICATION/DOWNGRADING SCHEDULE			
4. PERFORMING ORGANIZATION REPORT NUMBER(S) AFRPL-TR-85-013		5. MONITORING ORGANIZATION REPORT NUMBER(S)	
6a. NAME OF PERFORMING ORGANIZATION Air Force Rocket Propulsion Laboratory/Observables Section		6b. OFFICE SYMBOL (If applicable) DYSO	7a. NAME OF MONITORING ORGANIZATION
6c. ADDRESS (City, State and ZIP Code) AFRPL/DYSO, Stop 24 Edwards AFB CA 93523-5000		7b. ADDRESS (City, State and ZIP Code)	
8a. NAME OF FUNDING/SPONSORING ORGANIZATION	8b. OFFICE SYMBOL (If applicable)	9. PROCUREMENT INSTRUMENT IDENTIFICATION NUMBER	
8c. ADDRESS (City, State and ZIP Code)		10. SOURCE OF FUNDING NOS.	
		PROGRAM ELEMENT NO. 62302F	PROJECT NO. 5730
		TASK NO. 10	WORK UNIT NO. CU
11. TITLE (Include Security Classification) Exhaust Plume Measurements of 15-pound BATES Motors (U)			
12. PERSONAL AUTHOR(S) Misener, James A., Coauthors: Kessel, P.A. and Park, T-W.			
13a. TYPE OF REPORT Final	13b. TIME COVERED FROM 80/6 TO 84/10	14. DATE OF REPORT (Yr., Mo., Day) 85/6	15. PAGE COUNT 118
16. SUPPLEMENTARY NOTATION			
17. COSATI CODES		18. SUBJECT TERMS (Continue on reverse if necessary and identify by block number)	
FIELD	GROUP	SUB. GR.	
21	02		plume infrared signature
21	08		plume ultraviolet signature
			plume diagnostics
			plume diagnostics retrieval
			plume particle sizes
			plume particle properties
19. ABSTRACT (Continue on reverse if necessary and identify by block number) This work is the first AFRPL effort at taking certain plume diagnostics experiments out of the laboratory and into the field. Four major objectives were sought after: 1) gauging the use of laser transmissometer measurements as a plume visibility figure of merit; 2) measuring the ensemble particle size distribution function (PSDF) through application of Mie theory in deconvolving polarization/scattering laser signals from lightly-loaded (and therefore single-scattering) solid rocket motor plumes; 3) retrieving temperature and partial pressure profiles through multispectral infrared emission and absorption measurements; and 4) quantifying exit plan multispectral ultraviolet emission. Success has been limited. Laser transmittance as a visibility figure of merit embeds many assumptions and has not been positively correlated with total plume detectability. Nonetheless, different propellants are seen to have characteristic transmittance values and a propellant visibility ranking using this criterion has been undertaken using a limited experimental sample. The volume-to-surface effective mean particle diameters through applicable transmissometer/			
20. DISTRIBUTION/AVAILABILITY OF ABSTRACT UNCLASSIFIED/UNLIMITED <input checked="" type="checkbox"/> SAME AS RPT. <input type="checkbox"/> DTIC USERS <input type="checkbox"/>		21. ABSTRACT SECURITY CLASSIFICATION UNCLASSIFIED	
22a. NAME OF RESPONSIBLE INDIVIDUAL Lt James A. Misener		22b. TELEPHONE NUMBER (Include Area Code) (805)277-5584	22c. OFFICE SYMBOL AFRPL/DYSO

- 18. particle collection probes
 - laser transmissometer
 - plume visibility

19. extinction measurements were made rather than PSDFs due to difficulties in size distribution inversion schemes and low experimental signal-to-noise ratios. Captured particulates show they may be hollow. A follow-on supersonic shock swallowing particle collection probe has been designed to reduce the bias errors characteristic of particle capturing efforts. Inversion and instrumentation difficulties arose in applying the multispectral emission/absorption technique. UV spectra reveal a continuum even with propellants having no particle loading, giving credence to chemiluminescence as a major mechanism. Line structure reveals the presence of trace impurities, possibly coming from the motor case. These results give the foundation toward future AFRPL work in this area. It will be specifically aimed at quantifying input parameters for and verifying rocket plume signature predictions.

Accession For	
NTIS GRA&I	<input checked="" type="checkbox"/>
DTIC TAB	<input type="checkbox"/>
Unannounced	<input type="checkbox"/>
Justification	<input type="checkbox"/>



A-1

TABLE OF CONTENTS

<u>Section</u>		<u>Page</u>
1.0	INTRODUCTION	1
2.0	APPARATUS	2
2.1	BATES Test Stand and Motor	2
2.2	Propellants	3
2.3	Particle Sizing Instrumentation	5
2.3.1	Laser Transmission/Scattering Instruments	6
	Description	6
	Signal Conditioning	11
	Calibration	11
	A. Laser and Laser Power Meter	11
	B. Scattering Detectors	17
2.3.2	Particle Collection Probes	23
	Subsonic Particle Collection Probe Description	28
	Supersonic Particle Collection Probe Description	29
2.4	Plume Signature Instrumentation	32
2.4.1	Infrared Emission Absorption (IR-E/A)	32
	Description	33
	Signal Conditioning	35
	Calibration	36
2.4.2	Ultraviolet (UV) Instrumentation	40
	Description	40
	Signal Conditioning	41
	Calibration	41
3.0	DATA REDUCTION AND RESULTS	43
3.1	Plume Visibility Figure of Merit	43
3.1.1	Introduction and Transmissometer Data Reduction Methods	43
3.1.2	Transmissometer Results and Interpretation	45
3.2	Plume Particle Sizes	47
3.2.1	Transmissometer Data Reduction Methods	47

TABLE OF CONTENTS (Concluded)

<u>Section</u>		<u>Page</u>
3.2.2	Transmissometer Results and Interpretation	54
3.2.3	Particle Collection Probe Technique Data Reduction Methods	57
3.2.4	Particle Collection Probe Technique Results and Interpretation	57
3.3	Plume Temperatures and Partial Pressures	59
3.3.1	IR-E/A Technique Data Reduction Methods	59
3.3.2	IR-E/A Technique Results and Interpretation	63
3.4	Plume UV Signatures	65
3.4.1	UV Data Reduction Methods	65
3.4.2	UV Results and Interpretation	66
4.0	CONCLUSIONS	71
4.1	Summary and Discussion	71
4.2	Future Work	73
REFERENCES		74
APPENDIX A	A BRIEF REVIEW OF THE THEORETICAL BASIS OF THE AFRPL ROCKET EXHAUST PARTICLE SIZING EFFORT: ASSUMPTIONS AND MODELING	79
APPENDIX B	A BRIEF REVIEW OF THE THEORETICAL BASIS OF THE AFRPL INFRARED EMISSION/ABSORPTION EXPERIMENT TO RETRIEVE PLUME SPECIES TEMPERATURES AND PARTIAL PRESSURES: ASSUMPTIONS AND MODELING	89
APPENDIX C	A BRIEF REVIEW OF THE ADAPTIVE NOISE CANCELING SIGNAL PROCESSING TECHNIQUE AS APPLIED AT AFRPL	95
APPENDIX D	DESCRIPTION OF THE AFRPL PLUME RADIOMETRIC MEASUREMENTS PLANNED FOR 1984	103

LIST OF FIGURES

<u>Figure</u>		<u>Page</u>
1	Schematic of 15-lb BATES Motor	3
2	Schematic Diagram of AFRPL Laser Transmission/Scattering Measurement System	7
3	AFRPL Laser Transmission/Scattering Measurement System During Motor Firing	8
4	Laser Scattering Detector Schematic	9
5	Laser Scattering Detector Cross Section	10
6	Idealized Scattered Light Data Polarizer Activation Sequence	11
7	Laser Output Voltage vs Time	12
8	Probability Density vs Laser Output Voltage, Interval 1	13
9	Probability Density vs Laser Output Voltage, Interval 2	14
10	Laser Output Voltage Power Spectrum, Interval 1	15
11	Laser Output Voltage Power Spectrum, Interval 2	16
12	Laser Power Meter Output Voltage vs Time	17
13	Probability Density vs Laser Power Meter Output Voltage, Interval 1	18
14	Probability Density vs Laser Power Meter Output Voltage	19
15	Laser Power Meter Output Voltage Power Spectrum, Interval 1	20
16	Laser Power Meter Output Voltage Power Spectrum, Interval 2	21
17	Blackbody Spectral Radiant Exithance Distribution Curves for Temperatures Between 1000 and 2000K	22
18	Scattering Detector 5 Output Voltage vs Time	23
19	Probability Density vs Scattering Detector 5 Output Voltage vs Time, Interval 1	24
20	Probability Density vs Scattering Detector 5 Output Voltage vs Time, Interval 2	25
21	Scattering Detector 5 Output Voltage Power Spectrum, Interval 1	26
22	Scattering Detector 5 Output Voltage Power Spectrum, Interval 2	27
23	Subsonic Particle Collection Probe	28
24	Platinum Wire Collection Assembly	29
25	Supersonic Shock-Swallowing Quench Probe	31

LIST OF FIGURES (Continued)

<u>Figure</u>		<u>Page</u>
26	Top View of IR-E/A System	33
27	Aft-End View of IR-E/A System	34
28	Block Diagram of Signal Conditioning System	35
29	Theoretical Distribution of Radiant Energy with Wavelength Exit Slit	37
30	Top View of UV Measurement System	40
31	1200 Grooves/mm Diffracting Grating Efficiency vs Wavelength	41
32	Size Distribution Retrieval Compared with Inputted Size Distribution from Young	50
33	Scattering Detector vs Time Signal with a 15-lb BATES Motor Chamber Pressure Trace	51
34	SEM Photomicrograph of Two Captured 10 μ m Al ₂ O ₃ Spheres	58
35	Temperature Inversion Results from Young's BATES Plume Model	61
36	Concentration Inversion Results from Young's BATES Plume Model	62
37	In-Band (2.4-2.7 μ m) Radiation Axial Profiles for 15-lb BATES Motor Plumes with Identical Propellants	63
38	Typical 15-lb BATES Motor Water Band IR Emission Trace	65
39	Voltage Response vs Wavelength for 16 Mid-Firing Half-Scans for KKN Propellant	67
40	Voltage Response vs Wavelength for 16 Mid-Firing Half-Scans for CWB Propellant	68
41	Voltage Response vs Wavelength for 16 Mid-Firing Half-Scans for DWP Propellant	69
42	Single Half-Scan Comparisons of Representative Voltage Responses vs Wavelengths for Three Reduced Smoke Propellants	70

LIST OF FIGURES (Concluded)

<u>Figure</u>		<u>Page</u>
A-1	Al ₂ O ₃ Particles Captured at AEDC from a 0.25-lb Solid Rocket Motor	81
B-1	Gas-Only Flow Optical Geometry	92
B-2	Gas-Particle Flow Optical Geometry	94
C-1	An Adaptive Noise Cancelling System	95
C-2	SDI Signal	99
C-3	A Posteriori Reference Signal	100
C-4	Adaptive Noise Cancelling System Output	101
D-1	Radiometer Normalized Spectral Response	104
D-2	In-Band Radiant Intensity vs Axial Position Along 15-lb BATES Motor Plume Centerline	105

LIST OF TABLES

<u>Table</u>		<u>Page</u>
1	15-1b BATES Motor Configuration	4
2	Weight Percentage Composition of Representative AFRPL Reduced Smoke Propellants	4
3	Plume Species Compositions of HTMFP, LTMFP and RSP Propellants at Sea Level	5
4	Some Laser Transmission/Scattering Electro-Optical Parameters	9
5	Transmissivities for 29 15-1b BATES Motor Firings	46
6	Particulate Size from Transmissometer Experiment	55
7	D ₃₂ and D ₄₃ Comparison	56

1.0 INTRODUCTION

The Air Force Rocket Propulsion Laboratory (AFRPL) regularly conducts subscale thrust stand tests using the Ballistic Test and Evaluation System (BATES). The tests serve to characterize propellant performance in standard test motors, and the performance parameters usually measured are chamber pressure and thrust. Although these ballistic measurements are essential inputs in assessing propellant formulations, they yield little insight to combustion or plume radiation phenomena.

Increased efforts in the development of missile early warning, identification, and damage assessment systems require more accurately defined plume radiation and particle property knowledge. Plume signature measurements can serve to help verify Joint Army, Navy, NASA and Air Force (JANNAF) plume signature prediction code output since particle properties are sensitive and not well-characterized input parameters to these codes. Better quantification will reduce the uncertainty of code predictions. Spectral signatures and visibility figures of merit can also be used to assess propellant formulation observability trade-offs. The need for plume measurements is especially clear in light of targets of opportunity offered by the ongoing AFRPL BATES experiments.

BATES solid rocket motor exhaust plume measurements were sought after in an in-house project entitled Solid Rocket Motor Test Analysis. This work was directed toward three objectives: (1) to measure plume infrared (IR) radiative emission and absorption characteristics; (2) to measure plume ultraviolet (UV) radiation signatures; and (3) to measure plume particle sizes. An ancillary goal was to investigate use of a measurement in serving as an observability figure of merit, in particular, laser transmissivity. The original intent of the measurements was to reduce particle sizing laser transmission and scattering measurements to particle size distribution functions (PSDF's) and to reduce IR emission/absorption (IR-E/A) measurements to species temperature and concentration profiles. Supplemental in-vitro particle size measurements were also sought after via particulate sampling probes. All these measurements were to be compiled in a data file available for predictive code and propellant formulation analyses as needed. Actual

results fall somewhat short of these objectives and are detailed within the text of this report.

The rocket plume measurement instrumentation was chosen to specifically address specific measurement goals. The instrumentation includes a multi-wavelength, single line-of-sight IR-E/A system, a UV emission spectrometer, an exhaust flowfield particle collection probe and a laser transmissometer/scattering system capable of recording beam attenuation and Mie scattered light in both polarized states and in its unpolarized form. An additional instrument--a narrow field of view radiometer--was applied in this project but only in a few firings late in the experimental sequence. This application is discussed in Appendix D.

The specific data reduction and retrieval methods associated with deconvolving plume species temperature and concentrations from E/A data and plume particle sizes from laser transmission and scattering data are described in Sections 3.1 and 3.3, respectively, and in Appendices A and B. The primary focus of this report is the AFRPL rocket exhaust measurement methodology and ensuing results.

2.0 APPARATUS

Descriptions of the facilities and instruments used, calibration steps applied, and the procedures for signal conditioning data output follows. The reasons for applying this instrumentation and the associated signal conditioning and calibration techniques are discussed in this section.

2.1 BATES Test Stand and Motor

The plume measurements were conducted at an ambient test facility, Pad 5a of Experimental Area 1-32. The Allegany Instrument Company thrust stand at Pad 5a is designed to measure from 0 to 500 and from 0 to 10,000 lbs with +0.125% accuracy. Data was input digitally using the Nova DATUM Data Acquisition and Control System (DACS) at a 1000 samples/second rate for ballistic motor parameters and at a 250 samples/second rate for the optical plume measurements.

The 15-lb BATES motor used with the plume measurements is particularly well-suited to tactical solid rocket motors. Although the 15-lb BATES motor uses different insulation and ignitor, its operating conditions and 7-in. grain diameter are similar to those found in a field application. Figure 1 is a schematic of a 15-lb BATES motor whose motor characteristics are summarized in Table 1.

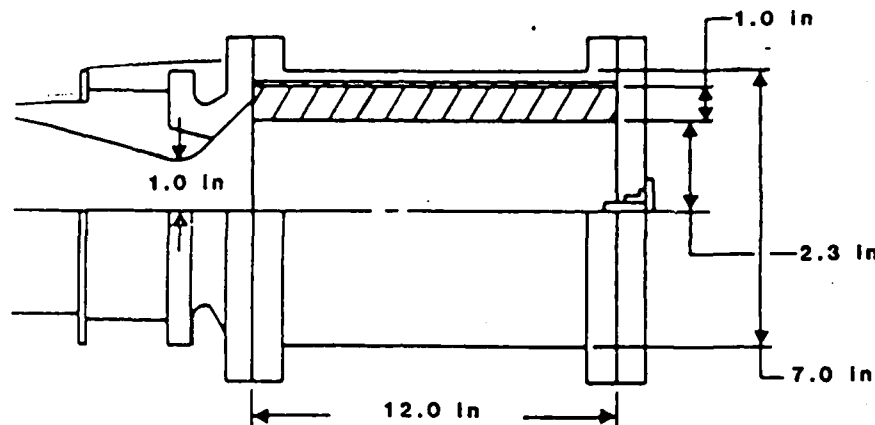


Figure 1. Schematic of 15-lb BATES Motor

2.2 Propellants

The propellants used were reduced smoke, low burn rate formulations, and most were targets of opportunity afforded by ballistic evaluations undertaken in air-launched propellant studies (Refs. 1 and 2). Aluminum was added to the propellant more to stabilize combustion than as a fuel. Table 2 lists ingredient compositions of representative reduced smoke propellants used in the firings reported here.

Representative exhaust gas mole fractions have been calculated for a 16% Al fuel mass fraction-loaded propellant plume (designated Smoky) (Ref. 4) and for three general reduced smoke plumes classes, High Temperature Methal Fuel Solid Rocket Plumes (HTMFP: CO, HCl, Al₂O₃), Low Temperature Methal Fuel Solid Rocket Plumes (LTMFP: H₂O, CO, HCl, Al₂O₃), and Reduced Smoke Low Visibility Solid Rocket Plume (RSP: H₂O, CO₂, CO, HCl, Al₂O₃) (Ref. 3). These are listed in Table 3. Note that most plumes measured in this project, including those propellants listed in Table 2, fall in the RSP class.

Table 1. 15-Pound RATES Motor Configuration

Nominal Propellant Weight, kg	7
Maximum Pressure, MPa	14
Pressure Range, MPa	1 to 14
Motor Weight, kg	60
Nozzle Divergence Angle, deg	15
Nozzle Convergence Angle, deg	45
Grain Configuration, cm	
Length	30
Outer Diameter	17.15
Inner Diameter	11.68
Web, cm	2.54
Web Action Time, s	1 to 5
Burning Surface, cm ²	1320
Mass Flow Rate, kgs ⁻¹	1 to 7
Burning Rate, mms ⁻¹	3 to 25
Pressure Neutrality	1.08
Port-to-Throat Ratio	3 to 32
Nozzle Throat Diameters, cm	1 to 6
Ignitor BKNO ₃ pellets	

**Table 2. Weight Percentage Composition of Representative
AFRPL Reduced Smoke Propellants**

<u>Ingredient</u>	<u>RSS</u>	<u>JAC</u>	<u>KKN</u>	<u>GWB</u>	<u>DWP</u>
Ammonium Perchlorate (AP)	86.0	86.0	86.5	76.0	75.0
Hydrocarbon Binder	8.64	10.8	9.7	9.7	9.7
Diocetylazelate (DOA)	2.15	2.19	2.0	2.0	2.0
Al ₂ O ₃	0.50	0.50	---	---	---
R _b Suppressant	---	---	1.5	12.0	5.0
Dimosyle Disscynate	2.19	---	---	---	---
Other Additives	0.53	0.53	0.3	0.3	8.3

The RSP formulation with its low Al₂O₃ loading is amenable to a laser transmissometer/scattering application because multiple scattering, focal

**Table 3. Plume Species Compositions
of HTMFP, LTMFP and RSP Propellants at Sea Level**

	<u>Smoky</u>	<u>HTMFP</u>	<u>LTMFP</u>	<u>RSP</u>
Temperature (K)	1860	1800	1000	1000
Pressure (atm)	1.22	1.0	1.0	1.0
Plume Model Fraction				
<u>Gases</u>				
H ₂ O	0.020	0.02	0.30	0.40
CO ₂	0.0037	---	---	0.12
CO	0.30	0.30	0.02	0.12
HCl	0.13	0.13	0.13	0.18
H ₂	0.41	0.40	0.40	0.40
N ₂	0.068	0.10	0.05	0.03
<u>Particles</u>				
Al ₂ O ₃	0.07	0.50	0.50	0.05

(Note that H₂O, CO₂, CO and HCl are the major UV/IR radiating RSP gas species. H₂ and N₂ are UV/IR nonradiating).

volume coincidence and particle cross-sensitivity effects are mitigated by the relatively low optical thickness of these propellant plumes. In contrast, highly aluminized plumes from high performance propellants (HTMFP and LTMFP) attenuate the laser signal to the point where background radiation, multiple scattering, coincidence and cross-sensitivity error sources dominate. These issues are addressed in Section 2.3 and in Appendix A.

2.3 Particle Sizing Instrumentation

Both nonintrusive and intrusive particle sizing instruments were used in this series of BATES motor plume measurements. The nonintrusive instruments were optical and consisted of a laser transmission/scattering experiment. Intrusive techniques included probe sampling of the plume exhaust flow.

2.3.1 Laser Transmission/Scattering Instruments

Description - The AFRPL laser transmission/scattering configuration was modeled after an Arnold Engineering Development Center (AEDC) particle size retrieval experiment with a short-duration (130 ms) arc-heated flowfield (Ref. 5). The intent was to translate the AEDC particle size measurement method to AFRPL measurements. This technique had never before been applied to rocket exhaust flowfields.

The laser transmission/scattering measurement system orientation is depicted in Figures 2 and 3. The system was designed to accomplish plume measurements in the relatively short-lived and hostile BATES motor test environment. The anticipated severity of vibration and temperature dictated installing a massive 250-kg support structure to enclose the measurement instruments and to maintain alignment between the laser and detectors. The structure was fabricated from 30-cm channel iron and was mounted in a concrete foundation. A laser and detectors were attached to this rigid structure (Fig. 3). A 3.5-cm thick rigid aluminum-backed foam insulated the entire structure and provided the enclosed instrumentation with some measure of protection from both the hostile exhaust plume environment and shrapnel from occasional nozzle failures. The structure was set 2 meters axially from the exit plane of a mounted 15-lb BATES motor casing. The entire system was kept indoors to maintain a controlled ambient temperature.

Figure 2 is a schematic of the instrumentation system which starts from a 4 Watt Argon-ion laser located across the plume from a laser power meter; this is the laser transmissometer portion of the experiment. There are six detectors arranged in a plane perpendicular to the plume axis and a seventh broadband detector for scattering measurements. Electro-optical parameters associated with this system (Table 4) are detailed in the ensuing discussion.

The Control Laser Corporation Model 552A 4W Argon-ion laser operates multi-line, but delivered 1.5 W average power at 514.5 nm for these measurements. The beam was interrupted for approximately 0.2 s midway through

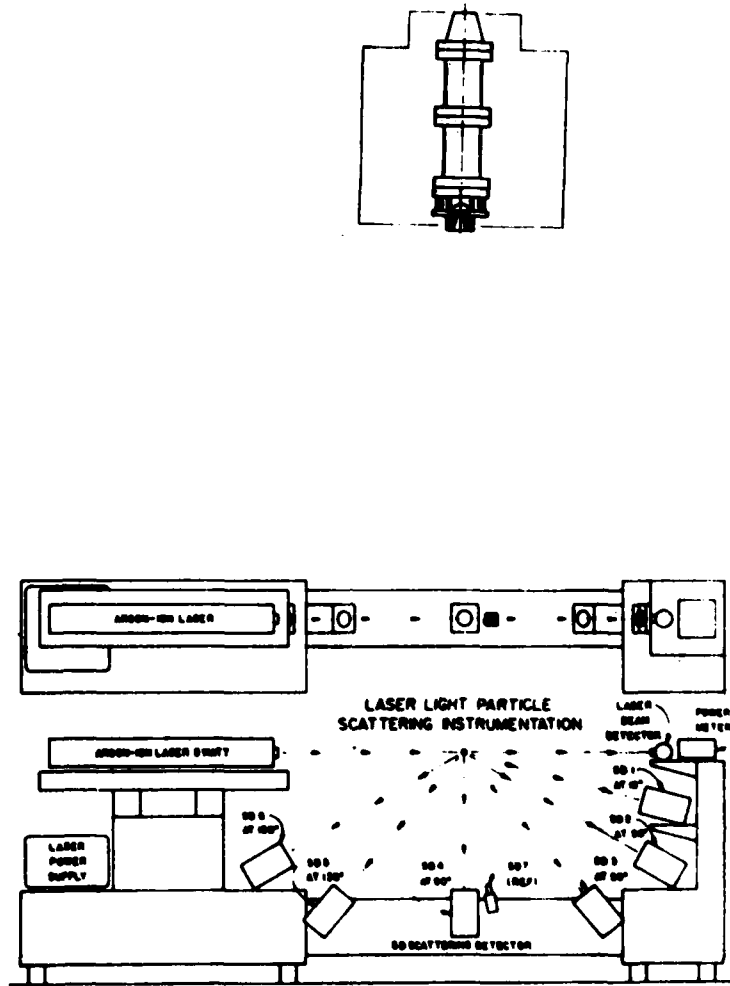


Figure 2. Schematic Diagram of AFRPL Laser Transmission/
Scattering Measurement System

each motor burn with a solenoid-operated shutter to enable subsequent correction of power meter and scattering detector output. The output at the laser source was independently monitored to spot and correct laser power fluctuations and long term drift.

During operation the laser light first traversed a 45° polarizer, thus simulating unpolarized light (comprised of equal parallel- and perpendicular-polarized components). The United Detector Technology (UDT) Model 21A optical power meter used to detect the transmitted laser signal had a broadband (380-

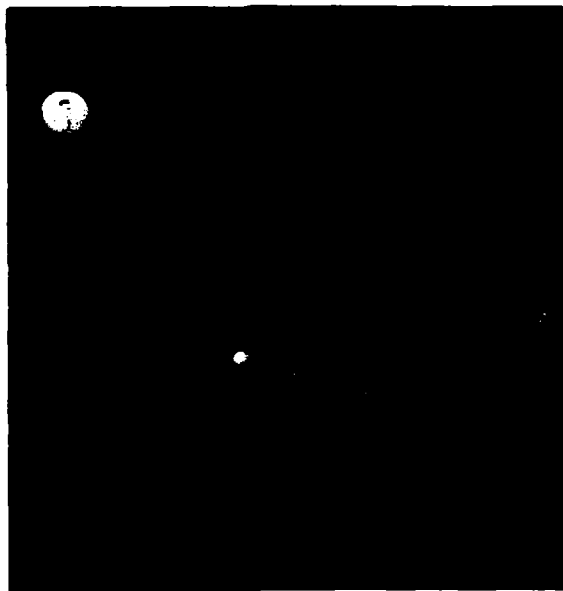


Figure 3. AFRPL Laser Transmission/Scattering Measurement System During Motor Firing

1100 nm) spectral range silicon PIN photovoltaic photodiode detector. A 10-nm full width half maximum (FWHM) bandwidth filter centered at the 514.5-nm laser wavelength was placed between the power meter detector and a UDT Model 2500 integrating sphere exit port and enabled full use of the power meter's 0.1 μ W - 10W sensitivity range.

The six scattering detector angles are indicated on Figure 2 as 15, 30, 50, 90, 120, and 150 degrees from the forward scattering direction. The scattering detection assemblies at each of these angles were identical, each with 10-cm diameter f/2.0 lenses. Figure 4 shows the configuration of the laser scattering detector and Figure 5 is a photograph of the laser scattering detector cross section.

These scattering detectors were designed to operate in the same plane orthogonal to the plume axis. All six were to be equidistant to the centerline, defining, along with the laser beam shape profile, a scattering volume on which ensemble Mie particle deconvolution techniques could be applied. Application of the Mie theory and the assumptions used are described in Appendix A. AFRPL data application retrieval methods are discussed in Section 3.1.

**Table 4. Some Laser Transmission/Scattering
Electro-Optical Parameters**

LASER

Beam Power (TEM_{00}) = 4W nominal, 1.5 W @ 514.5 nm

Beam Width = 2.0 mm

Beam Shape = Gaussian

Wavelength = 514.5 nm

POWER METER DETECTOR (Si Photodiode)

Optical Bandwidth = 10 nm centered @ 514.5 nm

Electrical Bandwidth = DC to 500 kHz (but with total power meter
system at DC to 200 Hz)

Detector Active Area = 1.0 cm^2

Noise Equivalent Power (NEP) = $5.9 \times 10^{-14} \text{ W}$ (1000 Hz, 1 Hz, 880 nm)

SCATTERING DETECTORS (Si Photodiode)

Optical Bandwidth = 1 nm centered @ 514.5 nm

Electrical Bandwidth = DC to 0.1 MHz

Detector Active Area = 1.0 cm^2

NEP = $1 \times 10^{-12} \text{ W}$ (1000 Hz, 1 Hz, 850 nm)

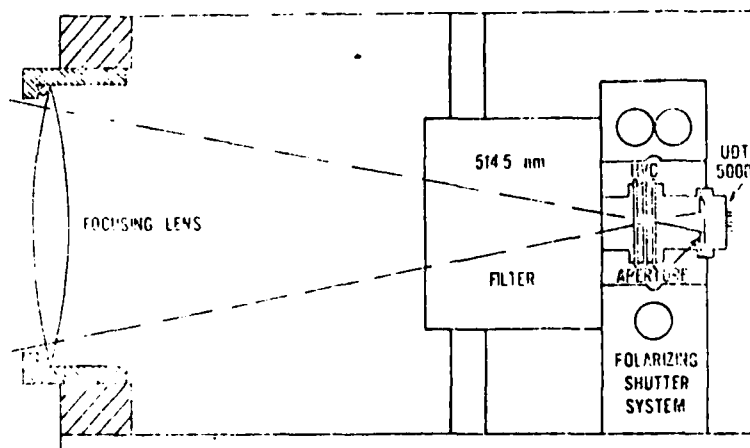


Figure 4. Laser Scattering Detector Schematic

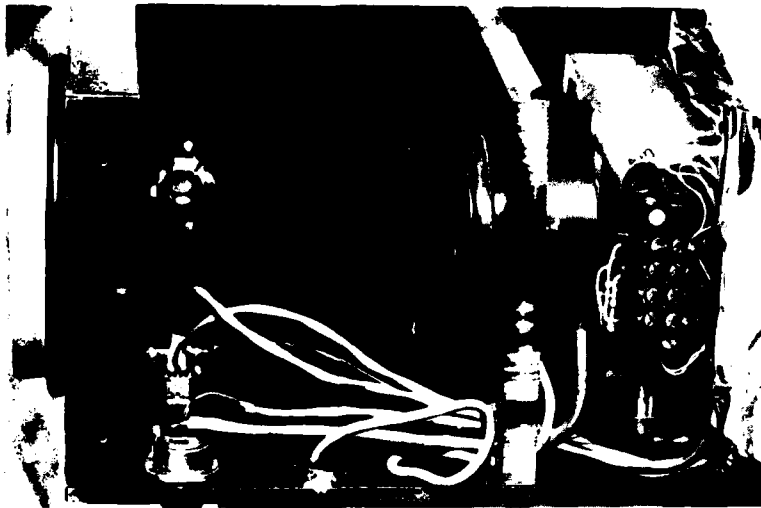


Figure 5. Laser Scattering Detector Cross Section

Each of the six scattering detectors had four detection modes: vertically polarized, horizontally polarized, nonpolarized and dark. For each detector, rapid sequencing of 18 polarizing filters was initially used to give 100-ms time resolution for each of the detection modes, but because of stresses induced by this dynamic mechanical environment, the improvements described by Reference 6 were implemented. With these improvements time resolution still remained at 100 ms, but 12 aluminum-reinforced DC solenoid-actuated detectors sequencing every 400 ms now comprised the polarization system. Figure 6 illustrates how a scattering detector channel signal with such a sequence was designed to appear. There was an approximately 10-ms settling time in the filter activation sequence. This sequence was similar to the preimprovement filter sequence, with differences accounted for by data preprocessing.

The six scattering detectors were UDT Model 500D silicon photovoltaic detectors responding from 300 to 1100 nm with 10^{-3} to 10^{-12} W selectable nominal sensitivity at 850 nm. A narrow 0.1-nm FWHM interference filter separated the scattered laser light from other plume emission wavelengths. The seventh detector was also a UDT Model 500 photodiode, but it had a relatively broadband filter (10-nm FWHM centered at 514.5 nm). It was mounted alongside the 90° scattering angle detector and placed in an unfocused detector assembly directed upstream from the laser beam but still at the plume

centerline. It was to serve as a plume radiation correction signal for the six narrowband scattering detector outputs.

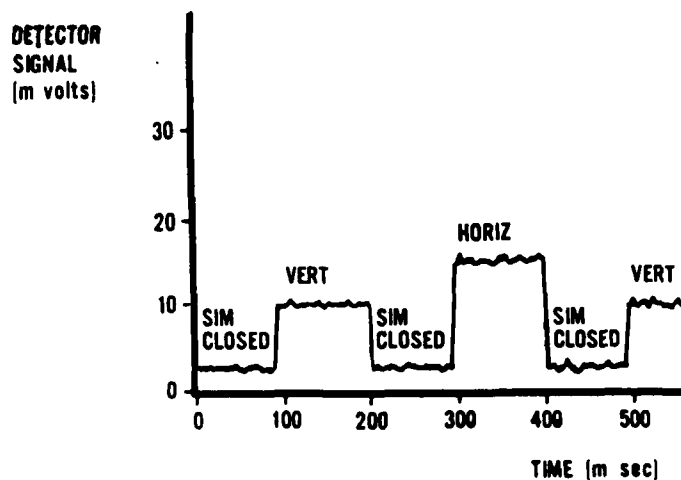


Figure 6. Idealized Scattered Light Data Polarizer Activation Sequence

Signal Conditioning - Signals from the laser power meter and seven scattering detectors were amplified at each instrument with a preamplifier then carried on 300 ft of coaxial shielded cable to the data acquisition system. Signals of 0-10 mv amplitude were digitized, then recorded at 250 samples/s on a 100 Hz-filtered NOVA DATUM digital data acquisition system magnetic storage tape.

Calibration

A. Laser and Laser Power Meter - The laser power meter operated in an uncalibrated absolute responsivity mode since transmissometer data reduction was accomplished mainly by measuring laser transmittance values during rocket motor firings. Since the zero transmittance level was accomplished at midfiring by a laser beam breaker, background levels were accounted for and did not need to be calibrated out. However, two important calibration considerations still remained: verification of laser power stability and background and random noise determination.

A data channel from the laser source was directly monitored to give continuous laser output voltage vs time. This data was divided into two equal time intervals and histograms depicting the laser output voltages for each of these intervals were calculated, then overlaid with theoretical normal distribution curves determined from data means and standard distributions. If the laser noise was indeed Gaussian random in form (and, therefore, subtractable as white noise), the histogram bins would follow the normal distribution model; moreover, there would be little variation between the two independent time intervals. An application of this analysis to a BATES firing is depicted by Figures 7-9.

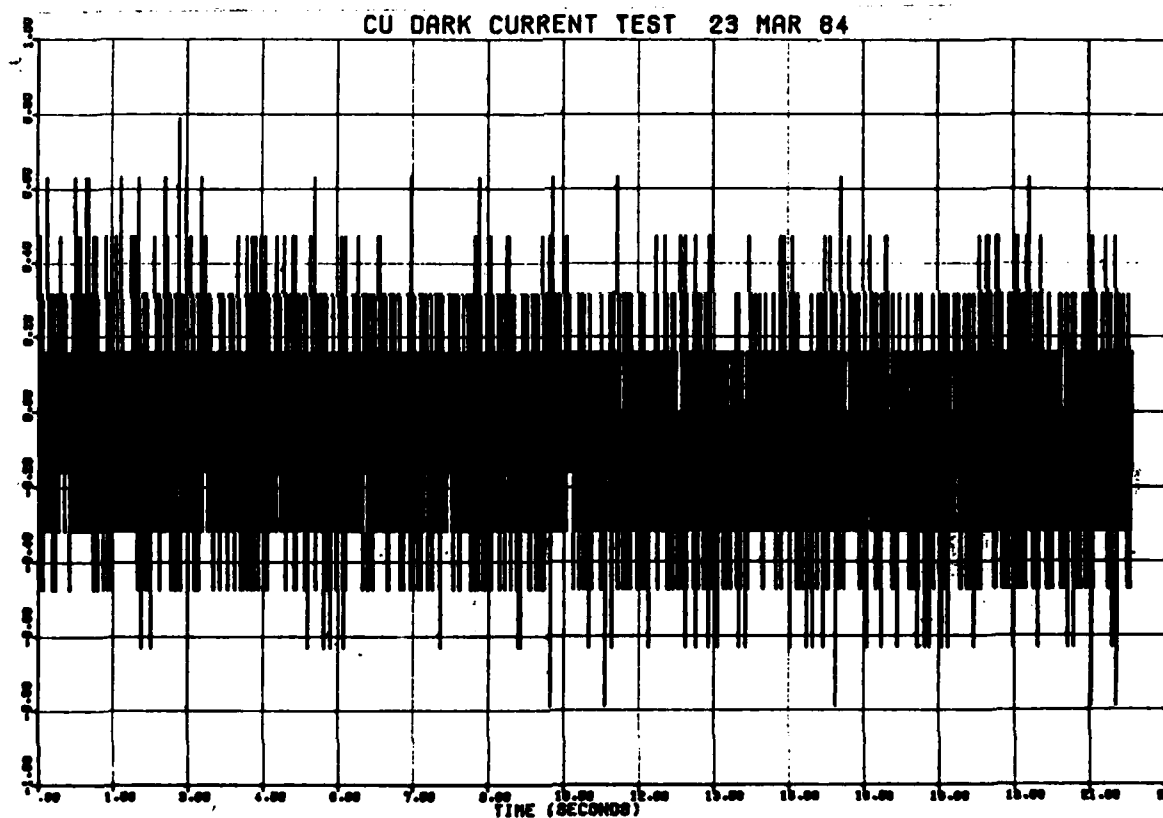


Figure 7. Laser Output Voltage vs Time

Note that the quantization observed in Figure 7 is a consequence of the low signal rate from the laser output voltage channel. The data steps recorded in the figure are highly resolved voltage counts from the data

acquisition system. This quantization, when coupled with the small standard bin widths used, explains the gaps in the histograms shown in Figures 8 and 9.

MEAN SQUARE	RMS	VARIANCE	CHI SQ	MEAN VALUE	STD DEV	MINIMUM	MAXIMUM	VALID OBS
480.633	21.923	5.995	843.92	21.786	2.449	12.733	27.823	1358 / 1358

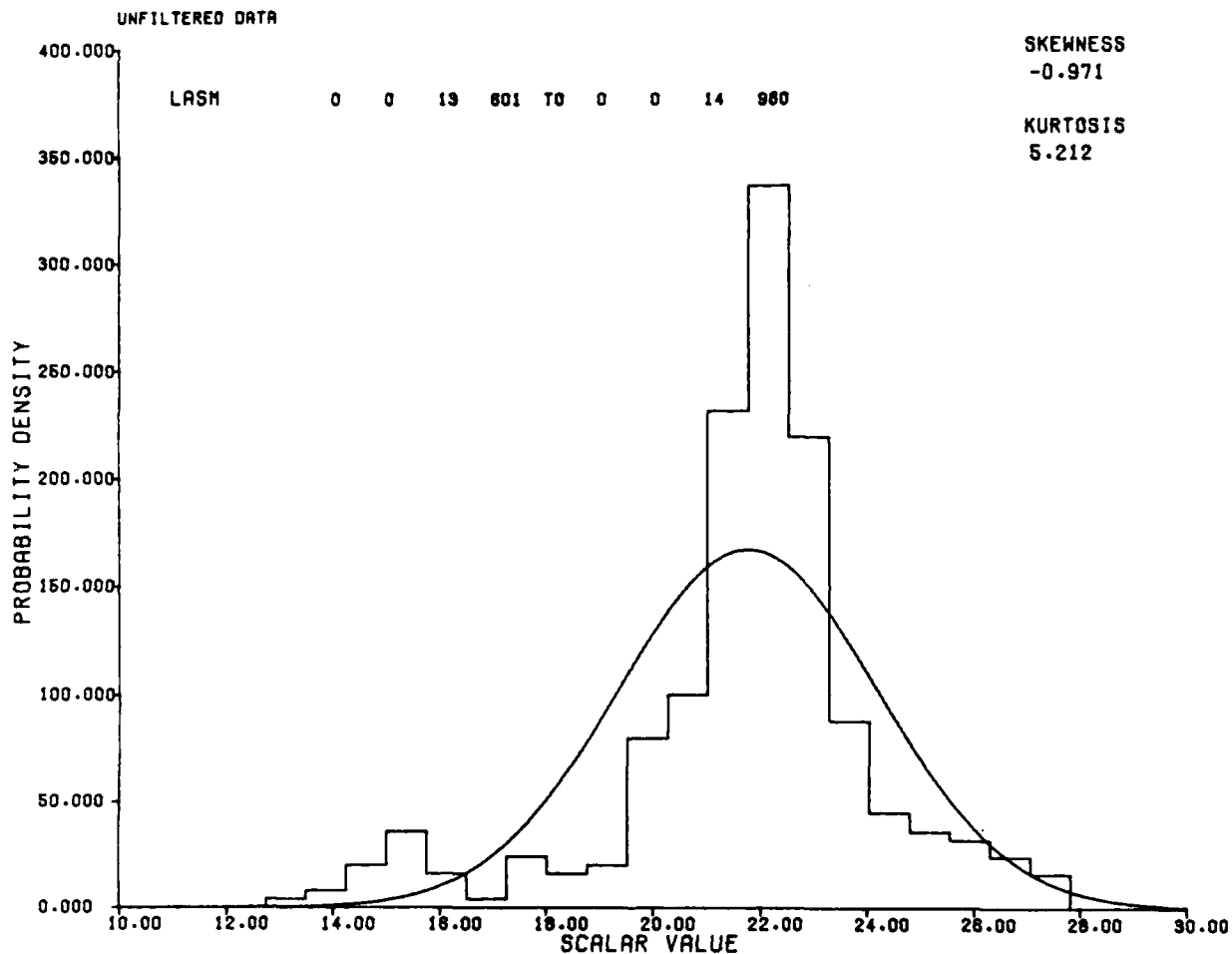


Figure 8. Probability Density vs Laser Output Voltage, Interval 1

To determine the noise contribution from any coherent components, a power spectrum analysis was also undertaken. Figures 10 and 11 show smoothed Hamming window power spectra of the laser voltage output data given in Figure 7. These were taken from the same two time intervals the histograms of Figures 8 and 9 were drawn from.

For the firings reported herein, the laser output voltage noise was

MEAN SQUARE	RMS	VARIANCE	CHI SQ	MEAN VALUE	STD DEV	MINIMUM	MAXIMUM	VALID OBS
539.808	23.234	3.230	93.59	23.164	1.797	19.178	28.766	1358 / 1358

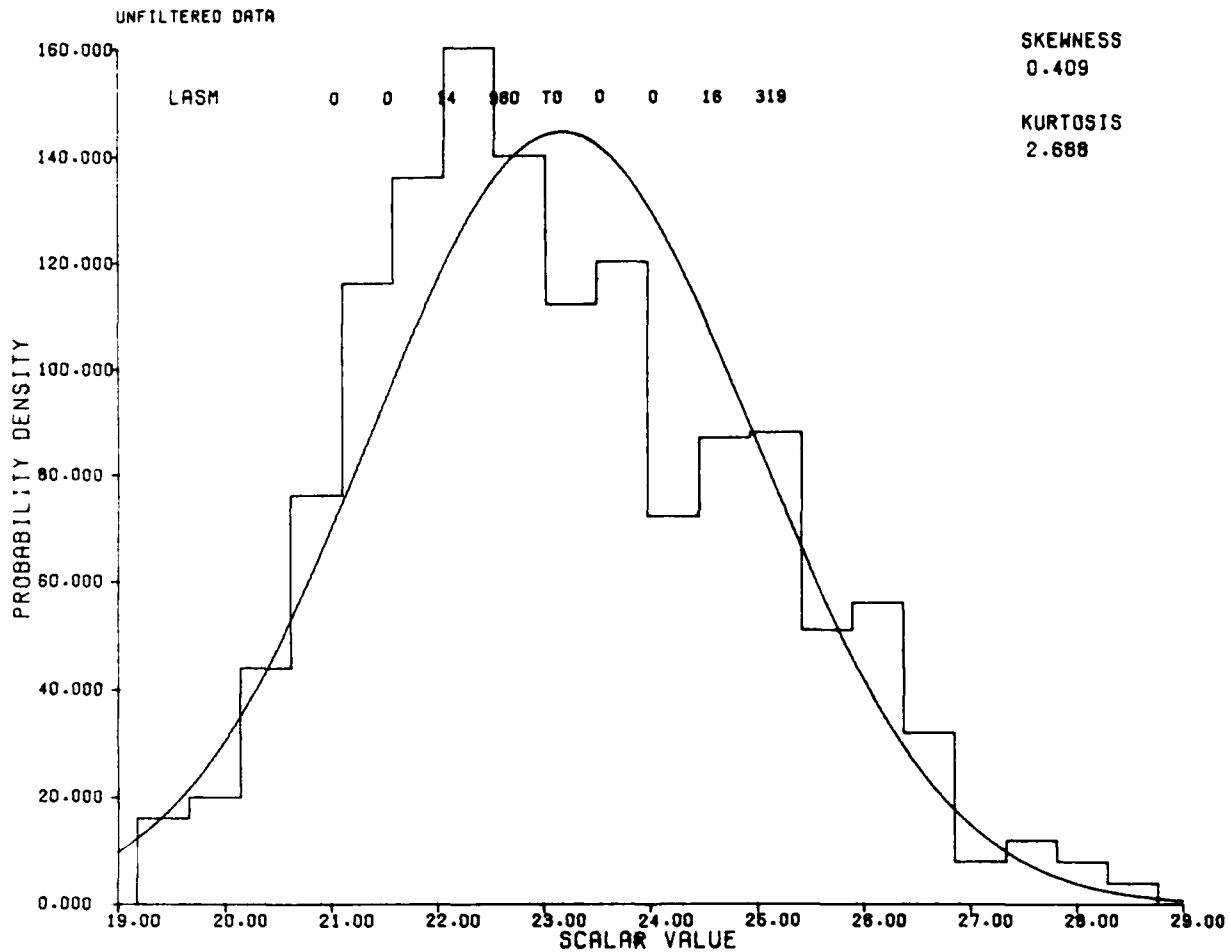


Figure 9. Probability Density vs Laser Output Voltage, Interval 2

found to be incoherent, making the laser transmissometer data suitable for the time-averaged data analysis procedure explained in Section 2.4.

The analysis of background and random noise levels of the laser power meter was accomplished in a similar manner. The laser power meter output voltage channel was periodically monitored for random noise, coherent noise forms and responses to leakages or internal radiation. This monitoring was conducted via a dark current measurement calibration step where the power meter's integrating sphere input aperture was blocked with a light-tight

BATES 262B-005 28/APR/82 TIME INTERVAL -.4 TO 2.8 SECONDS FROM IGNITION
POWER SPECTRUM ST=0 0 14 960 ET=0 0 16 313
LASM SPS 999.00
UNFILTERED DATA
NPT 1353 BANDWIDTH 1.4778 DEG OF FREEDOM 4.00
UNSMOOTHED RMS 23.2883

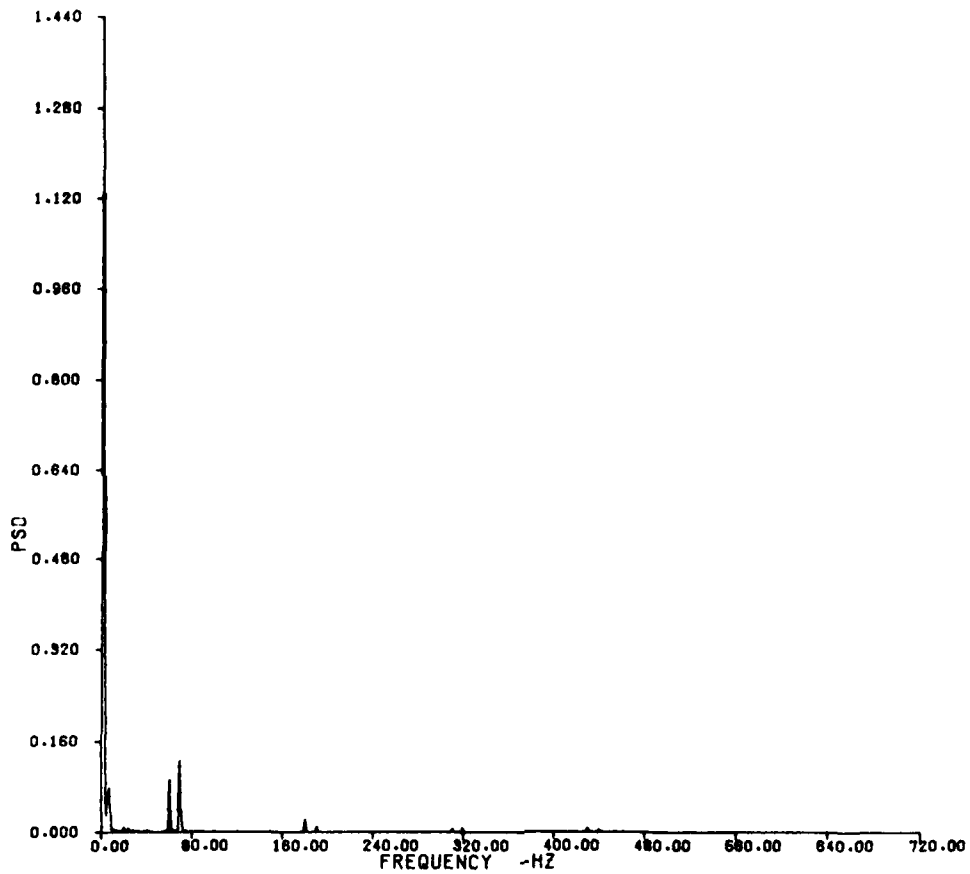


Figure 10. Laser Output Voltage Power Spectrum, Interval 1

cover. As with the previous analysis, the next goal was to identify noise forms present in the calibration data and to eliminate colored noise constituents. Results of a dark current calibration and histogram analysis are shown in Figures 9 and 10. Power spectra are given in Figure 11.

Note the quantization effect evidenced in Figure 12. As with Figure 7

BATES 262B-005 28/APR/82 TIME INTERVAL -.4 TO 2.8 SECONDS FROM IGNITION
 POWER SPECTRUM ST=0 0 14 960 ET=0 0 16 313
 LASM SPS 999.00
 UNFILTERED DATA
 NPT 1353 BANDWIDTH 1.4778 DEG OF FREEDOM 4.00
 SMOOTHED- HAMMING WINDOW 5 POINTS RMS 0.1313

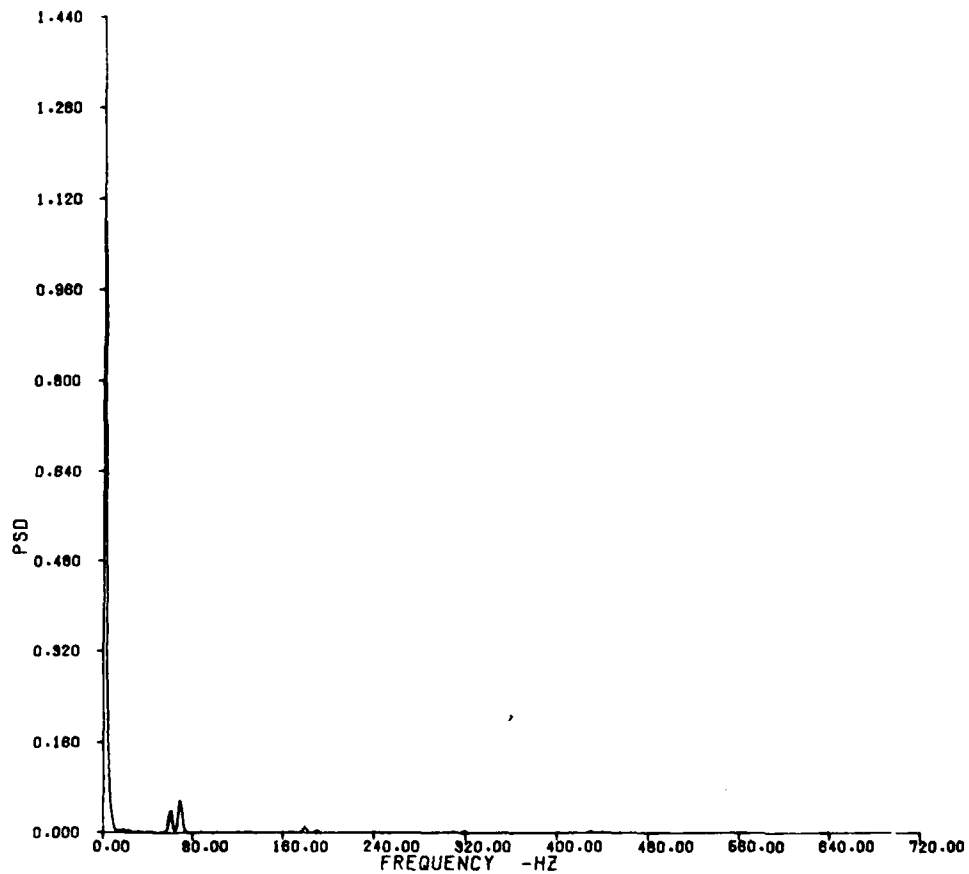


Figure 11. Laser Output Voltage Power Spectrum, Interval 2

this is a result of the disparity between the low signal rate and high data acquisition system resolution. Empty histogram bins of Figures 13 and 14 again result from this quantization.

Note that 60 and 68 Hz noise spikes stand out in the otherwise relatively incoherent noise in the laser power meter dark current calibration

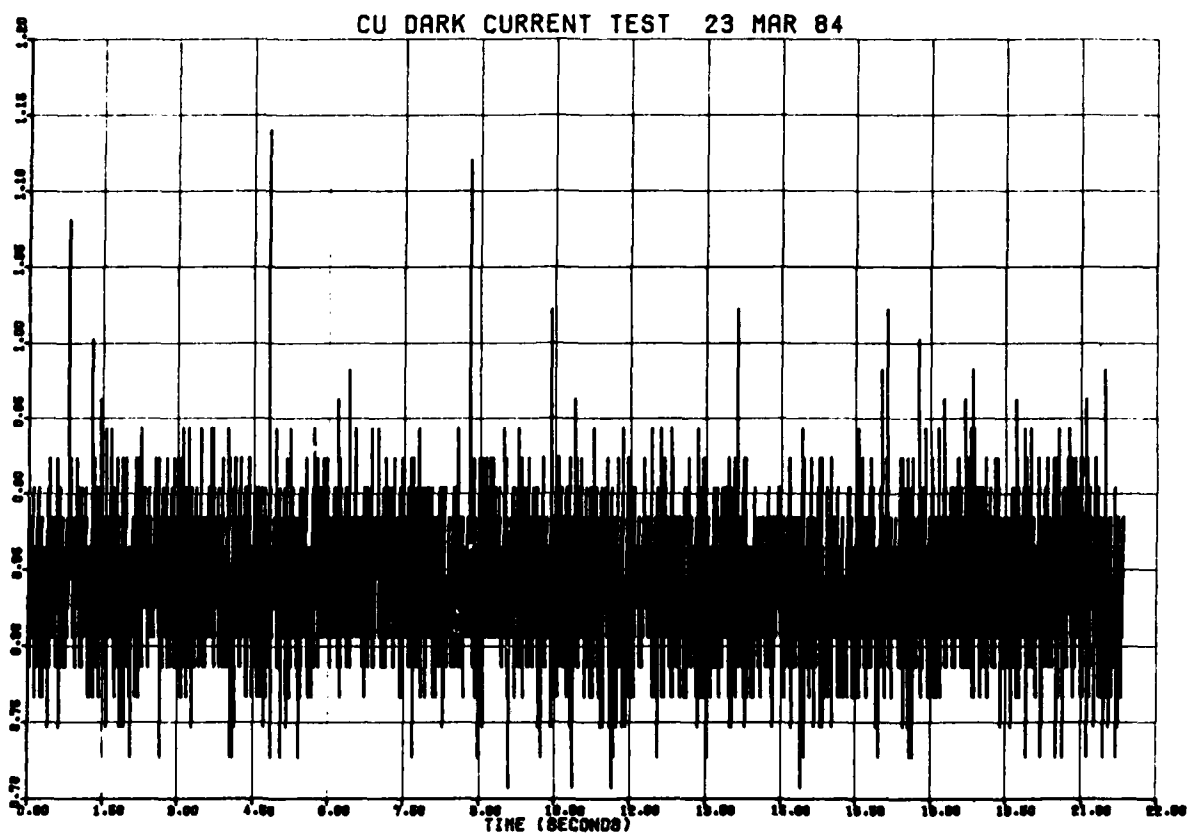


Figure 12. Laser Power Meter Output Voltage vs Time

cut shown in Figure 15. The 60 Hz noise has some background AC current crosstalk and its elimination requires searching characteristic AC sources. The 68 Hz spike, however, is more difficult to control and a narrow band notch filter may be the best fix.

B. Scattering Detectors - Calibrating the absolute responsivity of the scattering detectors presented a difficult problem. The detectors were essentially locked into the scattering geometry depicted in Figure 2, and it was thought that removing them from the laser scattering system for absolute calibration with a blackbody reference source would prohibitively alter the firing-to-firing alignment. However, minor adjustments, especially along the plume radius, were relatively easy to do. To maintain the alignment integrity, a quartz-halogen lamp was placed at the focal volume defined by the scattering detectors. The lamp filled the detectors' FOVs. This absolute

MEAN SQUARE	RMS	VARIANCE	CHI SQ	MEAN VALUE	STD DEV	MINIMUM	MAXIMUM	VALID OBS
0.703	0.838	0.002	989.75	0.837	0.038	0.708	1.022	2818 / 2818

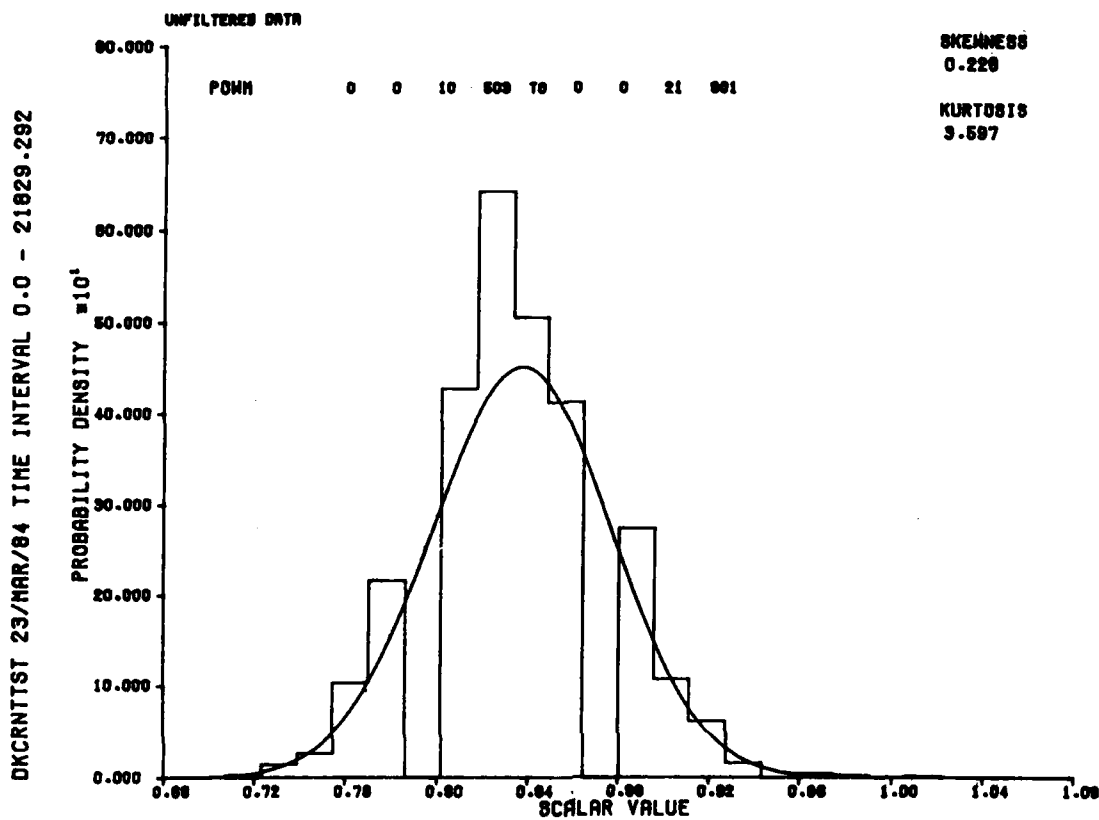


Figure 13. Probability Density vs Laser Power,
Meter Output Voltage

calibration technique assumes spatial radiance uniformity across the lamp, equal scattering detector instantaneous fields of view (IFOVs) and the same relative angle between the lamp and each detector.

To ensure the integrity of the responsivity calibration several supporting calibration parameters were necessarily determined to fully characterize influencing error sources (Ref. 7). These are:

- (1) absolute spectral positioning;
- (2) spectral resolution;
- (3) out-of-band rejection;
- (4) frequency response determination;

MEAN SQUARE	RMS	VARIANCE	CHI SQ	MEAN VALUE	STD DEV	MINIMUM	MAXIMUM	VALID OBS
0.714	0.845	0.002	999.00	0.844	0.039	0.708	1.140	2489 / 2489

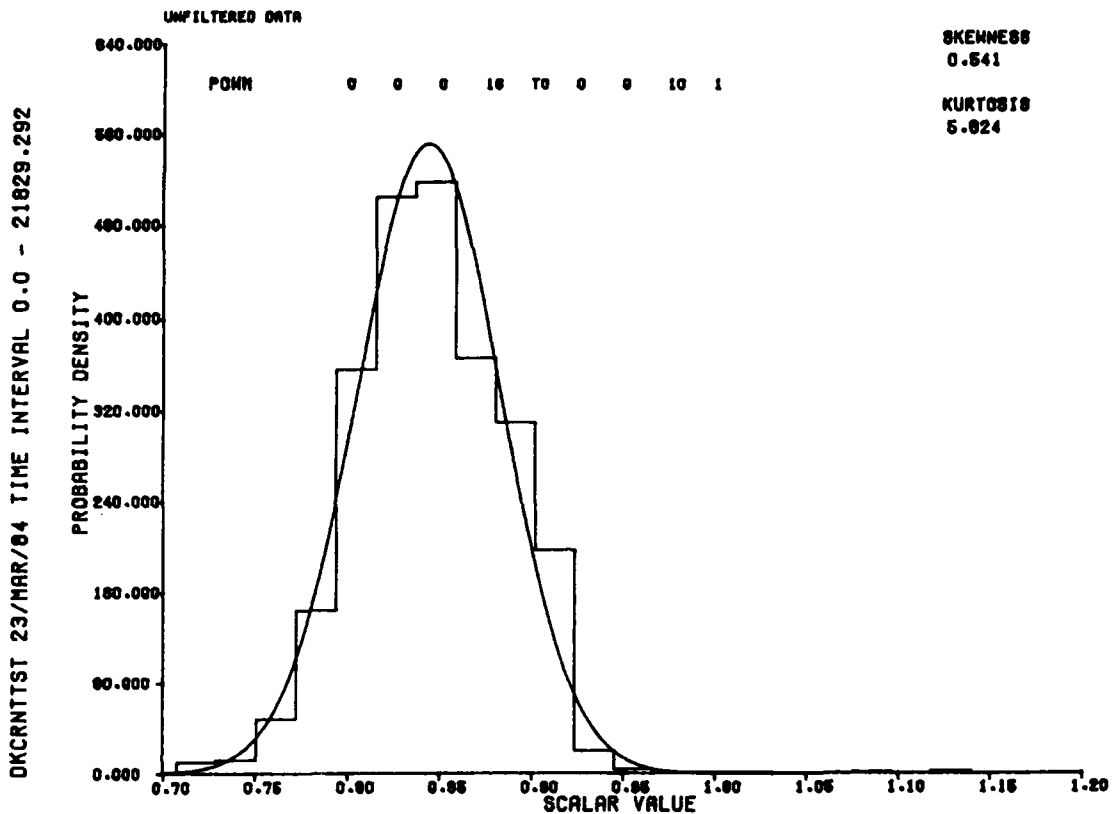


Figure 14. Probability Density vs Laser Power Meter
Output Voltage

- (5) FOV mapping; and
- (6) background and noise level determination.

These factors, and especially Factors 5 and 6, are discussed in further detail in this section.

Out-of-band rejection was also easily accounted for since the Si photodiode response cut off above 1.06 μm , and since solid rocket motor plume gaseous species radiate virtually negligible amounts within the Si spectral response (Ref. 8). Most radiation at these optical frequencies occurs with hot plume particle continuum radiation in addition to particle-scattered and particle-transmitted light from background sources. Figure 17 shows that even with 2000K particles emitting as a blackbody continuum, there is not much

DKCRNTT8T 23/MAR/84 TIME INTERVAL 0.0 - 21828.292

POWER SPECTRUM ST=0 0 0 18 ET=0 0 9 977

POHM SPS 249.25

UNFILTERED DATA

NPT 2484 BANDWIDTH 0.6021 DEG OF FREEDOM 12.00

SMOOTHED- HAMMING WINDOW 6 POINTS RMS 0.0185

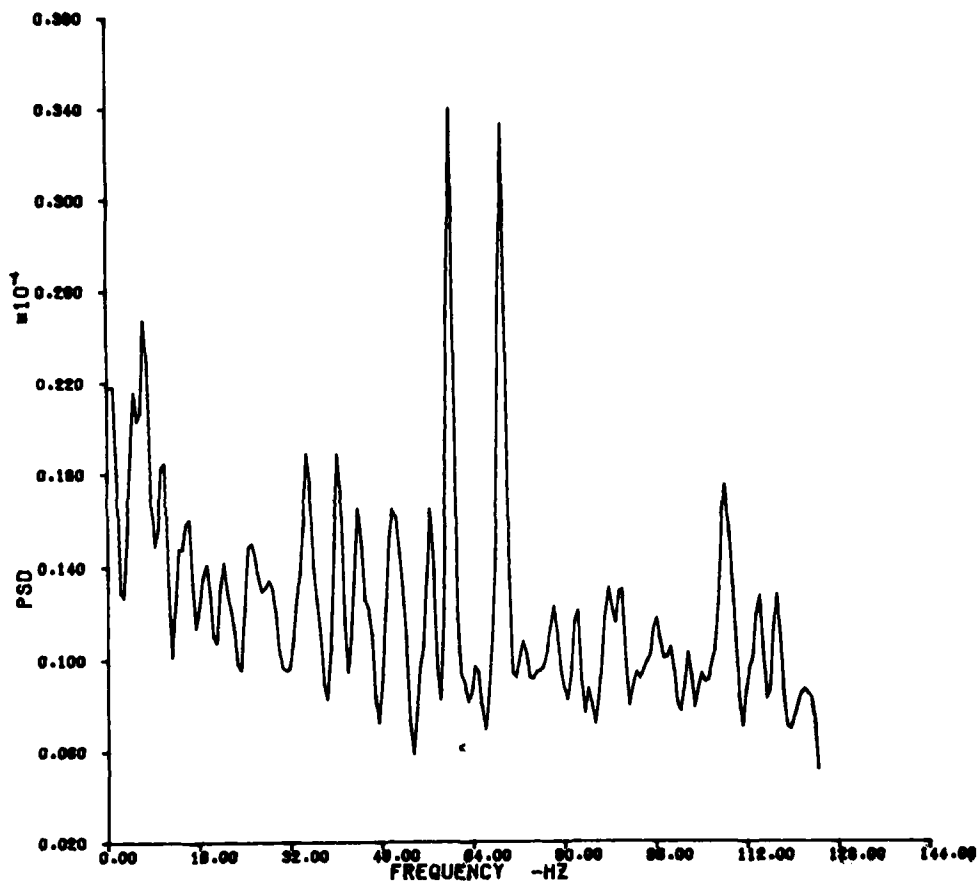


Figure 15. Laser Power Meter Output Voltage
Power Spectrum, Interval 1

radiative flux in the vicinity of 0.5 μm . This is further substantiated by the Naval Postgraduate School's experience with diffractively scattered light measurements (Ref. 9). Hence, out-of-band leakage is not a problem for the scattering detector--or for that matter, laser power meter--application.

OKCRNTTST 23/MAR/84 TIME INTERVAL 0.0 - 21829.292
 POWER SPECTRUM ST=0 0 10 503 ET=0 0 21 787
 POWH SPS 249.25
 UNFILTERED DATA
 NPT 2816 BANDWIDTH 0.6311 DEG OF FREEDOM 12.00
 SMOOTHED- HANNING WINDOW 5 POINTS RMS 0.0173

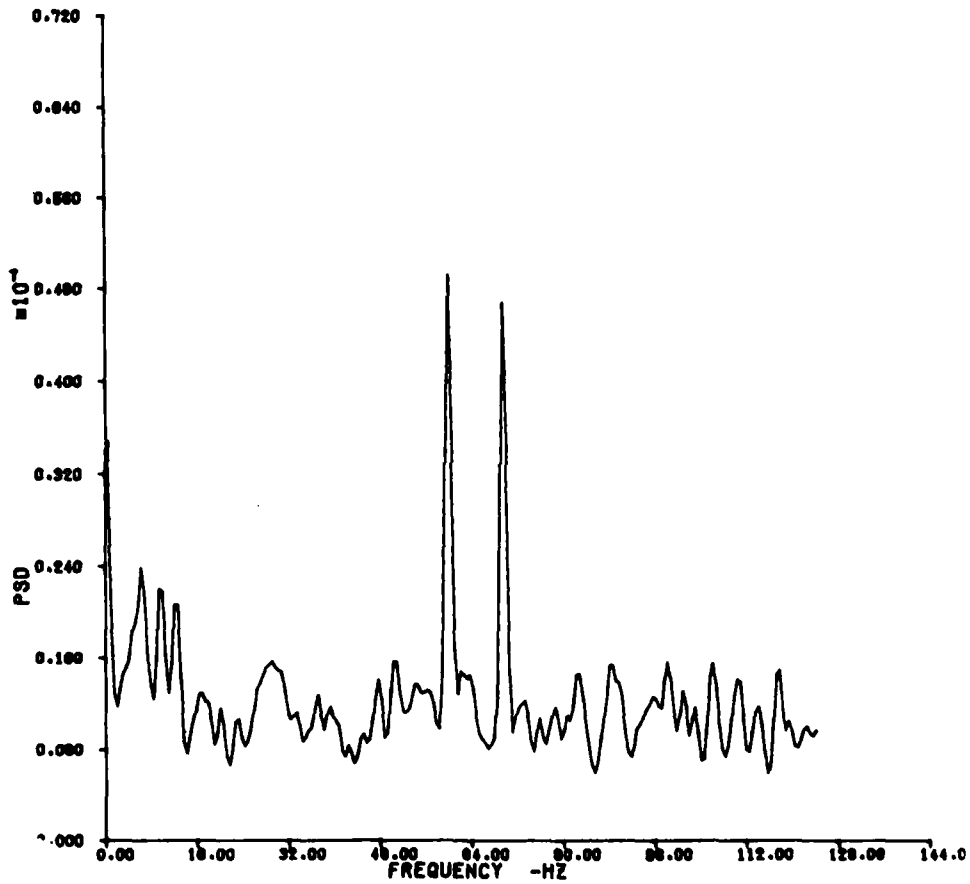


Figure 16. Laser Power Meter Output Voltage
Power Spectrum, Interval 2

The Si photodiode scattering detector 10-90% rise time was 2×10^{-7} s.
 Further scattering detector electro-optical parameters were given earlier in
 Table 4.

This brings us to the FOV mapping step in the scattering detector

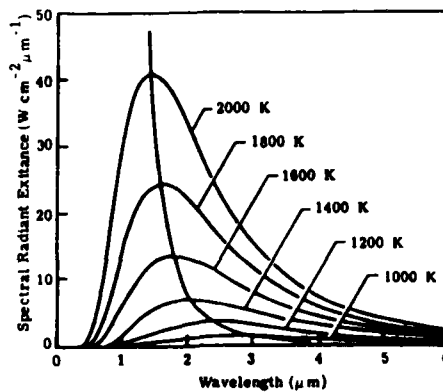


Figure 17. Blackbody Spectral Radiant Exitance Distribution
Curves for Temperatures Between 1000 and 2000K

calibration sequence. Ideally, a polar plot of the two-dimensional scattering detector radiometer FOV would be performed to quantify the instrument response as a function of incidence angle. This is essential to ascertain that no detector spatial detectivity anomalies exist and to define the normalization curves which characterize the spatial radiation distribution within each scattering detector's focal plane. This polar plot should be conducted with a collimated beam of sufficient intensity and small enough area to elicit a point-by-point detector system response.

The facilities to accomplish this (e. g., a long focal length collimator system) were unavailable to AFRPL at the time the BATES motor measurements described in this report were taken. In lieu of the polar plot, a one-dimensional FOV mapping calibration along the plume radial direction was performed for each firing. Because the detectors were intended to measure angular scattering intensities in the radial direction, the second dimension, plume axial direction, was determined to be of lesser importance. Detector response was measured as a function of distance along the plume radius. The mapping served as an alignment and focusing aid, but the scattering detector assembly afforded limited adjustment in the plume's radial direction.

The background and noise determination step in the calibration sequence was identical to that just reported in the laser power meter

calibration. Results of one such scattering detector dark current calibration are given in Figures 18-22. As with Figures 7 and 12, quantization effects are shown to be present due to a difference between the signal rate and data acquisition system time resolution.

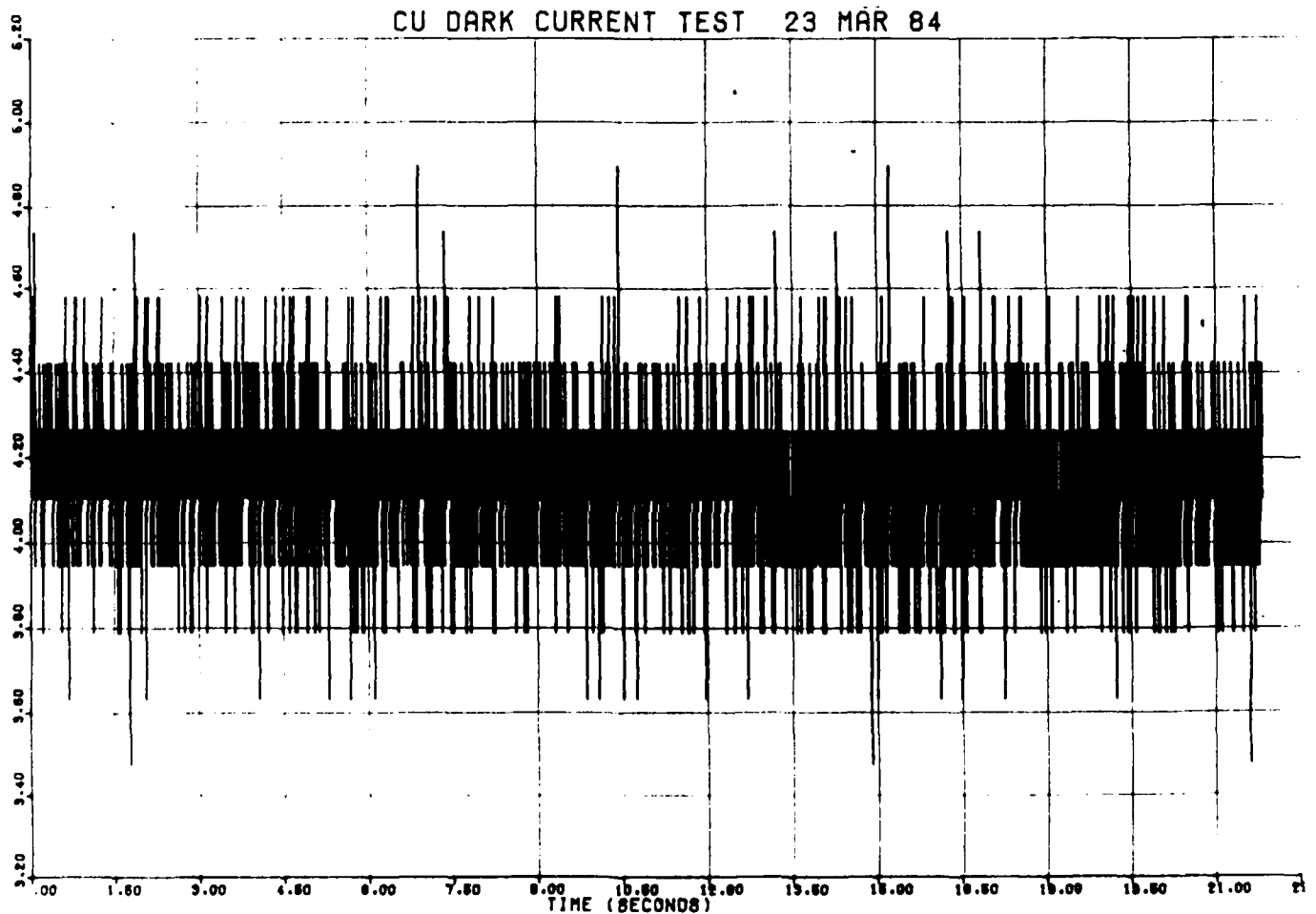


Figure 18. Scattering Detector 5 Output Voltage vs Time

Note the omnipresent 60 Hz noise spike which the calibration reveals. Although not clearly dominant, its elimination, as described earlier, involves searching characteristic AC sources.

2.3.2 Particle Collection Probes - In-vitro sampling of rocket exhaust particles has long been performed at AFRPL (Refs. 9-11). The objective was,

MEAN SQUARE	RMS	VARIANCE	CHI SQ	MEAN VALUE	STD DEV	MINIMUM	MAXIMUM	VALID OBS
17.988	4.170	0.022	999.00	4.167	0.149	3.474	4.885	2499 / 2499

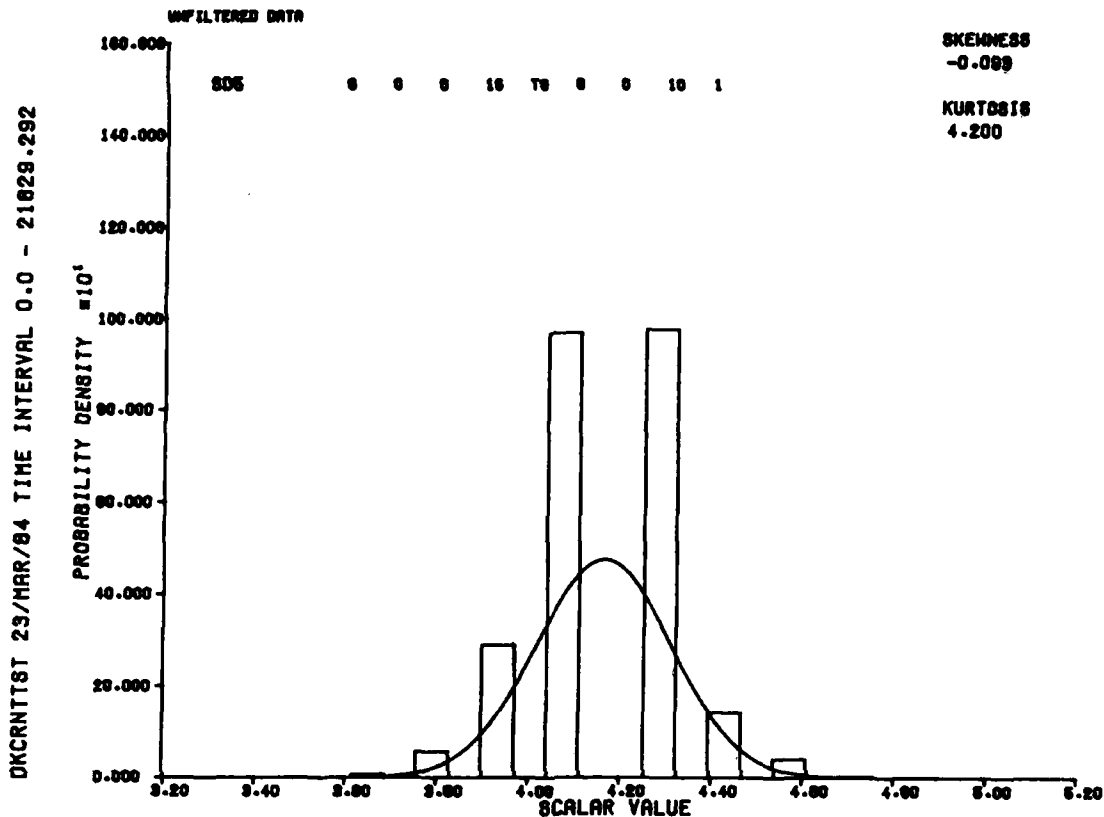


Figure 19. Probability Density vs Scattering Detector 5
Output Voltage vs Time, Interval 1

and is, to collect unbiased solid rocket motor exhaust particles to verify motor performance and plume signature prediction codes. The same aim was an ancillary objective of the present AFRPL effort, but a further goal--to correlate nonintrusive laser particle size measurements with probe-captured particle data--was sought. The now more pressing need to collect unbiased and undisturbed particles both in terms of size and surface morphology to verify the code gave emphasis to designing a supersonic shock-capturing probe. It is hoped that the new design will capture unbiased rocket exhaust particles in the field which has never been accomplished to any significant degree.

MEAN SQUARE	RMS	VARIANCE	CHI SQ	MEAN VALUE	STD DEV	MINIMUM	MAXIMUM	VALID OBS
17.100	4.146	0.029	999.00	4.143	0.161	3.474	4.665	2016 / 2016

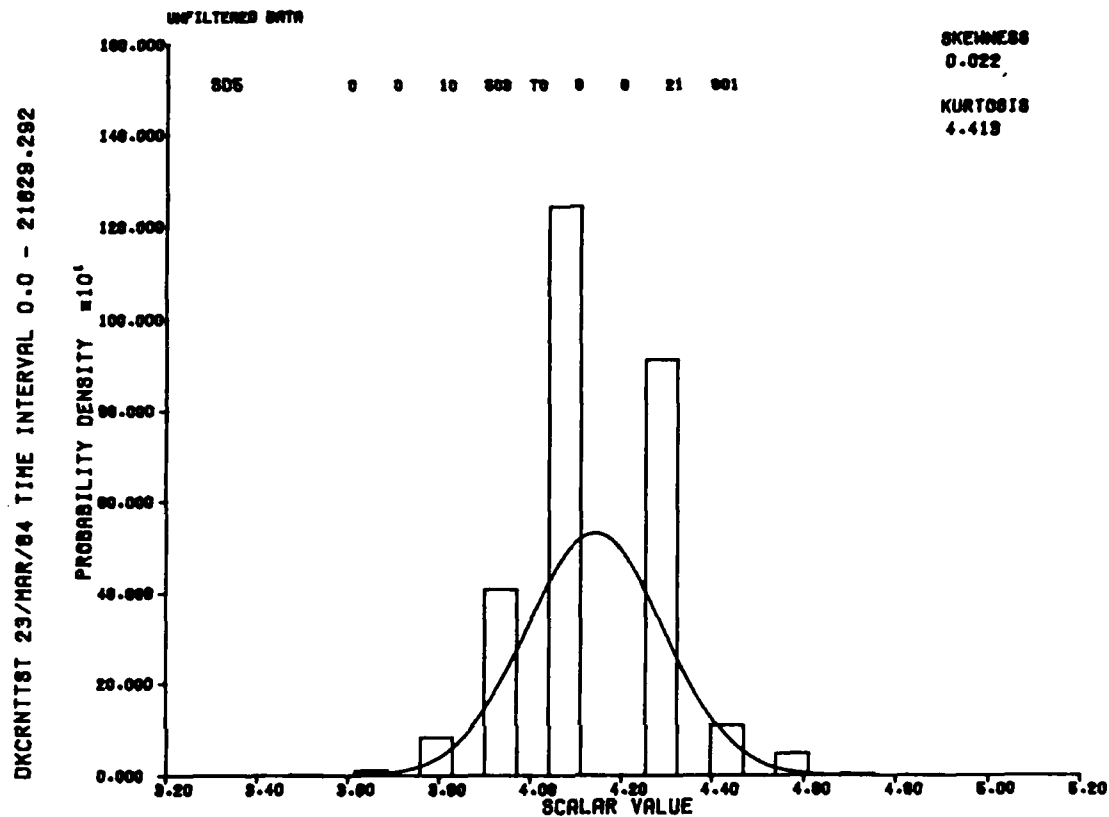


Figure 20. Probability Density vs Scattering Detector 5
Output Voltage vs Time, Interval 2

At least four basic problems must be solved to successfully extract an unbiased sample of particulates from a rocket exhaust. They are:

(1) the collection probe may bias the particle diameter measurement via bow shock and recirculation effects, changing the collected particle size distribution;

(2) particulate entrainment problems may introduce foreign particles into the flow;

(3) agglomerates of smaller particles may be broken up during collection and handling; and

DKCRNTST 23/MAR/84 TIME INTERVAL 0.0 - 21029.292
POWER SPECTRUM ST=0 0 0 16 ET=0 0 9 977
806 SP6 249.25
UNFILTERED DATA
NPT 2484 BANDWIDTH 0.6021 DEG OF FREEDOM 12.00
SMOOTHED- HANNING WINDOW 5 POINTS RMS 0.0410

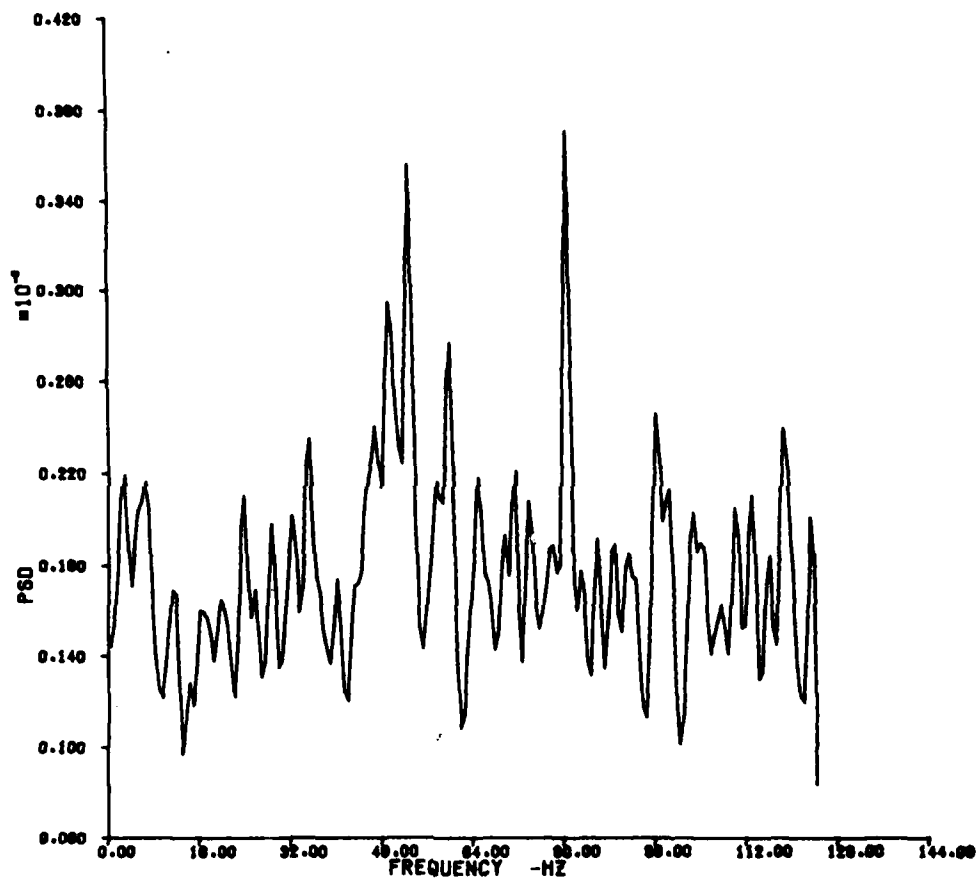


Figure 21. Scattering Detector 5 Output Voltage
Power Spectrum, Interval 1

(4) particles may continue to react after they have been captured, thus obscuring the true nature of their chemical composition while within the plume.

```

DKCRNTTST 23/MAR/84 TIME INTERVAL 0.0 - 21829.292
POWER SPECTRUM          ST=0  0  10  603  ET=0  0  21  787
SD5                      SPS 249.25
UNFILTERED DATA
NPT 2816   BANDWIDTH  0.6311  DEG OF FREEDOM  12.00
SMOOTHED-  HAMMING WINDOW  5  POINTS   RMS    0.0384

```

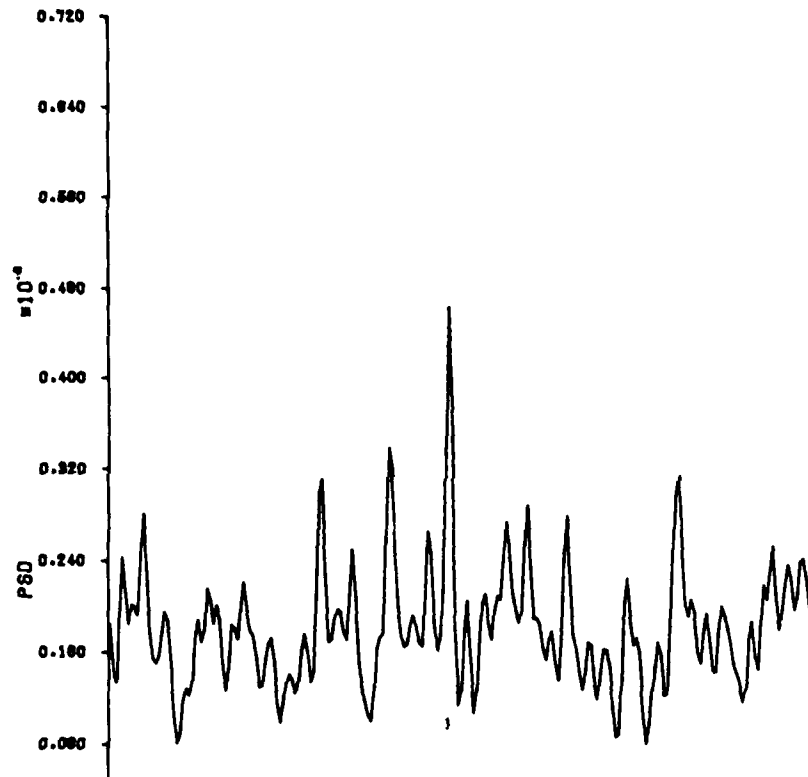


Figure 22. Scattering Detector 5 Output Voltage
Power Spectrum, Interval 2

A major advantage of intrusive collection techniques over the nonintrusive optical particle sizing means is that heavily-laden particulate flows can be investigated; optical thickness is of no concern.

Two intrusive flowfield particle collection probes are described in this section. The first, a subsonic particle collection probe, has been applied to a number of the firings described in this report. The latter, a

shockless supersonic inlet particle collection probe, has gone through its final design phase under the AFRPL particle sizing effort reported here.

Subsonic Particle Collection Probe Description - The AFRPL subsonic particle collection probe is the $36.5 \times 5 \text{ cm}^2$ torpedo-shaped aspirated tube shown in Figure 23. In its current application the probe is placed on the plume centerline and approximately seven meters downstream from the BATES nozzle exit plane. A portion of the subsonic plume flow is captured within the 0.5-cm entrance orifice and particles within this flow adhere to a number of 25-micron platinum wires strung in an assembly within the probe. Collected particles were then submitted for further analysis to a Nanometrics Model HPS 70 Field Emission Scanning Electron Microscope capable of 70\AA resolution photomicrographs. A Bausch and Lomb QMS image analyzer was also applied but with limited success, as described later in Section 3.1.

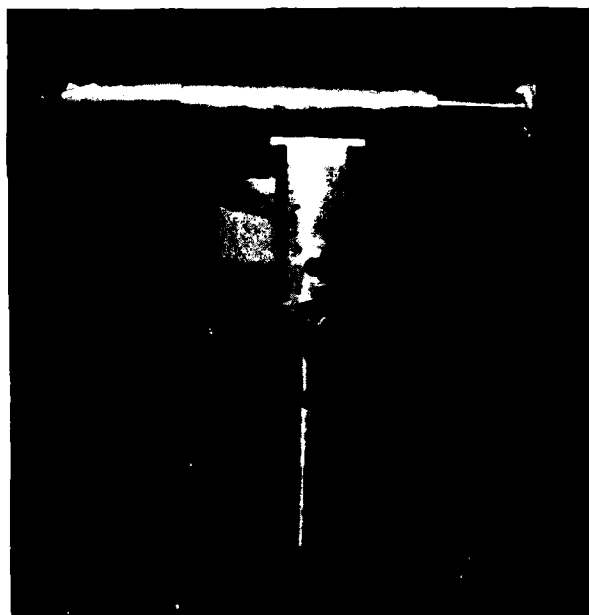


Figure 23. Subsonic Particle Collection Probe

The platinum wire collection assembly shown in Figure 24 represents an improvement implemented at AFRPL in July 1982. Prior to this, particles within the probe impacted on a blunt 2-cm diameter aluminum plug. When placed in the plume flow, a stagnation point was created at the center of the plug, with most of the particle-laden flow moving axisymmetrically around the collection surface, biasing the collection away from the smaller particles

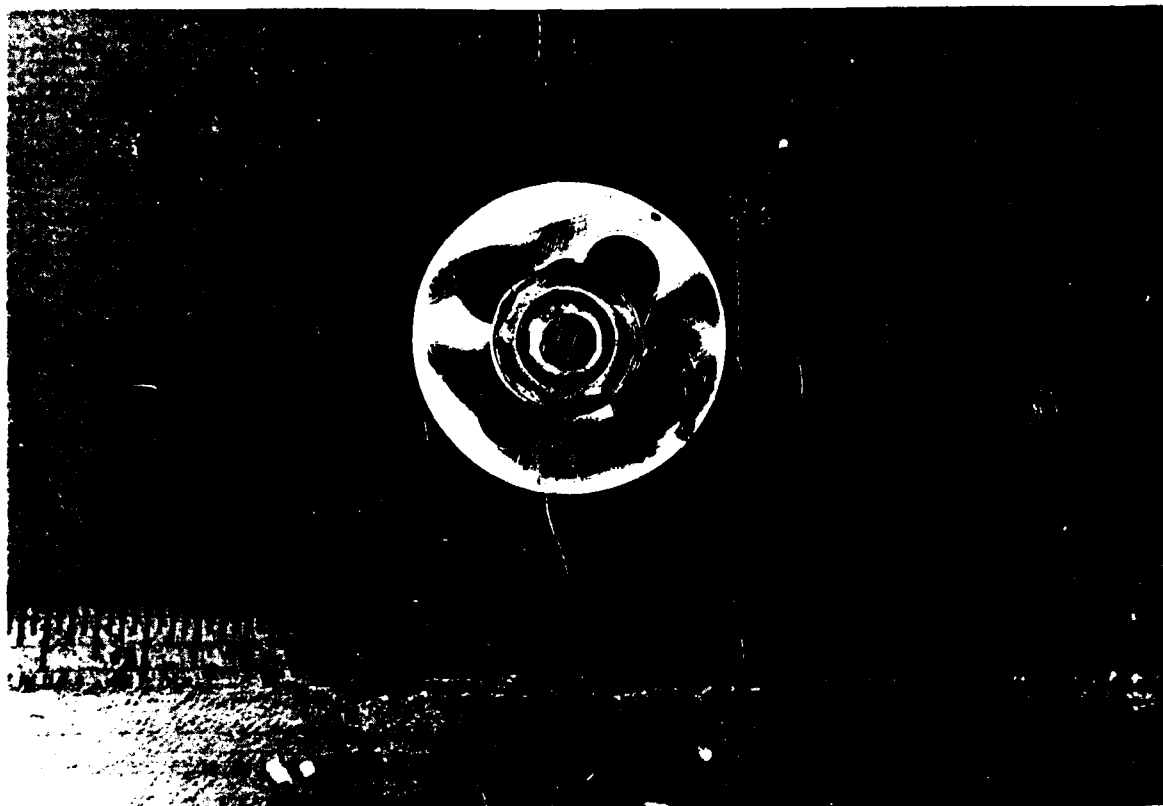


Figure 24. Platinum Wire Collection Assembly

which tend to follow the flow (Ref. 12). The small cross sectional area of the platinum wires alleviates much of this bias.

Despite the improvement, collected particles still tend to inaccurately represent plume flowfield particles because of collection methodology error sources such as particle agglomeration, bow shock, platinum wire impact, and particle handling effects. This points to the difficulty in accurately applying a sampling technique to rocket exhaust field measurements.

Supersonic Shock-Swallowing Quench Probe Description - Although it is virtually impossible to eliminate all of the effects, we can minimize them and construct a probe so that the extent of bias can be estimated.

The supersonic particle collection device has three objectives:

(1) to collect contaminated particles for chemical and surface property determination;

(2) to collect a particle sample whose total mass is not biased by the collection scheme; and

(3) to collect a particulate sample where particles do not pass through a normal shock which will help determine if particle agglomeration occurs to a statistically significant extent.

The particle capture probe shown schematically in Figure 25 attempts to address all these goals. The probe consists of a sharp tungsten tip designed to efficiently capture or swallow a stream tube of one gram per second of plume in a supersonic flow if the internal pressure is kept low. Similar tips designed by one of the authors at AEDC have been exposed to the supersonic flow of arc heated air at envelopes as high as 2000 B/lb and pitot pressures as high as 80 atm for periods of 1.0 second with no apparent ill effect. The performance of the tungsten tip in the highly erosive rocket engine particulate flow is not expected to be as good as has been obtained in "clear" air, so the tip has been made removable to facilitate its replacement and refurbishment.

To ensure that the probe does not stagnate the captured stream tube, a stream of cold nitrogen has been introduced to act as an ejector flow, thus reducing the tip exit pressure to 7.0 psia. The probe tip will be pumped through when the nitrogen is turned on. The plume flow ratio of 14:1 was selected to decelerate and quench the hot rocket motor plume particles. The specimen temperature is reduced to about 270 R to preclude burning the filter. The mixing passage flow rates and areas were sized to prevent formation of a normal shock at the design conditions. A series of oblique shocks will decelerate this combined flow to a slightly lower Mach number. A normal shock is expected to raise the static pressure to about the 30 psia required to force the captured rocket plume particles through the 0.025 μ m removable

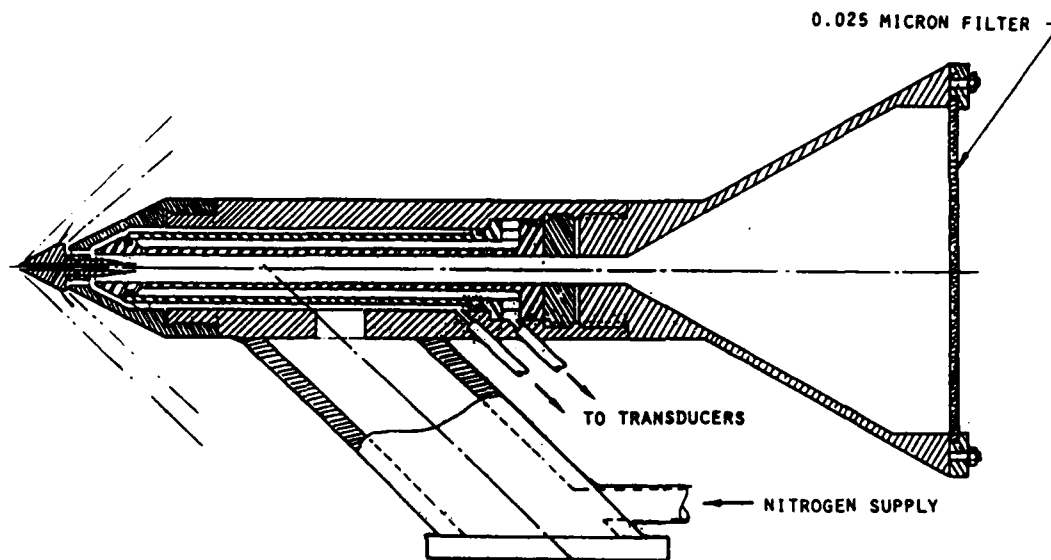


Figure 25. Supersonic Shock-Swallowing Quench Probe
(Filter Assembly Not to Scale)

millipore filter. A pressure passage has been provided to measure the gas static pressure at the point that the core flow discharges into the cold quench stream.

The removable micropore filter has been selected to collect up to a gram of particulate without creating undue filter pressure loss. The filter will be analyzed to determine the capture particulate diameter distribution. Since the expansion field will tend to separate the particulate as a function of diameter, a careful statistical analysis of the filter's PSDF will be made to determine the effect of the expansion process on the particulate input location.

Since the probe is designed to stay in the rocket plume flow for only 1.0 second, we have also designed a probe injection mechanism and shield. In practice the injector will rotate the probe into the plume flow during the motor firing to avoid the debris and ignitor smoke from the ignition transient. A shield will be rotated into the flow along with the probe to

ensure it is only exposed to the plume flow at a predetermined location in the plume. A pair of pneumatic actuators has been configured to rotate the probe and shield into and out of the flow and to cover and uncover the particle collection probe in the desired sequence. The probe stand is designed to be adjustable to accommodate a variety of rocket motor test stands at AFRPL.

The particle collection test sequence will begin by first collecting particles in the least severe area of the plume; thus our first objective of collecting uncontaminated particles will be achieved with little risk. On subsequent tests the probe will be located upstream of test nozzle Mach disks to obtain a sample with subsonic plume flow. If sufficient progress has been made, the probe will be redesigned internally to produce a completely isentropic internal flowfield to decelerate the particulates without a normal shock. This is so particulate agglomeration can be studied.

In addition to collecting particles for later analysis, the particle probe can be used to determine the particle mean flux and PSDF maps of the entire plume which can then be checked against the flowfield predictions. We can also obtain data on the distribution of impurities injected into the flow from ablative nozzle walls. The determination of the impurities such as carbon particles could be expected to have a large influence on plume radiation and may explain what has heretofore been consigned as anomolous plume radiation data.

2.4 Plume Signature Instrumentation

Plume signature instrumentation consisted of infrared and ultraviolet scanning monochromators used in application-specific configurations. These will be described in this section.

2.4.1 Infrared Emission/Absorption (IR-E/A) Instrumentation - IR-E/A measurement techniques have been successfully applied to yield specie temperatures and partial pressure profiles with long duration single-phase liquid rocket engines (Refs. 13 and 14), but the application to short duration two-phase solid rocket motors is unique to this AFRPL experiment. Because of the short (2-5 s) 15-pound BATES firing times, it was found necessary to

abandon the traditional IR-E/A multiposition spatial scanning technique described in Reference 13 and to work from a fixed position at the plume centerline near the motor exit plane. To compensate, it was decided to obtain multispectral data at the fixed IR-E/A station.

The physics behind the IR-E/A temperature and partial pressure inversion scheme is introduced in Appendix B of this report. The inversion technique adopted by AFRPL is described in Section 3.3 of this report.

Description - Schematics of the system layout with respect to the BATES motor and plume are shown in Figures 26 and 27 with Figure 26 showing the top view relative to a BATES 15-pound motor and Figure 27 representing the aft end perspective.

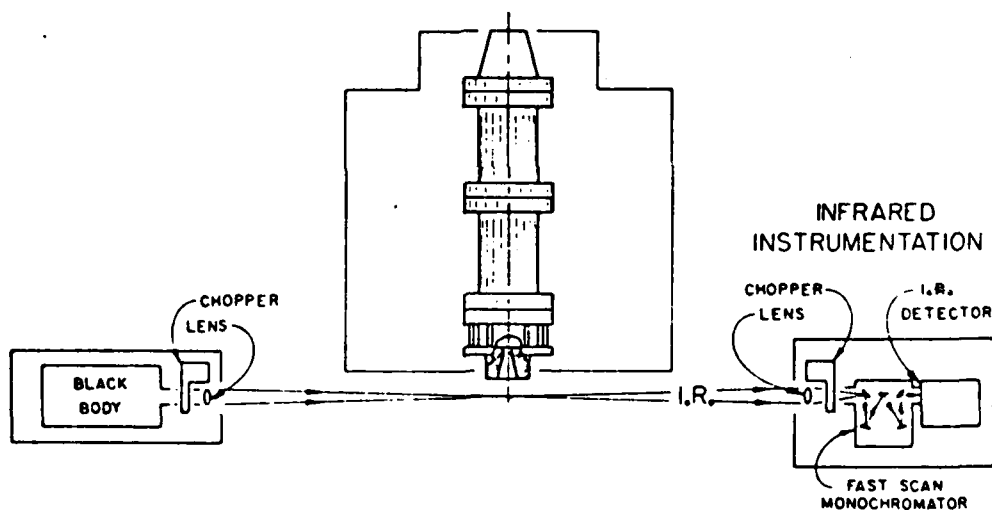


Figure 26. Top View of IR-E/A System

The radiation source system consisted of a 1-in aperture Barnes Model 11-210 blackbody radiation source set at 1000C. The source radiation was chopped at 1670 Hz and was focused to the plume centerline by a 10-cm focal length $f/2.5$ fused silica plano convex lens. The system is shown in Figure 27. A housing which could be flushed with gaseous nitrogen protected the system.

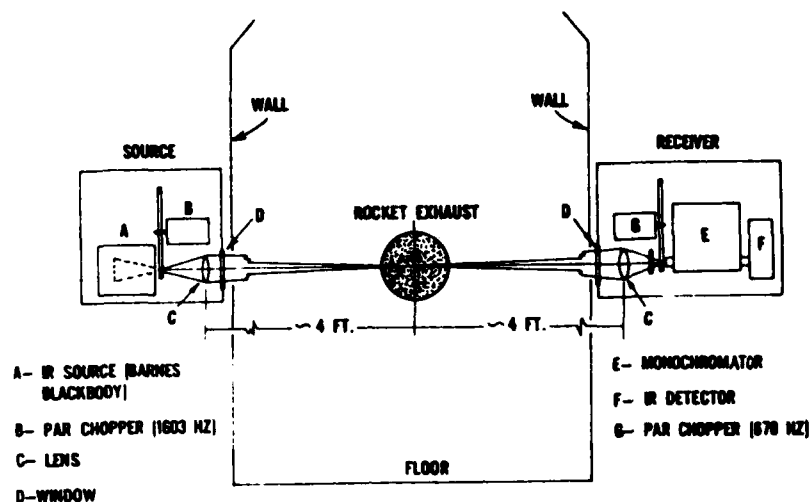


Figure 27. Aft-End View of IR-E/A System

The receiving system had a Spex Minimate Model 1670 grating monochromator with a 0.22-m focal length and f/4.0 aperture ratio, configured in a Czerny-Turner layout. The monochromator was equipped with a 300 grooves/mm diffraction grating blazed to operate with peak efficiency at the 2 μm wavelength. As was the source system, a PAR Model 125A optical chopper was in the optical train operating at 670 Hz. Condensing optics consisted of the identical fused silica lens found with the source system. Again, a protective housing with a fused silica window surrounded the system.

The monochromator was equipped with 18 mm high and 1.25 mm wide entrance and exit slits to provide 50 \AA resolution radiance to an ellipsoidal mirror attachment. The mirror focused the exit slit image onto a Santa Barbara Research Center Model 70750 C126 InSb detector. This detector later replaced the original Spex Model 1428 thermopile detector mainly because its sub- μs rise time (vs the thermopile's maximum 4-ms rise time) enabled it to adequately resolve the signals received from the fast grating scan.

The monochromator was modified to scan at 9 $\mu\text{m/s}$ over its design scan speed of 0.013 $\mu\text{m/s}$. To accomplish this, a cam was placed over the existing lead screw and attached to a sine bar which drove the kinematic grating mount

quicker than originally designed. The linear motion was preserved in the new design. A linear potentiometer was fitted to the drive mechanism to produce a voltage signal V_λ proportional to wavelength. A 24 V DC motor was also attached to the drive mechanism to permit the fast scan.

The receiver system was capable of a 50 \AA resolution scan from 1800 to 4900 \AA in 350 ms but operated from 2750 to 4250 \AA .

Signal Conditioning - The signal conditioning system is diagrammed in Figure 28. The preamplifier outputs an AC signal proportional to the radiation impinging the InSb detector. This detector signal was then carried through 300 ft of coaxial cable and, along with the source and receiver chopper synch channels, fed through two PAR Model 128A lock-in amplifiers. One lock-in amplifier was synchronized by a 1603 Hz source chopper and the other by the 630 Hz receiver chopper. In this way the analog transmitted source signal V_T and the radiance signal V_R were separated and then recorded simultaneously. These signals, along with the grating drives potentiometer signal V_λ , were recorded on magnetic tape at 250 samples/s using a NOVA Datum digital data acquisition system.

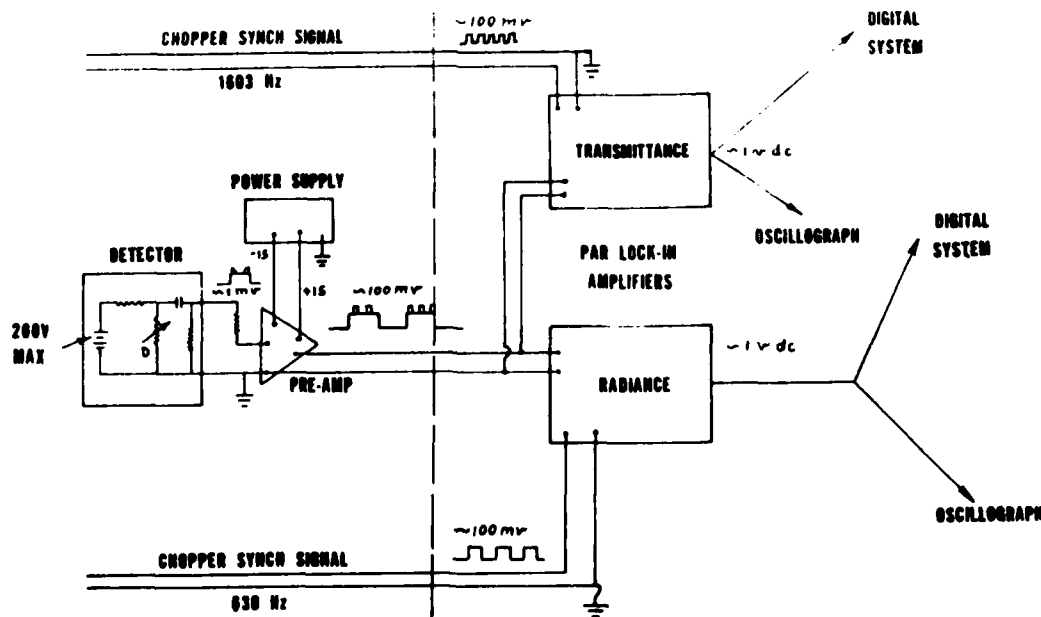


Figure 28. Block Diagram of Signal Conditioning System

Calibration - Absolute spectral positioning was initially accomplished by inserting a 1200 grating/mm ultraviolet/visible grating in place of the 300 grating/mm grating used in the measurement. A low pressure mercury lamp source was then focused into the monochromator's entrance slit and the motorized scan drive was actuated. The voltage applied to the drive mechanism's potentiometer V_{in} was recorded along with the potentiometer wiper voltage V_{λ} and the detector response voltage V_R . Characteristic Hg line peaks at 2536.52, 3131.55, 3663.28 and 4046.56 \AA were then discriminated in a $V_R(V_{\lambda})$ plot. Since the diffraction grating ruling ratio of 4 holds with a 1200 gratings/mm substitution for the 300 gratings/mm calibrating grating, it follows that V_R peaks occur at V_{λ} 's corresponding to 1.01, 1.25, 1.47 and 1.62 μm . Although these wavelengths are at the low end of both the 1200 gratings/mm grating efficiency curves and the InSb spectral response, they sufficed as initial curve fit points for the function.

$$\lambda = a (V_{\lambda}/V_R) - b \quad (1)$$

The wavelength λ , determined by the particular calibration a and b curve fit constants and output voltages V_{λ} and V_R , gave the absolute spectral positioning for the corresponding BATES firing data. Implicit in this linear form curve fit is the assumption of a linear relationship between V_{λ} and V_R (i. e., the potentiometer's wiper voltage linearly corresponds to likewise linear drive mechanism and kinematic grating mount motions).

To eliminate the effects of radiation from secondary orders of diffraction, three long pass blocking filters set at 1.5, 2 and 3.5 μm were designated to be set in the monochromator's optical path with cut-on wavelengths depending on the desired scan spectral interval. Only radiation from the first order free spectral range was allowed through.

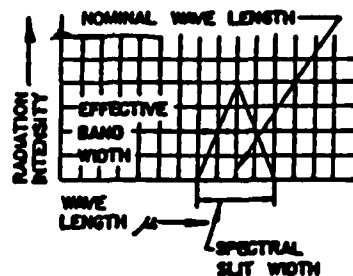
No FOV mapping was undertaken with this instrument because the necessary collimator was unavailable to AFRPL at the time these measurements were taken. In addition, spatial modulation of the signal was assumed to be a relatively insignificant error source because of the characteristic uniform response over the InSb detector's small active detection surface area.

As noted previously, the monochromator's 1.25-mm wide slits give a 50 Å optical resolution. Because of its spectral scan from 1.8 to 4.9 μm, the instrument's resolving power R, defined as

$$R = \lambda / \Delta\lambda , \quad (2)$$

ranged from 360 to 980.

The 50 Å spectral slit width defines the width of the theoretical triangular radiant energy slit function and is illustrated in Figure 29.



2 : EFFECTIVE B.W. = SPECTRAL S.W.

Figure 29. Theoretical Distribution of Radiant Energy with Wavelength Exit Slit

This theoretical triangular radiant energy distribution indicates that a peak-normalized bandwidth could be employed in determining the flux measured by the monochromator. With this peak normalization technique the effective 50 Å slit width was centered about a specific wavelength which was dependent on scan position. The peak power which occurs at this wavelength was normalized such that an "energy rectangle's" height was defined. Hence, the instrument's spectral responsivity $R(\lambda)$ is made equal to the width of the rectangle $R(\lambda)$ enclosing an area equal to the integrated area under the true $R(\lambda)$ area. This normalization procedure can also be used when calculating the monochromator's calibration transfer function.

The blackbody's equation for radiance $N_{\Delta\lambda}(T)$ is

$$N_{\Delta\lambda}(T) = \int_{\delta_1}^{\delta_2} \frac{c_1}{\lambda^5 (e^{c_2/\lambda T} - 1)} d\lambda \quad (\text{Wcm}^{-2}\text{sr}^{-1}) \quad (3)$$

where

$$\lambda_1 = \text{cut-on wavelength (cm)}$$

$$\lambda_2 = \text{cut-off wavelength (cm)}$$

$$c_1 = 2\pi c^2 h = 3.741832 \times 10^{-12} \text{ (Wcm}^2\text{)}$$

$$c_2 = hc/k_b = 1.438786 \text{ (cmK)}$$

$$T = \text{blackbody source temperature (K)}$$

Equation 3 does not have a closed form solution and must be solved through a geometric series expansion before $N_{\Delta\lambda}(T)$ can be input into Equation 3 (Ref. 15). The wavelength interval between λ_1 and λ_2 is the monochromator's spectral response given earlier. The error introduced by bandwidth normalization is quantified when calculating the monochromator's absolute responsivity.

The normalized absolute responsivity $R(\lambda)$ over a fixed bandpass $\Delta\lambda$ is the ratio of the instrument output voltage to the irradiance $E_{\Delta\lambda}$ or radiance $L_{\Delta\lambda}$ of the calibration source, i. e.,

$$\overline{R(\lambda)} = V_{\text{cal}}/E_{\Delta\lambda\text{cal}} \quad \text{or} \quad L_{\Delta\lambda\text{cal}} \quad (4)$$

Hence, the in-band irradiance or radiance of a source can be computed from

$$E_{\Delta\lambda\text{source}} \text{ or } L_{\Delta\lambda\text{source}} = V_{\text{cal}}/R(\lambda). \quad (5)$$

Linearity is implicit in Equations 4 and 5.

Radiance from a 1000 C-rated Barnes Model 11-210 blackbody radiation source with an emissivity ϵ of 0.99 ± 0.01 and a 0.5-inch cavity aperture was used in the absolute responsivity calibration.

Hence, the plume in-band radiance relative to the system transfer function K_s is essentially a function representing the product of the

normalized absolute responsivity $\overline{R(\lambda)}$ and its associated uncertainties, shown in Equation 6 with an uncertainty factor U:

$$K_s = \overline{R(\lambda)}U = N_{\Delta\lambda}(T)/V_{cal}, \quad (6)$$

where

$N_{\Delta\lambda}(T)$ = blackbody radiance determined from Equation 3; and

V_{cal} = calibration radiance channel voltage.

The ensuing system transfer function K_s is necessary for calibrated data reduction of ensuing plume radiance measurements.

The uncertainty factor U is comprised of:

(1) uncertainty in determining the calibration constant K_s , which includes source uniformity and alignment uncertainties in the calibration system's optical transmission and inadequate out-of-band rejection;

(2) effects due to the unknown plume spectral intensity curve (i. e., spectral peaks)--this is largely mitigated by the linearly responding instrument;

(3) radiation from outside the monochromator's IFOV contributing to the measured radiance;

(4) plume test pad interactions arising from flowfield impingement onto the ground and reflections of radiation from the pad walls; and

(5) window contamination changing the calibration constant.

The relative uncertainties of Items 1 and 2 are discussed in detail in Reference 16, including a method to calculate the effects. As mentioned, Effect 3 is minor with a flatter monochromator response curve $R(\lambda)$. However,

the magnitude of Effect 4 is unknown. Uncertainty caused from Effect 5 can be reduced through frequent calibration and window cleaning.

2.4.2 Ultraviolet (UV) Instrumentation - BATES plume UV spectra are of interest both to help verify solid propellant combustion models, and more basically, to better construct a plume UV radiation model by identifying the species that radiate in the UV. Laboratory UV emission spectroscopy is being undertaken at AFRPL with selected solid rocket motor composite propellants (Ref. 17) and at Grumman Aerospace Corporation with shock-heated Al_2O_3 particles (Ref. 18). UV measurements have also been taken with rocket motors (Refs. 19 and 20). Reduced and minimum smoke propellant motors, however, have never been instrumented for UV measurements until this AFRPL application.

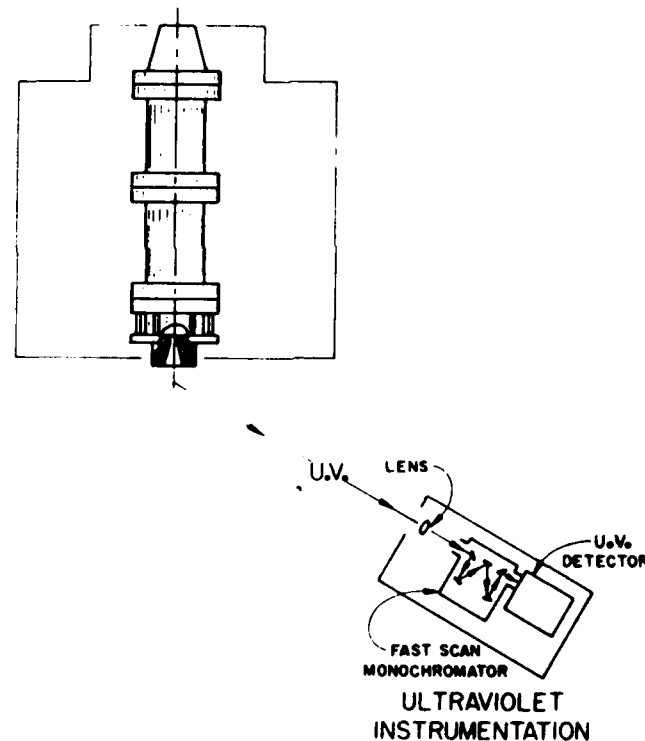


Figure 30. Top View of UV Measurement System

Description - The UV measurement system is depicted in Figure 30. It is a receiving system only, consisting of a Spex Minimate Model 1670 grating monochromator and associated optics, and identical in every way to the IR-E/A

receiving unit except that a BaF1 window and a 1200 grooves/mm diffraction grating blazed to operate with maximum efficiency at 3000 \AA were inserted in place of a fused silica window and a 300 grooves/mm grating. Also, a RCA 1P28 photomultiplier tube rated at a spectral response exceeding 40 m/A/W from $2600\text{--}4300 \text{ \AA}$ was used in lieu of the IR-E/A systems's InSb detector. Radiation from the monochromator exit slit was focused onto the photomultiplier tube's photocathode.

The monochromator's 1.25-mm entrance and exit slits were set for a 50 \AA spectral resolution. The 100-ms $2750\text{--}4250 \text{ \AA}$ spectral scan was accomplished at a rate of 15 m/s via the same drive mechanism detailed in Section 2.4. The difference in scan speed was accounted for by a different cam attachment.

Signal Conditioning - Only three voltage signals needed to be recorded: the UV monochromator's drive mechanism's input voltage, $V_{uv\lambda in}$; the $V_{uv\lambda}$ signal corresponding to the UV monochromator potentiometer's wiper voltage; and the $V_{uv\lambda}$ voltage corresponding to the photomultiplier's response to the radiation focused on its detection surface. These signals are sent through 300 ft of coaxial cable to the control room for digital data sampling and recording at 250 samples/s through a 100 Hz filter.

Calibration - Absolute spectral positioning was accomplished in a manner similar to the IR-E/A system described in Section 2.4.3. $V_{uv\lambda in}$ responses to 3131.55 , 3663.28 and 4046.56 \AA Hg line peaks were mapped vs $V_{uv\lambda}$ response outputs, giving a relationship between $V_{uv\lambda in}$ and $V_{uv\lambda}$ when Equation 1, $\lambda = a (V_{uv\lambda in}/V_{uv\lambda}) - b$, is used in a linear curve fit. This established an absolute spectral positioning calibration.

Figure 31 illustrates the dominance of first order radiation in the spectral region used here, eliminating the need for blocking filters.

As noted in the description of the IR-E/A system, the 50 \AA spectral resolution defines the extent of the theoretical triangular radiant energy distribution. Again, the spectral response function $R(\lambda)$ was peak normalized and set at a rectangle whose height was defined at $\overline{R(\lambda)}$. The monochromator's

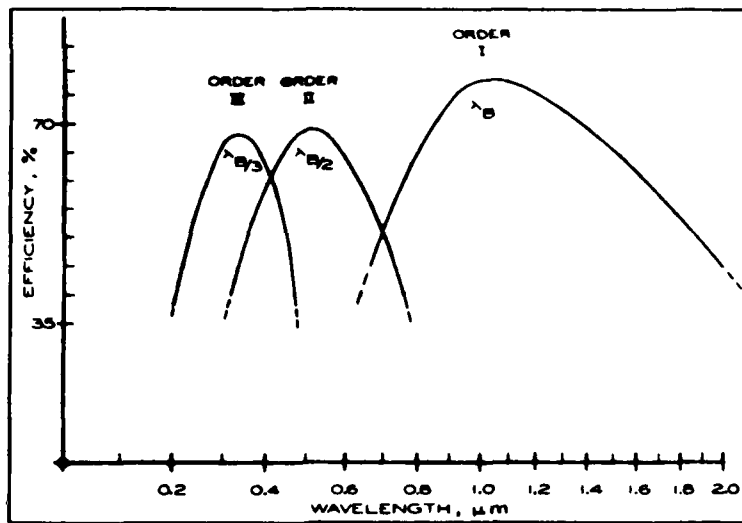


Figure 31. 1200 Grooves/mm Diffraction Grating
Efficiency vs Wavelength

resolving power as defined by Equation 2, ranged from 25 and 85 between 2750 and 4250 Å.

There is not much radiant power from a 1000 C blackbody source falling within the 2750-4250 Å spectral range, but the system calibration function K_g was still calculable using the procedure outlined in Equations 2-6. Recognizing the potentially low signal-to-noise ratio with a blackbody-based absolute response calibration, a quartz-halogen calibration source was originally proposed. However, the blackbody source was found to be sufficient.

The same contributions to uncertainty in determining the absolute spectral response that were enumerated in Section 2.4.3 also exist here. Reference 16 describes how they were incorporated in UV radiance calibration calculations.

3.0 DATA REDUCTION AND RESULTS

Data reduction methodologies and results are presented in this section. Any difficulties in retrieving data, either from instrumentation problems or data inversion techniques are mentioned in this section as they strongly impact results. The four measurement areas presented here are:

- (1) plume visibility figure of merit;
- (2) plume particle sizing;
- (3) plume temperatures and partial pressures; and
- (4) plume UV signatures.

3.1 Plume Visibility Figure of Merit

3.1.1 Introduction and Data Reduction Method - One propellant ranking criterion is plume visibility. This is of especial concern with low visibility reduced and minimum smoke solid rocket formulations. In conjunction with an ongoing low visible signature tactical rocket motor grain formulation development effort, AFRPL has undertaken solid rocket motor exhaust plume visibility studies (Refs. 21 and 22).

An experimental technique from which some plume visibility figures of merit could be deduced would greatly benefit AFRPL's low visibility propellant development projects. The difficulty encountered is devising measurements which correlate well with primary and secondary smoke levels under flight conditions. To address this issue AFRPL has developed an analytical computer code aimed at evaluating various plume visibility screening methods (Ref. 23). Future efforts with radiometric plume characterization measurements are planned.

It was thought that the laser transmissometer measurement could be applied as a plume visibility screening method. Major contributors to primary

smoke visibility are the particle optical properties which control the plume's nearfield contrast. Contrast is a function of scattered and absorbed light. The particle optical properties which determine scattering--particle size, the real index of refraction, and the absorption coefficient--are also the factors which determine laser beam transmittance. Moreover, particle density is an affecting parameter in both plume visibility and laser transmittance; these two effects are related and described by Mie theory (Appendix A). In fact, all primary smoke plume visibility factors except afterburning mechanisms relate to laser beam transmittance.

There are major drawbacks in applying the laser transmissometer experiment in this way. Secondary smoke arising from water and acid condensation in the plume farfield is not addressed, nor is the presence of ignition smoke or plume scattering from either direct or diffuse sunlight considered. Also, the firings under this project are static; flight conditions, which have a major impact on the plume flowfield and therefore the visible signature, are not accounted for. The laser transmission is made only from the 90° aspect angle, hence ignoring other radiative flux directions which contribute to total plume visibility (such as the rocket chamber "searchlight" effect and the very real angular dependence of light scattering). Additionally, laser transmission is monochromatic, and although the particle optical properties on which transmittance is dependent apply to other visible wavelengths, the mathematical scattering efficiency functions describing Mie theory are transcendental and highly sensitive to wavelength as well as particle size and aspect angle. A final point which is actually a combination of the drawbacks listed above is that any correlation between laser beam extinction, its application as a secondary measure of primary smoke to the ultimate plume visibility criterion, total plume detectability, has not been undertaken. This is the bottom line which a plume visibility screening figure of merit must address.

It was decided to apply the laser transmittances from the AFRPL particle size measurements to assess plume visibility with the above caveats taken into account. Laser transmissometer instruments and geometry were detailed in Section 2.3.1 of this report.

3.1.2 Transmissometer Results and Interpretation - Laser transmission data was successfully collected for 29 firings. In each of these firings the laser action period was divided into ten intervals, excluding the time interval the shutter breaker blocked the laser output. The mean transmissivities of these intervals and the one sigma values are recorded in Table 5 as well as the mean transmissivities and standard deviations within each propellant group. Note that while these mean transmissivity numbers may reflect accurate figures of merit for a large ensemble, the small samples and the variations of nozzle geometries here detract from a straightforward comparison of different types of propellants. The uncertainties are reflected in the propellant series' standard deviations but only to the extent of sample size and only in cases where sample size exceeds one. It may not be possible to ascribe the one sigma statistical description of the mean transmissivities to a visibility criterion because all sample sizes are small.

Considering the just mentioned caveat, interesting transmissivity (and therefore, plume visibility) comparisons can still be made. Table 5 lists three reduced smoke sidewinder propellants. Reviewing each propellant formulation's mean transmissivity τ_p and the data quality privisos, both AFRPL RSS ($\bar{\tau}_p = 83.054$) propellant plumes are attenuated to a greater extent with our Ar^+ laser transmissometer $0.5145 \mu m$ than is Aerojet's RSSA formulation. By this measure only, it appears Aerojet's RSSA formulation's plume is less visible.

Similarly, of the propellant formulations tested without solid additives, the MSMP-4 ($\bar{\tau}_p = 96.474$) and DWP ($\bar{\tau}_p = 96.429$) formulations proved superior in our visibility figure of merit than did KKN ($\bar{\tau}_p = 92.389$) or RS GAP 80 ($\bar{\tau}_p = 90.538$). It must be noted that the RS GAP 80 transmissometer experiment was configured with the laser beam path 2 cm (instead of 2 m) from and parallel to the nozzle exit plane.

It is important to once again point out that a true statistical description of representative plume laser transmission for each of the propellant types tested was not accomplished with the limited data presented

Table 5. Transmissivities for 29 15-Pound BATES Motor Firings

AFRPL MOTOR IDENTIFICATION	PROPELLANT	TRANSMISSIVITY ($\% \tau$)	σ_{τ}	PROPELLANT MEAN TRANSMISSIVITY	
				$\% (\tau_p)$	$\bar{\sigma}_{\tau}$
144B-008	*RSS	83.049	0.88	83.049	---
179B-001	*RSSA	88.970	1.08	91.695	3.68
179B-004	*RSSA	94.169	1.03	91.695	3.68
194B-001	*ARCOCEL-423	87.157	5.40	84.054	4.39
194B-002	*ARCOCEL-423	80.951	1.74	84.054	4.39
240B-004	CWB (DTS-9886)	85.673	2.34	85.673	---
241B-001	KKN (DTS-9889)	94.968	0.750	92.389	2.89
241B-002	KKN (DTS-9889)	95.886	1.35	92.389	2.89
241B-004	KKN (DTS-9889)	89.371	2.04	92.389	2.89
241B-005	KKN (DTS-9889)	90.281	1.32	92.389	2.89
241B-006	KKN (DTS-9889)	91.441	0.830	92.389	2.89
242B-001	DWP (TPH-8289)	95.573	1.76	96.429	1.73
242B-002	DWP (TPH-8289)	94.710	1.27	96.429	1.73
242B-003	DWP (TPH-8289)	99.194	0.700	96.429	1.73
242B-005	DWP (TPH-8289)	93.039	3.00	96.429	1.73
242B-007	DWP (TPH-8289)	96.571	1.24	96.429	1.73
242B-008	DWP (TPH-8289)	99.179	0.843	96.429	1.73
242B-009	DWP (TPH-8289)	95.728	1.99	96.429	1.73
242B-010	DWP (TPH-8289)	97.514	1.78	96.429	1.73
242B-011	DWP (TPH-8289)	96.389	2.68	96.429	1.73
242B-013	DWP (TPH-8289)	95.315	3.95	96.429	1.73
242B-016	DWP (TPH-8289)	94.334	1.01	96.429	1.73
242B-018	DWP (TPH-8289)	98.158	0.432	96.429	1.73
242B-019	DWP (TPH-8289)	95.123	2.36	96.429	1.73
242B-020	DWP (TPH-8289)	95.123	2.36	96.429	1.73
242B-022	DWP (TPH-8389)	97.728	1.09	96.429	1.73
242B-023	DWP (TPH-8289)	97.562	1.26	96.429	1.73
248B-001	MSMP-4	96.474	0.704	96.474	---
262B-005	RS GAP 80	90.538	3.39	90.538	---

*These are reduced smoke sidewinder propellants. Firing number 144B-008 was an AFRPL formulation with 0.5 weight percent Al additive loading; the 179B-series was an Aerojet formulation with 0.5 weight percent ZrC; and the 194B-series was an ARC formulation with 1.0 weight percent ZrC (Ref. 1).

here; hence, the extent of error in the above observations cannot yet be reported. In addition, the link between plume transmissivity and an accurate visibility figure of merit option is not established.

One final point: previous efforts to accurately correlate the mean particle diameter to such motor and performance parameters as nozzle throat diameter, particulate concentration within the motor chamber, average chamber pressure and average chamber residence time (Ref. 24) arose from observing

that a reasonable single-variate correlation between the particle and nozzle throat diameters may exist (Ref. 25). This leads to the possibility that a relationship between transmissivity and these parameters may exist. Data scatter, however, was the limiting factor. On second glance some data scatter would appear reasonable. The relationship between laser transmissivity and mean particle diameter is not only logarithmic but also depends on the difficult to solve Mie theory equations. This will be shown in Section 3.2.1.

3.2 Plume Particle Sizes

3.2.1 Transmissometer Data Reduction Methods - The laser transmission/scattering measurement described in Section 2.3.1 present the in-situ particle sizing data described in this section. Two data reduction schemes were envisioned to deconvolve the measured angular and transmitted light intensities to particle sizes: an AEDC-supplied computer code designed to yield PSDF histograms and an Aerospace Corporation-contracted computer code designed to yield mean particle sizes. For reasons to be shown in this section only the second of these techniques, the Aerospace Corporation method, was used to retrieve particle sizes.

The AEDC-supplied size deconvolution code (SIZFRED) (Ref. 26) input parameter requirements were used to help design the AFRPL laser scattering configuration. SIZFRED was generically designed to yield PSDF bins from angularly scattered and orthogonally polarized light incident on a multiangled array of signal detection channels, all normalized by the radiation intensity from an unpolarized 90° scattering channel. The laser light was to be initially oriented 45° to the scattering plane so both parallel and perpendicular components would be present, thus simulating unpolarized light. The scattering volume was to be narrowly defined by a focused array of detectors. The AFRPL scattering measurement apparatus was modeled in this way.

SIZFRED was later modified to two families of computer codes: (1) MIESTEP, which calculates Mie functions for the polarization states given the detection angular positions and FOV's; and (2) SIZIM, which performs the

PSDF deconvolution from the MIESTEP data tape through a modified Phillips-Twomey (Ref. 27) constrained linear inversion technique.

Although the two codes are described in some detail by Curry (Ref. 27), explanations of Mie scattering theory and the constrained linear inversion numerical method are in order to explain the applicability of the AEDC deconvolution methods to the AFRPL laser scattering experiment. The tenants of Mie scattering as they specifically apply to the AFRPL plume particle sizing effort are given in Appendix A.

To understand the constrained linear inversion technique one must recognize that the scattered intensity components can be written as Fredholm integral equations in the form (Ref. 28)

$$G_i(y_i) = \int_0^{\infty} K(y_i, D) dD. \quad (7)$$

In this specific particle sizing application, the scattering intensity components for each scattering detector are Fredholm integral equations of like form:

$$I_{\perp}(\theta) = C \int_0^{\infty} \sigma_{p_{\perp}}(\theta) n(\alpha) d\alpha \quad (8)$$

and

$$I_{\parallel}(\theta) = C \int_0^{\infty} \sigma_{p_{\parallel}} n(\alpha) d\alpha \quad (9)$$

where

θ = scattering detector aspect angle,

C = scattering detector absolute spectral response calibration constant,

$\sigma_{p_{\perp}, \parallel}(\theta)$ = differential scattering cross sections;

α = dimensionless size parameter

$\alpha = 2\pi r/\lambda$ where r is particle radius; and

$n(\alpha)$ = particle size distribution function.

An explanation of the terms θ , σ_p , α and $n(\alpha)$ is contained in Appendix A.

The constrained linear inversion technique embodied in SIZIM essentially begins with the polarization intensity ratio definition:

$$P(\theta) = \frac{I_{\perp}(\theta) - I_{\parallel}(\theta)}{I_{\perp}(\theta) + I_{\parallel}(\theta)} \quad (10)$$

Substituting Equations 8 and 9 into Equation 10 yields the relation,

$$P(\theta) = \frac{\int_0^{\infty} \sigma_{p_{\perp}}(\theta)n(\alpha)d\alpha - \int_0^{\infty} \sigma_{p_{\parallel}}(\theta)n(\alpha)d\alpha}{\int_0^{\infty} \sigma_{p_{\perp}}(\theta)n(\alpha)d\alpha + \int_0^{\infty} \sigma_{p_{\parallel}}(\theta)n(\alpha)d\alpha} \quad (11)$$

which explicitly relates measured data $P(\theta)$ to the PSDF $n(\alpha)$. The PSDF is retrieved from the equation through the Phillips-Twomey constrained linear inversion method. The method is modified to provide a linear solution for the nonlinear Equation 11. The PSDF $n(\alpha)$ is retrieved by first holding the numerator constant and solving for $n(\alpha)$, then holding the denominator constant using the just-retrieved $n(\alpha)$ as an iteration starting point. This recursive approach is terminated upon convergence to a solution.

Young (Ref. 29) has approached what is essentially the solution of Equation 11 differently. He has approximated the nonlinear integral equation by using a first-order linear expansion and has shown that the Fredholm kernel (given in Equation 11 as $\sigma_{p_{\perp}}(\theta)$ and $\sigma_{p_{\parallel}}(\theta)$) varies more than Curry (Ref. 26) has determined. Young attributes this difference to his not making the assumption of holding the denominator, then numerator, constant in successive recursions as Curry does. The impact of this analysis on the AFRPL scattering experiment is to shed uncertainty on the original particle size retrieval method of choice--the MIESTEP/SIZIM family of codes.

In his analysis, Young ran uncalibrated relative intensity synthetic data like that acquired in the AFRPL laser scattering set-up through his first-order linearized particle size inversion scheme to determine if a relative size distribution could be accurately retrieved. His results, shown in Figure 32, point to the fact that in this case, data from the laser scattering experiment yields size distribution information only for particles in the 0.3 to 0.5 μ m size range. This is very little information indeed. Moreover, the data used in this analysis was noiseless, so error propagation through the linear deconvolution algorithm was not taken into account.

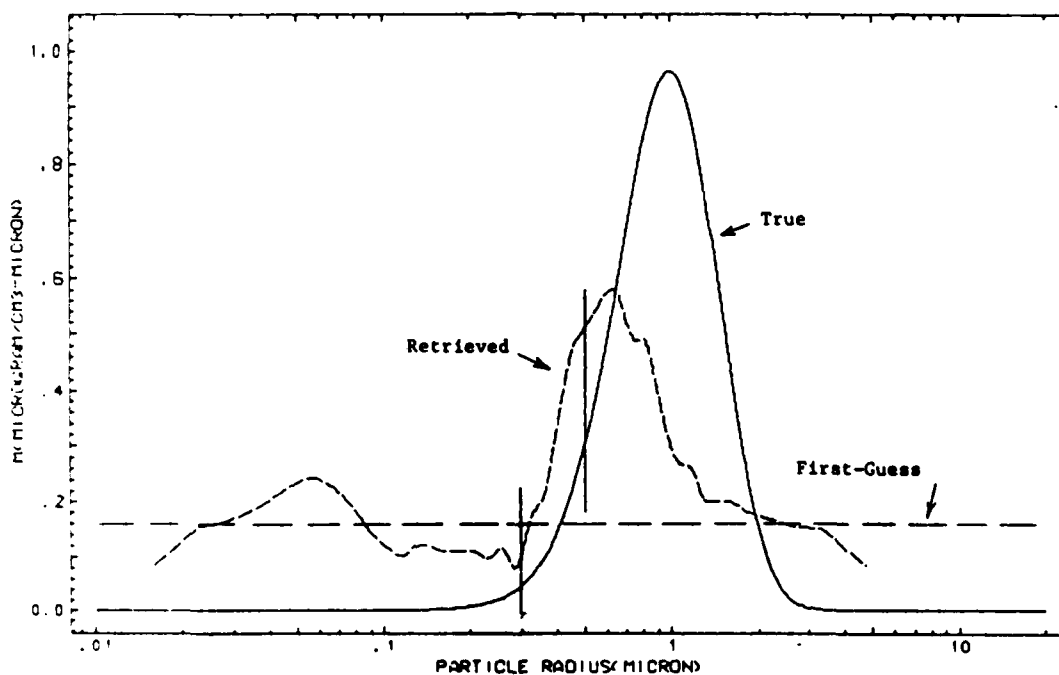


Figure 32. Size Distribution Retrieval Compared with Inputted Size Distribution from Young (Ref. 21)

The perfect noiseless data necessary for the aforementioned inversion was not supplied by the AFRPL experiment. Figure 33 depicts the low signal-to-noise ratio, showing very little difference in scattering detector pre- and post-ignition signal levels. Appendix C addresses the AFRPL efforts in enhancing scattering detector signals through an innovative adaptive noise cancellation scheme.

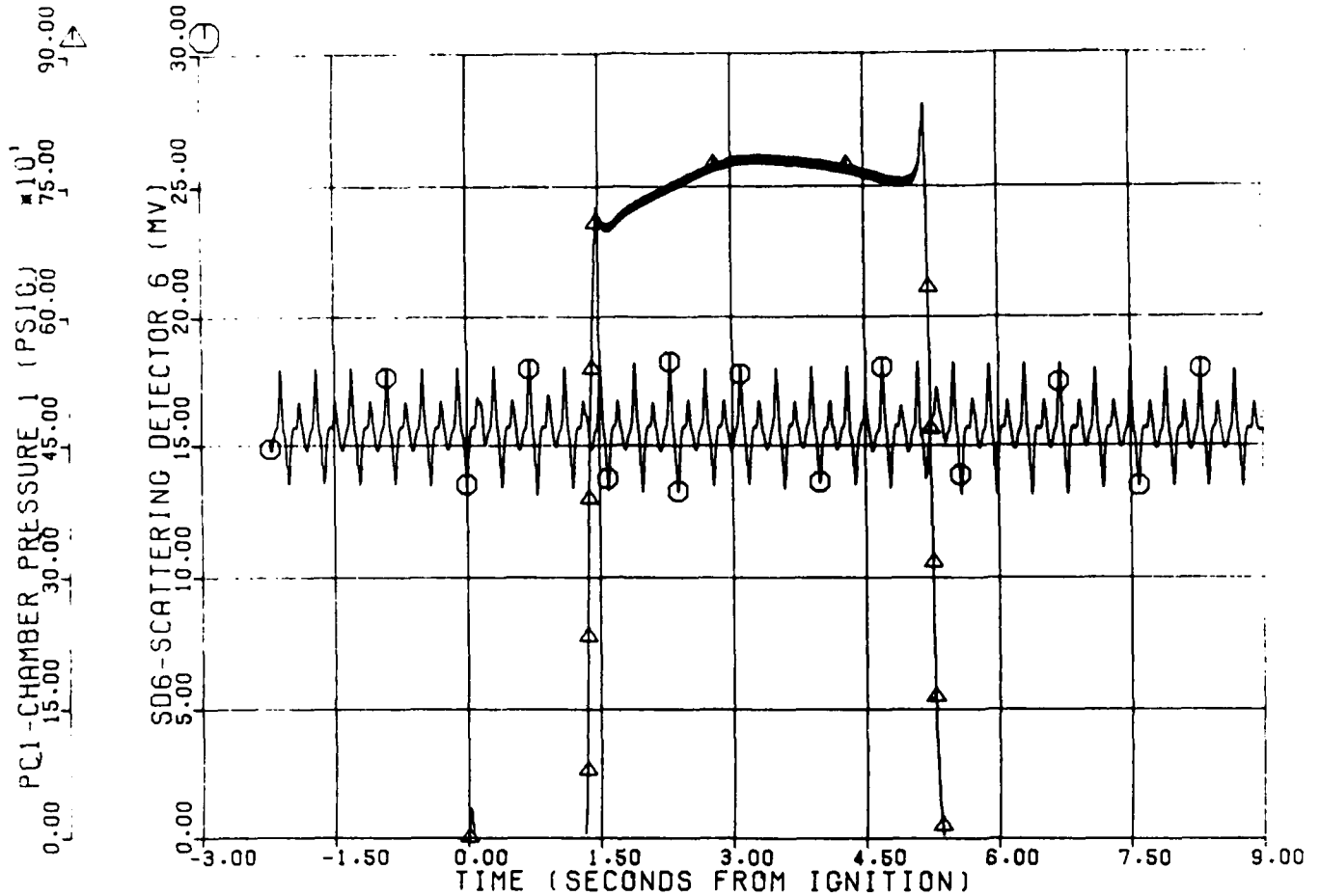


Figure 33. Scattering Detector vs Time Signal with a 15-lb
BATES Motor Chamber Pressure Trace

Given the debilitating uncertainty within the PSDF inversion scheme combined with the experimental uncertainties mainly from the low scattering detector signal-to-noise ratios (but also from unknowns in the calibration procedure and scattering focal volume determination), it was decided to use the laser scattering/transmissometer experiment to yield a volume-to-surface (or Sauter) mean particle diameter integrated over the laser line of sight through the plume (Refs. 29 and 30).

The single-color transmissometer algorithm described in these references has been codified into a mean particle size retrieval computer program, A32CODE (Ref. 31).

The basic retrieval method used in A32CODE recognizes the low mass loading conditions prevalent in the low-visibility propellant two-phase plume flows. These conditions make reasonable the application of single-scattering from homogeneous, spherical particle assumptions (discussed in Appendix A) and the application of Beer's Law toward describing laser light extinction:

$$\ln \tau = L \int_0^{\infty} \pi r^2 Q_{\text{ext}}(\lambda, r) n(r) dr \quad (12)$$

where

τ = transmittance;

L = laser path length;

r = particle radius;

Q_{ext} = extinction efficiency;

λ = laser wavelength; and

$n(r)$ = PSDF.

Salient concepts behind Q_{ext} and $n(r)$ are discussed in Appendix A.

In Young's methodology (Ref. 29), he defines the mean extinction efficiency $Q_{\text{ext}}(\lambda)$ as being a weighted mean value:

$$\overline{Q_{\text{ext}}(\lambda)} = \frac{\int_0^{\infty} r^2 Q_{\text{ext}}(\lambda, r) n(r) dr}{\int_0^{\infty} r^2 n(r) dr} \quad (13)$$

The total mass loading C_m is the integrated product of the characteristic bulk density of the particulate material (ρ_p), the volume of the particle and the number of particles is expressed as

$$C_m = \int_0^{\infty} (\rho_p 4\pi/3 r^3) n(r) dr. \quad (14)$$

Finally, the volume-to-surface mean particle radius is defined as:

$$r_{32} = \frac{r^3 n(r) dr}{r^2 n(r) dr} \quad (15)$$

which is simply,

$$r_{32} = \bar{r}^3 / \bar{r}^2 \quad (16)$$

Substituting Equations 13-16 into the Beer's Law expression, Equation 12, yields

$$-\ln \tau = \frac{3L}{4\rho_p} C_m \frac{\bar{Q}_{ext}(\lambda)}{r_{32}^3} \quad (17)$$

or

$$r_{32} = \frac{-3LC_m \bar{Q}_{ext}(\lambda)}{4\rho_p \ln \tau} \quad (18)$$

Young's technique essentially calls for calculation of the mean extinction efficiency $\bar{Q}_{ext}(\lambda)$ from Mie theory principles and the solution of Equation 18 given prior knowledge of the other terms in the expression.

Hence, A32CODE has as its input parameters (Ref. 32): (1) plume diameter L at laser transmissometer station (cm); (2) particulate mass loading (g/cm^3); (3) particulate material bulk density, ρ_p (g/cm^3); and (4) laser transmittance through the plume. Additional inputs include real and imaginary components of the particulate index of refraction, laser wavelength and choice of unimodal or bimodal rectangular size distributions. Uncertainties in measurement are imbedded in error base input options for Parameters 1-4, and lack of knowledge of indices of refraction can also be specified in the code inputs. The final output, mean particle radius r_{32} , reflects the input error budgets.

It should be cautioned again that the Beer's law assumptions in the physics behind the code--a low concentration plume, a homogeneous plume media

(with an index of refraction $n=1-0k$) and the interaction mechanisms consisting of absorption and scattering--limit the applicability of the code to the low-visibility type propellants used in this study. Furthermore, the single scattering by homogeneous, solid spherical particles implied by using a mean extinction efficiency $\bar{Q}_{ext}(\lambda)$ introduces enough uncertainty that results must be couched in terms of effective mean volume-to-surface particle radius over the laser line of sight. These objections aside, the just described analytic procedure is sound and helps provide AFRPL with its first substantive in-situ particle sizing capability, from measurement to final data reduction.

3.2.2 Transmissometer Results and Interpretation - Considerable difficulty was experienced in taking suitable BATES motor laser transmission data. With solid Al or ZrC additive loadings approaching 5% by weight, laser transmissivity was virtually zero, rendering this type of data unusable. Since a significant number of AFRPL BATES firings are not the solid loaded low smoke type, many targets of opportunity were necessarily bypassed. Also, the laser transmissometer configuration described in Section 2.3 worked only for 15-lb BATES motors. Actions taken in 1984 to make the transmissometer axially adjustable for 30- and 70-lb BATES motors were effected late enough to not affect any solid additive loaded plume measurements reported here. As a consequence, of the 29 firings listed earlier in Table 5 (Section 3.1.2) with usable laser transmission data, only five had Al or ZrC additives; the other 24 had no solid propellant ingredients. Table 6 summarizes the particulate sizes derived from the A32CODE described in the previous section.

In reducing the data, input error bounds were estimated. Transmissivity standard deviations served as the error bands for those measurements. Additionally, particulate mass loadings were determined by elemental molecular weights and gas and particulate matter exhaust densities were calculated from an AFRPL theoretical one-dimensional isentropic equilibrium program (Ref. 32). A $\pm 10\%$ error range was assigned to this computation and to specific gravities for pure form Al_2O_3 and ZrO_2 . Indices of refraction ranging between $(1.7-1.8)n + i(0-0.02)k$ were assigned to the particles. Finally, the length of the laser path through the plume was determined to be 9.75 ± 0.65 cm.

Table 6. Particulate Size from Transmissometer Experiment

AFRPL MOTOR IDENTIFICATION	PROPELLANT PARTICLE LOADING	EXHAUST PARTICULATE PRODUCT	COMPUTED D_{32} (μm) OF EXHAUST PARTICLES
144B-008	0.50% Al	Al_2O_3	0.700 ± 0.106 (+15.1%)
179B-001	0.50% ZrC	ZrO_2	0.744 ± 0.139 (+18.8%)
179B-004	0.50% ZrC	ZrO_2	2.08 ± 0.56 (+ 27.1%)
194B-001	1.0% ZrC	ZrO_2	$1.63 \pm .084$ (+ 51.7%)
194B-002	1.0% ZrC	ZrO_2	0.922 ± 0.134 (+29.0%)

It must be remembered that these particle size measurements were taken from a thus far unverified laser transmissometer technique. Implicit in this caveat are the assumptions, both analytical and physical, described in Section 3.1 and Appendix A. Although we are confident of the size retrieval methodology, another corresponding measurement or absolute system calibration has yet to be adequately done.

The small sample size of five coupled with three different values for the propellant particle loading variable make any trend analysis of the derived particle size difficult and highly speculative

Table 7 lists the comparison between the transmissometer measurement-derived mean particle diameter and the semi-empirical correlation diameter calculated from Equation 16. The above listed mass-volume diameter D_{43} was chosen by Nickerson (Ref. 24) instead of the volume-surface diameter D_{32} because it serves to better predict two-phase flow losses, but the difference should not be as pronounced as shown above. The D_{32} values exceed the D_{43} diameters by several factors in each of the three firings. The question of which figure is better representative of the true rocket exhaust particle size cannot yet be inarguably answered. Given this limited information no attempt was made to correlate the computer mean particle size with motor geometry or performance parameters. Nickerson derived such an empirical relationship used in the above tabulation with 66 particulate samples captured in the farfield from a variety of solid rocket motor exhaust flows; this curve-fit is embedded in the two-dimensional/two-phase Solid Performance Program (SPP) used to

Table 7. D_{32} (from Transmittance) and D_{43} (from Nickerson) Comparison

AFRPL MOTOR IDENTIFICATION	EXHAUST PARTICULATE PRODUCT	\overline{D}_{32} (μm) (TRANSMISSOMETER)	\overline{D}_{43} (μm) (CORRELATION)
144B-008	Al_2O_3	0.700	0.293
179B-001	ZrO_2	0.744	0.222
179B-004	ZrO_2	2.08	0.0988
194B-001	ZrO_2	1.63	0.280
194B-002	ZrO_2	0.922	0.276

to predict motor performance and an input to JANNAF flowfield and radiation prediction computer codes. Nickerson's relation is:

$$D_{43} = 3.6304 D_t^{0.2932} (1 - e^{-0.0008163 \xi_c P_c \tau}) \quad (16)$$

where

D_{43} = mass-weighted average diameter (μm);

D_t = nozzle throat diameter (in);

ξ_c = Al_2O_3 or ZrO_2 concentration in chamber (g-mol/100 g);

P_c = average chamber pressure (psia); and

τ = average chamber residence time (ms).

Particle capturing techniques used in establishing data points to derive Equation 16 suffer from the same deficiencies enumerated in Section 2.3 (and in fact, may suffer from even more biases because some particles were gathered from petri dishes lying exposed in the plume flow). The accurate specific impulse predictions of SPP point to the semi-empirical model's authenticity but only toward measuring specific impulse. More data points must be acquired to truly verify Equation 16. Even this, however, is no substitute for the necessary step of taking an accurate calibration or parallel measurement to

gain confidence in the laser transmissometer experiment's mean particle diameter results.

3.2.3 Particle Collection Probe Technique Data Reduction Methods - The subsonic particle collection probe described in Section 2.3.2 captured particulate samples for AFRPL in-house analysis. At the time of this writing, the AFRPL image analysis capability could not give a size distribution count over the full extent of the expected size range. This is unfortunate because correlating mean sizes with the A32CODE effective mean size determination of the previous section would enhance confidence in the laser transmissometer measuring technique's results. The data would be useful despite biases introduced by dust entrainment, agglomeration and bow shock effects. To overcome these error sources, a sharp-edged supersonic particle probe as described in Section 2.3.2 is currently in fabrication and will be applied at AFRPL in the future along with an upgraded image analyzer.

The possible deposition of carbon, aluminum chloride or other surface contaminants on the particles was not analyzed via any x-ray electron probe technique, as AFRPL does not presently possess the capability.

3.2.4 Particle Collection Probe Technique Results and Interpretation - Photomicrographs of captured rocket exhaust particles indicate that a few may be hollow (Fig. 33). Dawbarn and Kinslow (Ref. 33) noted the same phenomenon in their work and have summarized several suspected mechanisms. Alumina has been postulated to form a stable molten core of aluminum on the surface, expanding by pressure from aluminum vapor; this appears to be unlikely due to the severe aerodynamic forces interacting with particulates within the exhaust plume flowfield. A more likely explanation is that the Al_2O_3 inflation occurs from gases, H_2 or CO_2 , within the plume. These inflated Al_2O_3 particles could be nonstoichiometric α -phase alumina not reacting with these gases. Nonetheless, inherent in all these suggestions is that hollow spheres arise from aluminum burning outside the combustion chamber, therefore accounting for but a fraction of the total amount of alumina captured. This seems reasonable--hot particle streaks in solid rocket motor plumes is a well-observed phenomena at AFRPL and elsewhere.

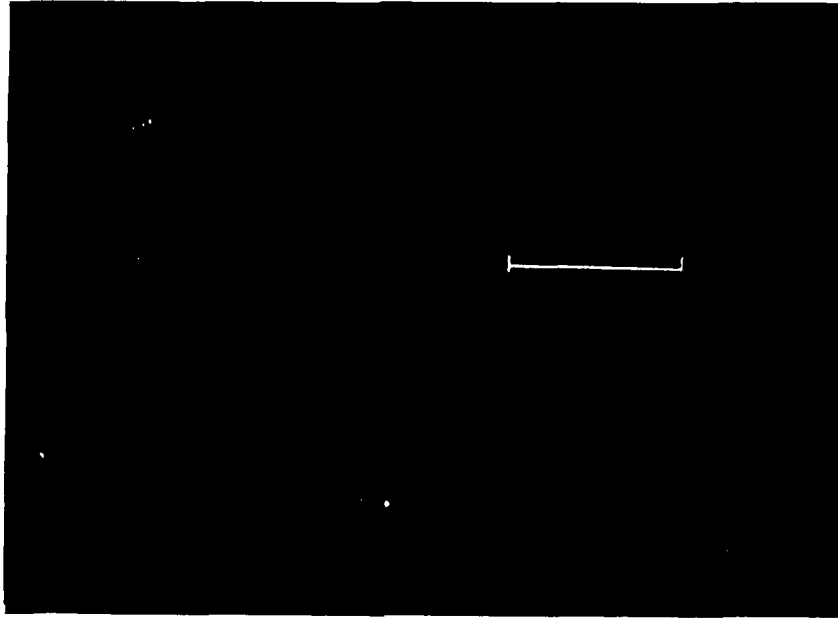


Figure 34. SEM Photomicrograph of Two Captured 10- μ m Al_2O_3 Spheres.

Note that the one on the right appears to be hollow.

Reference 34 cites high ambient humidity (greater than 80%) as a strongly contributory factor in the formation of hollow Al_2O_3 spheres, since they observe that aluminum spheres burn better--and hence more hollow spheres are produced--in a wet atmosphere. The AFRPL findings dispute this. All data reported here were taken at relative humidity levels usually well below 30%. Also the high H_2O content of a rocket plume logically disputes the empirical high relative humidity-hollow particle correlation; the effective and already high humidity within the plume should be relatively independent of the external environment.

Ramifications of hollow particles with a cavity opening such as shown in Figure 34 are substantial. The effective emissivity of an aggregation of Al_2O_3 particles with this characteristic would be much higher than pure form Al_2O_3 , as the cavity could emit blackbody radiation. The hole also makes the particles obviously nonspherical, and Mie theory mechanisms

described in Appendix A might not adequately explain plume scattering. Electromagnetic radiation may be absorbed into the cavity, then reradiated thermally; also, it may be reflected several times within the cavity, exiting at different angles than postulated by scattering theory. Additionally, mass conservation assumptions in flowfield and radiation prediction computations (i. e., differences in predicted particle sizes between hollow and solid spheres) makes the presence of hollow spheres a significant phenomenon. Assumptions regarding the particle density impact not only on results from radiation predictions but also on the A32 code reported earlier in this section. Strand (Ref. 34) reports densities of hollow Al₂O₃ rocket exhaust particles which vary from 1.5 to 3.5 g/cm², differing substantially from the 3.7 g/cm² value used in A32 code to determine the mean particulate size.

3.3 Plume Temperatures and Particle Pressures

3.3.1 IR-E/A Technique Data Reduction Methods - As described in Section 2.4 of this report, an IR-E/A fixed line-of-sight multispectral measurement technique was used during these firings. The spectral emission/absorption scan data was to be deconvolved to temperature and partial pressure profiles through an iterative Abel inversion algorithm developed by Young (Ref. 35).

Young's methodology can be illustrated by the gas-only radiance L^P and transmittance τ^P relations developed in Appendix B. These relations can be expressed as:

$$L_{\lambda}^P(\lambda, T^P) = \int_0^{\infty} (L_{\lambda}^{BB}(s) + L_{\lambda}^E(s)) \frac{d\tau^P(s)}{ds} ds \quad (17)$$

where

λ = wavelength;

T^P = plume temperature;

s = line of sight;

l = distance along s ;

$L_{\lambda}^{BB}(s)$ = monochromatic blackbody radiance at s ;

$L_{\lambda}^E(s)$ = monochromatic external radiance incident on the plume boundary; and

$\overline{\tau_{\lambda}^P}(s)$ = average monochromatic transmittance of the plume along s .

Also,
$$\ln \tau^P(s) = - \int_0^s c^P(s) p^P(s) K^P(s) y^P(s) ds, \quad (18)$$

where

$c^P(s)$ = concentration at s ;

$p^P(s)$ = pressure at s ;

$K^P(s)$ = monochromatic absorption coefficient at s ; and

$y^P(s)$ = monochromatic band model function at s .

Young's algorithm solves Equation 18 for $p^P(s)$ given a known concentration profile $c^P(s)$ and can henceforth also be used, as indicated in Appendix B, to retrieve temperature profiles. The Abel inversion scheme described in Reference 35 essentially uses the $-d \tau^P(s)/ds$ term in Equation 16 as the weighting function in the inversion procedure. Note that τ^P is written as a function of both wavelength λ and position s along the plume line of sight.

Young (Ref. 35) calculates the near infrared bandpasses at which the major plume constituents H_2O , CO_2 and CO radiate without overlap at the elevated temperatures and pressures expected with BATES motors as:

- (1) H_2O : 2.3-2.64 μm
3.1-3.5 μm
6.0-6.9 μm

- (2) CO_2 : 4.14-4.23 μm

(3) CO: 5.0-5.3 μm .

These define the spectral regions under which an IR-E/A inversion can be accomplished, with single plume species radiators and therefore enough of a pure $-\frac{d\tau_{\lambda}^P(s)}{ds}$ weighting function variation along λ to justify a multispectral experimental technique.

Young also models a radial temperature profile along s with the plume centerline peak temperature at 1500K and declining monotonically to 750K at a 10-cm radius. He also provides synthetic IR-E/A radiance data for 6.3 μm H₂O, 4.3 μm CO₂. Despite this reasonable BATES temperature profile and radiance model, the ensuing weighting function $-\frac{d\tau^P(s)}{ds}$ does not vary enough to extract accurate temperature or concentration profiles, as illustrated in Figures 35 and 36. There is a $\pm 30\%$ error bound even in this best case. The less stressing nonscanning monochromatic case was then analyzed, and a similar

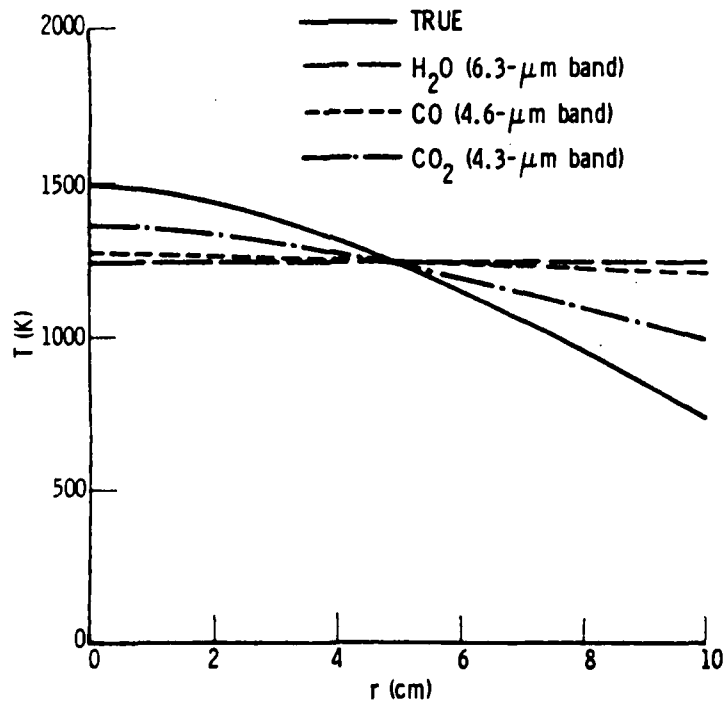


Figure 35. Temperature Inversion Results from Young's BATES Plume Model (Ref. 25)

lack of $-\overline{d\tau^P(s)}/ds$ resolution leads to only slightly better inversion accuracies. These poor inversion results occurred even with noise-free synthetic data. The plume analyzed here was particle-free and represents a simpler model than one with particle emission and absorption effects.

The conclusion, which was reached midway through the AFRPL experimental efforts, was that a multispectral IR-E/A temperature and partial pressure plume profile could not be accurately retrieved with solid rocket motors. The alternatives to pursue were essentially two: convert the IR/E-A apparatus to multiple in-band and spatially scanning emission and absorption measuring detectors similar to that applied at AEDC (Ref. 36) or abandon the AFRPL IR-E/A efforts.

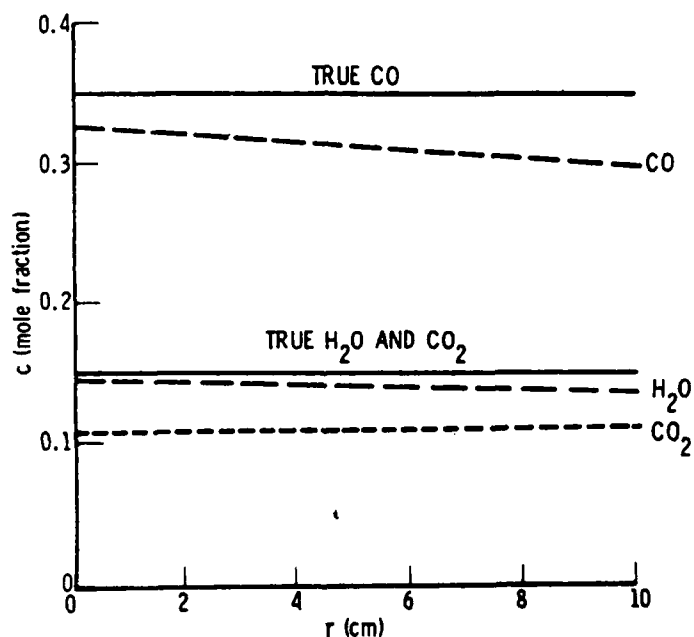


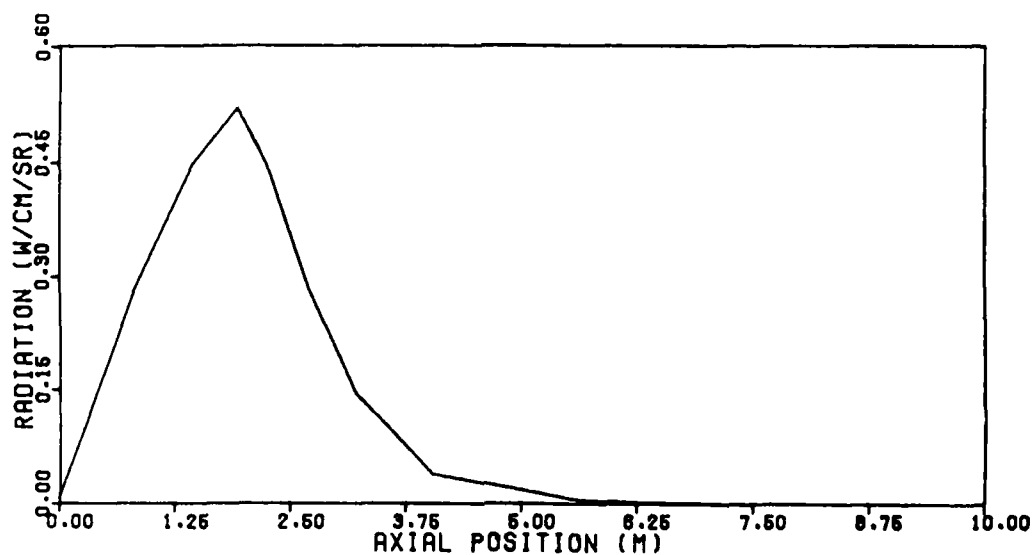
Figure 36. Concentration Inversion Results from Young's BATES Plume Model (Ref. 26).

AFRPL chose to pursue the analytic portion of a gas/particle temperature and concentration profile retrieval method despite probable new instrumentation requirements. The analysis (Ref. 37) and computer code (Ref. 38) centered around a spatially scanning IR-E/A measurement scheme. The AFRPL experimental apparatus, however, remained the same due to cost and space constraints. The AFRPL scanning monochromator was locked at the 2.7- μ m p

branch H₂O band and used as a narrow bandpass radiometer to gauge the water-band intensity variation through the BATES firing.

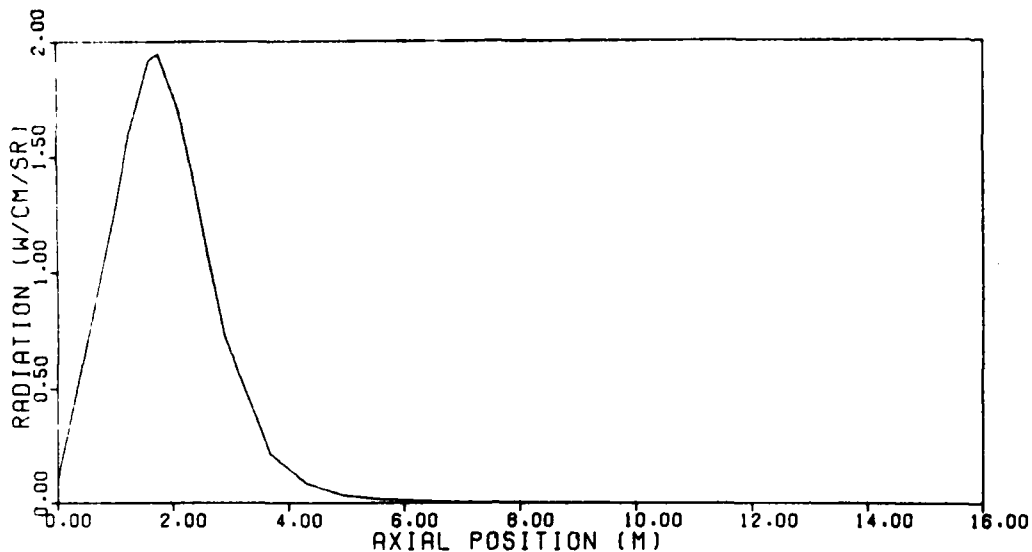
3.3.2 IR-E/A Technique Results and Interpretation - Because the IR-E/A technique could not be used as originally expected to yield plume temperatures and partial pressures, no data of this type can be presented. However, some infrared emission data in the 2.7- μ m H₂O band was taken by the blackbody source/chopper/lock-in amplifier arrangement described in Section 2.4.1.

There was difficulty in assigning system calibration factors to the monochromator's voltage output because of inconsistent wavelength and response calibration techniques. Hence, a quantitative firing-by-firing comparison is not possible, especially when considering that the plume station radiation depends on variable motor ballistic and geometry parameters. The predictions of Figure 37 illustrate how a 2.4-2.7 μ m bandpass station radiation can vary with changes in chamber pressure, thrust and nozzle geometry. The propellant and other motor parameters remain unchanged.



- a. Chamber Pressure: 170 psi; Thrust: 1200 lbf; Nozzle Throat Diameter: 0.920 in; Nozzle Exit Diameter: 2.593 in.

Figure 37. In-Band (2.4-2.7 μ m) Radiation Axial Profiles for 15-lb BATES Motor Plumes with Identical Propellants



- b. Chamber Pressure: 590 psi; Thrust: 1000 lbf; Nozzle Throat Diameter: 10.78 in; Nozzle Exit Diameter: 2.325 in.

Figure 37. In-Band (2.4-2.7 μ m) Radiation Axial Profiles for 15-lb BATES Motor Plumes with Identical Propellants

In light of this only a qualitative assessment of the 30 firing cases with IR emission data can be done. Figure 38 depicts the typical plume emission data at the water band taken as a function of time. The chamber pressure curve is also shown for reference. Note that at ignition the radiance level pulses sharply, as it does near the firing termination. This can be attributed to the BKNO_3 ignition pellets and initial flash at ignition and the characteristic high pressure bump near burnout. All the data show these attributes.

Because of its uncalibrated form, not much significance can be attached to this data beyond the presence of the aforementioned radiance spikes. Note the lengthy H_2O -band steady state radiance. This indicates, albeit after the fact, that a stringent time resolution requirement is not required in a spectral scan if one assumes the same steady state conditions exist in other bands of interest. This fact is used in planning the scanning rate of future AFRPL spectroradiometric efforts.

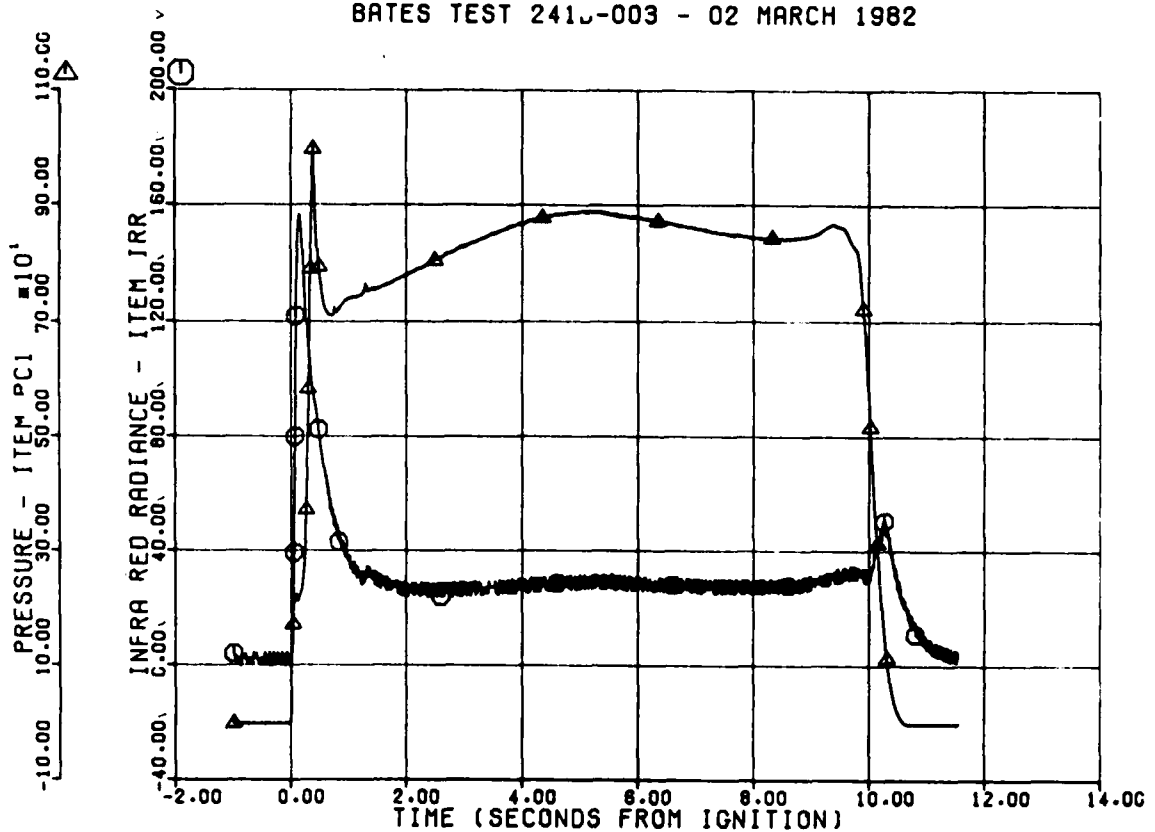


Figure 38. Typical 15-1b BATES Motor Water Band IR Emission Trace

3.4 Plume UV Signatures

3.4.1 Data Reduction Methods - The fundamentals of plume UV emission are not well known. With many composite solid rocket motor propellants, the gas phase chemistry is not wholly characterized or understood. There is not much data in support of chemical modeling efforts although some spectroscopic laboratory measurements are underway (Ref. 17). Because of these major uncertainties in identifying UV radiation mechanisms for solid rocket propellant plumes and without the immediate prospect of a supporting model to base measurements on, 2750-4250 Å emission spectra at the plume centerline and near the motor exit plane were recorded for possible use in a data base. Subsequent scans were displayed simultaneously to show temporal spectral behavior.

Reactive radical plume species expected to be present in this spectral region included OH, CN, NH, CH, NO and CO. Some stability additives were also

expected to possibly contribute. It was also hoped a time history of plume species would provide useful information. Accurate detection of the species present within the plumes is highly dependent on the spectral resolution and sensitivity of the measuring instrument, and as will be illustrated, these were constraining aspects of the AFRPL UV measurements.

Section 2.4.1 describes how potentiometer output signals proportional to the wavelength position of the UV monochromator grating drive were curve-fitted via the linear regression-derived relation of Equation 15. The photomultiplier voltage response to the throughputted UV signal was then plotted as a function of the wavelength for each scan direction. Computer software was created to plot successive scan directions as a function of wavelength, yielding time contours of the UV signature. The uncertainty of the wavelength calibration, although different for each firing, is about 15 Å. The 50 Å spectral resolution of the monochromator was the limiting precision for wavelength.

As with the IR-E/A measurements reported in Section 3.3, the lack of an accurate absolute intensity calibration (due to poor documentation and uncharacterized window and lens spectral transmittances) prevents disclosure of radiation units; rather, intensity heights are displayed in their uncalibrated voltage units. This leads to a qualitative interpretation only of the magnitude of the UV radiation detected.

3.4.2 UV Results and Interpretation - There were twenty-six 15-lb BATES firings with successfully recorded UV scans between 2750 and 4100 Å. Three reduced smoke composite propellant series were evaluated: KKN (AFRPL 240B series), CWB (AFRPL 241B series) and DWP (AFRPL 242B series). The propellant compositions are shown in Table 2 (Section 2.2)

Representative UV spectra from each of these series are shown in Figure 39. There is similarity between individual UV signatures within each series, but there are significant differences between the propellant series UV spectra, as illustrated in Figure 40.

Because of the variation of several ingredient loadings between the

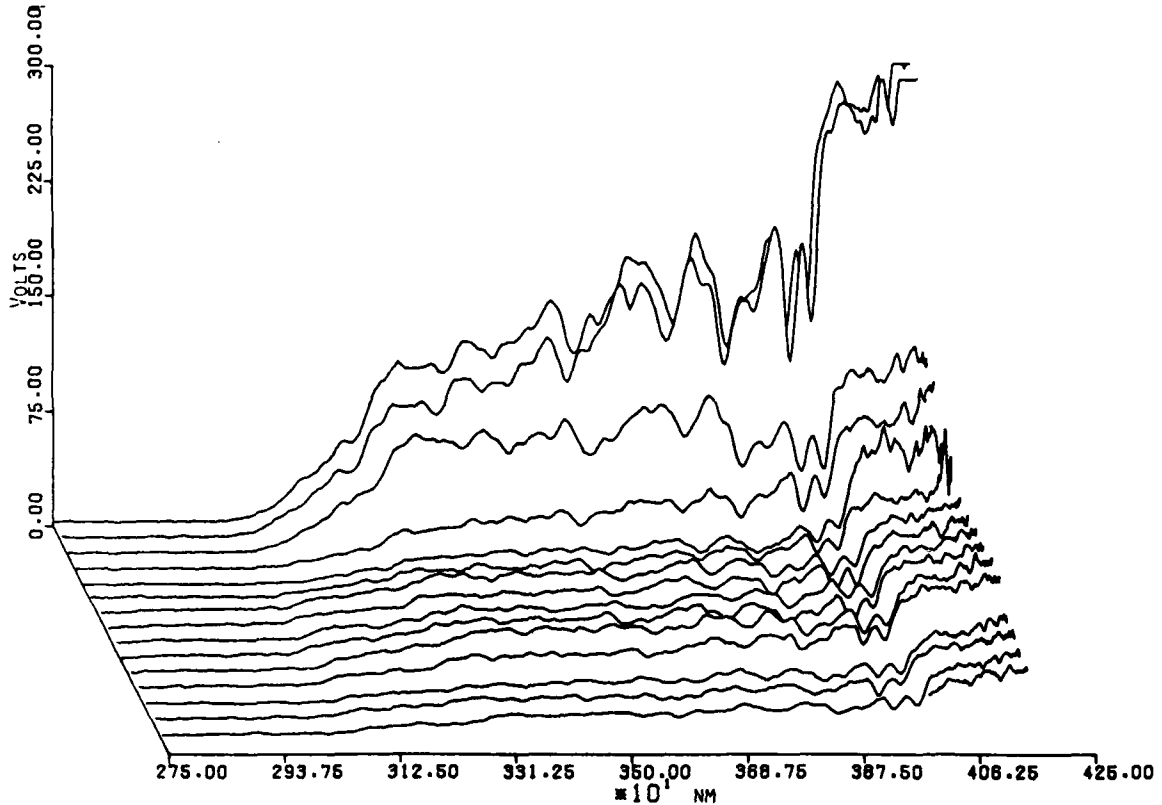


Figure 39. Voltage Response vs Wavelength for 16 Mid-Firing Half-Scans for KKN Propellant (Firing 240B-004)

three propellants, it is difficult to assert a quantitative cause for the signature differences, but some general observations can be made. First and most obviously, the time variation of relative UV signatures can be gauged from Figures 39-41. The integrated scan signatures can be seen to change slightly through the firings. Some changes during the steady state firing are to be expected because of spurious noise signals mainly due to small plume radiance fluctuations. As shown in the UV spectra, most of the scan-to-scan variations are minor and can be ascribed to these fluctuations. The only significant change between half-scan signals is shown in Figure 39. This sudden post-steady state intensity growth was seen to occur periodically in all the three propellant series. A UV signal "burst" occasionally appears

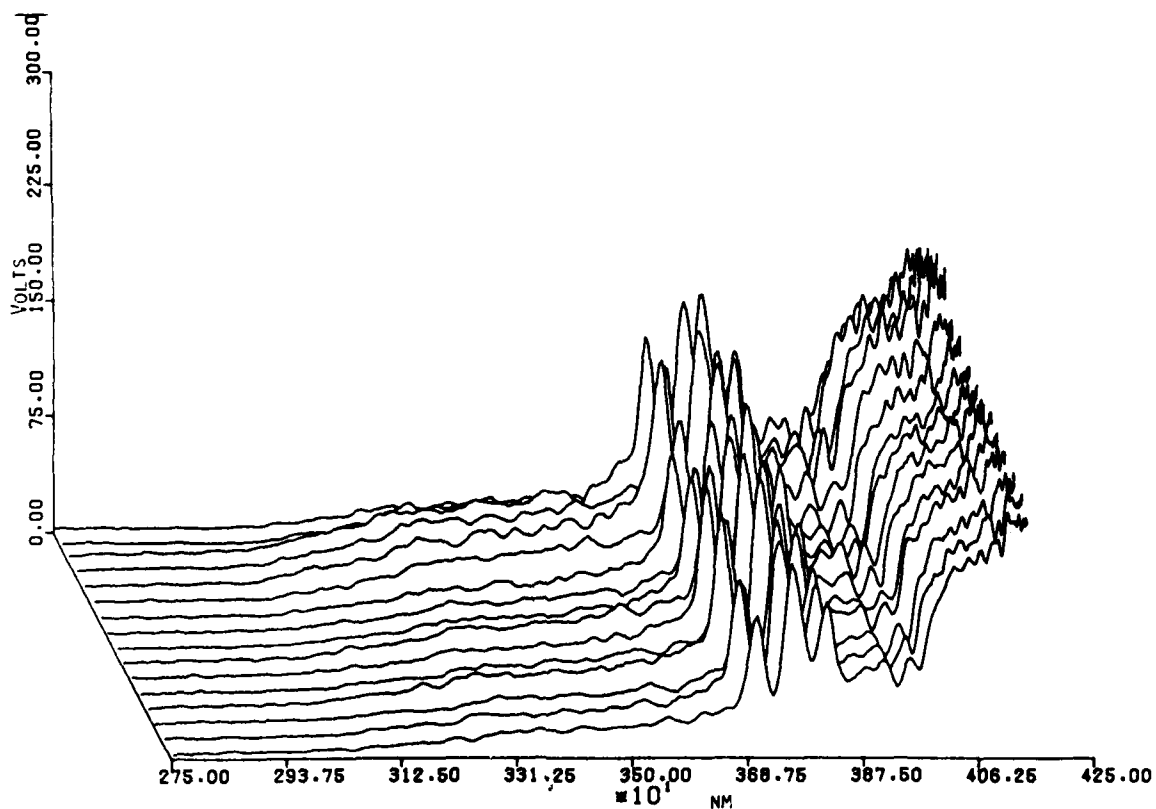


Figure 40. Voltage Response vs Wavelength for 16 Mid-Firing Half-Scans for CWB Propellant (Firing 241B-004)

near the end of the burn time. It is difficult to explain this transient behavior; it may arise because of an uneven mass flux of UV radiating species. Notice this is a continuum effect. Similar intensity versus time fluctuations have been recorded before (Ref. 20).

Figure 42 makes especially evident the presence of some type of continuum radiation. In this figure there is a general gradual increase in the response of the detector with increasing wavelength. Atop this pedestal are signal fluctuations characterizing the molecular band structure of plume specie. This continuum base has been subject to previous analysis (Ref. 21). Two mechanisms for its appearance have been postulated: thermal greybody emission from hot alumina particulates and chemiluminescence, primarily from the $\text{CO} + \text{O}$ reaction, from plume afterburning. The relative contributions

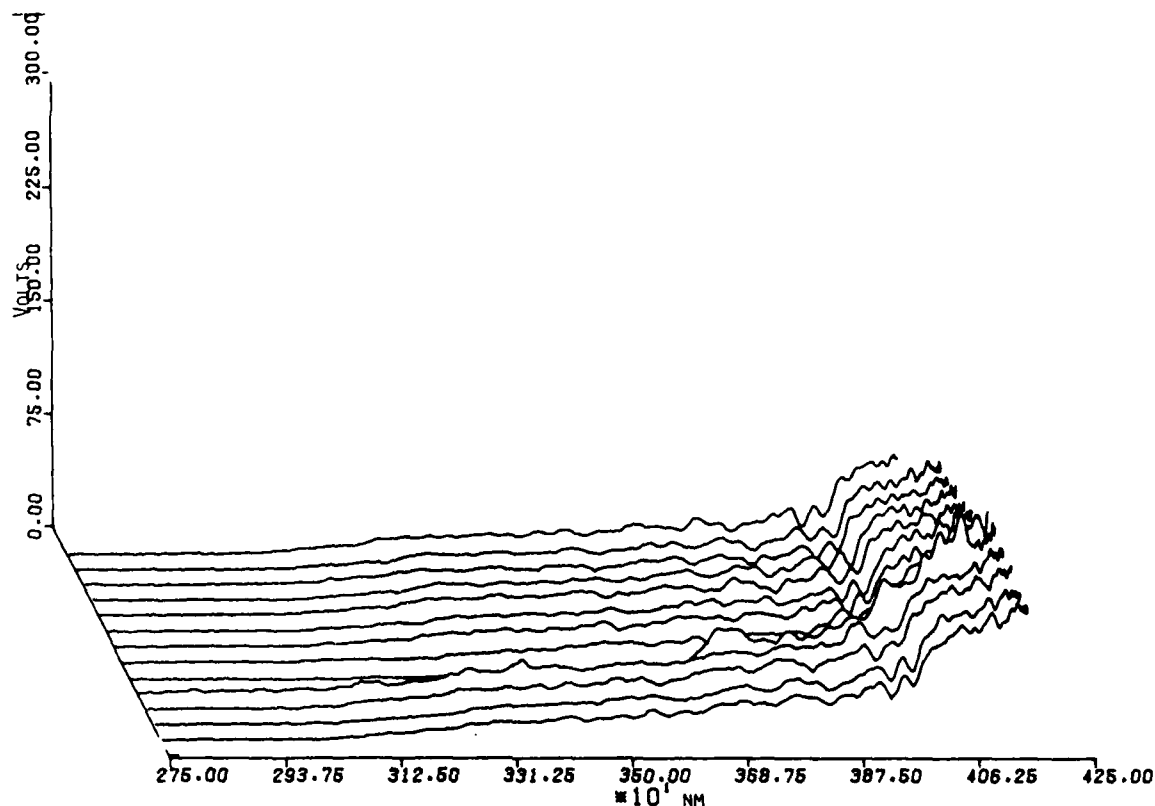


Figure 41. Voltage Response vs Wavelength for 16 Mid-Firing Half-Scans for DWP Propellant (Firing 242B-004)

from these phenomena is uncertain, but it appears that both are of some importance in explaining the observed rocket plume UV emission.

The interesting difference the data presented in this report poses is that none of the three propellant formulations shown in Figures 39-42, KKN, CWB and DWP had particulate additives; this is shown in Table 2 (Section 2.2). It is suspected then that the observed continuum behavior arose mainly from CO + O chemiluminescence rather than thermal emission. It is unfortunate that the UV monochromator was not completely and reliably calibrated, as the extent of the apparent chemiluminescence would be of interest. There is a caution to the chemiluminescence assumption, however: although the UV monochromator's FOV was carefully aligned to exclude the motor nozzle, thermal emission emanating from this source could be a contributory, albeit doubtful, continuum

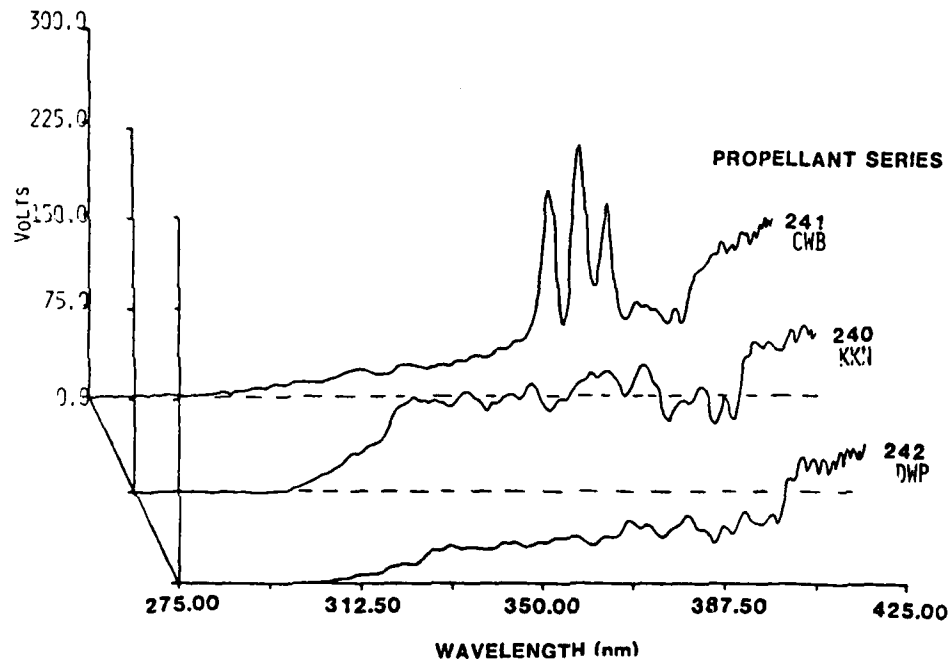


Figure 42. Single Half-Scan Comparisons of Representative Voltage Responses vs Wavelengths for Three Reduced Smoke Propellants

radiation factor. Other radiation sources may be unaccounted particles within the propellant formulation, out-of-field scattering and carbon ablation from the nozzle.

Neither the expected (1,0), (2,1) and (0,0) OH vibrational bands at about 2830, 2890 and 3060 \AA nor the several less than 3000 \AA NO γ bands were found in the data taken with these BATES firings. A similarly poor matchup was found in the UV data analysis contained in Reference 32, although OH and NO band structures were reported with high resolution on composite propellant strands in a laboratory environment (Ref. 21). One reason for the poor AFRPL field measurement results was that the sensitivity of the UV instrument is relatively low at the correspondingly low UV signatures of these wavelengths. The above mentioned laboratory results show that these species radiate in these regions.

There appears to be a 3360 \AA NH emission peak, especially in the

latter scans of a KKN propellant firing (Fig. 39). The other apparent species present are violet CN bands which extend from approximately 3500 to 4600 Å. The scan resolution is unfortunately not fine enough to discern individual CN line features as the 3850, 3871 and 3883 Å triplet, nor is it fine enough to distinguish CN emission from an Fe molecular band at 3860 Å. Pb and PbO molecular line features characteristically dominate the spectra from about 4060 and 4270 Å, and this is apparently true with the cases presented by these three propellants. As there is no other explanation, we must assume trace elements of Pb or PbO from the motor case are in the reduced smoke AP propellant plumes tested. One final note: there is an unidentified spectral triplet feature centered at about 3760 Å which is easily discerned with the CWB propellant of Figure 40. In the absence of any other information, we must assume this is Fe; that is, in addition to Pb or PbO, trace elements of Fe are also found within the exhaust plume measured.

4.0 CONCLUSION

4.1 Summary and Discussion

In summary, the experimental apparatus described herein was applied to four specific plume measurement areas: visibility figure of merit, particle sizes, temperatures and partial pressures and UV signatures. In each of these areas, successful measurement is primarily contingent on instrumentation, retrieval algorithms and physical assumptions.

The plume visibility figure of merit criterion used in this study, laser transmissivity, is but one possible description. Drawbacks such as the presence of obscuring ignition smoke, and the monochromaticity of the measurement were enumerated. The major drawback is the lack of correlating data between the attenuation measurement and total plume detectability. Nonetheless, applying the transmissivity figure of merit to a series of reduced smoke propellant plumes indicates a difference between different formulation exhausts. By this criterion, a relative ranking of signatures can be made. It must be cautioned, however, that further work must be done in making different figure of merit measurements and positively relating any figure of merit measurements to total plume detectivity. Larger sample sizes

should also be acquired, both to assure statistical confidence intervals and derive further figures of merit.

AFRPL particle size measurements are dependent on a number of physical assumptions and are subject to difficult numerical data retrieval methods. The technique finally decided on in this work yields an effective volume-to-surface mean particle diameter from the laser transmissometer experiment. Results thus far generated come from a relatively small sample of solid rocket motor firings, so generating a conclusive relationship between the retrieved particle diameter and motor geometry or performance cannot yet be done. Comparing the results with a semi-empirical curve fit (based on earlier data on captured particles) of expected mean diameters shows the retrieved particle diameters are significantly larger, but again, more data must be taken before a modification to the curve fit can be considered. Further work must also be done to verify and calibrate the retrieved particle diameters and to generate an experiment and analytical technique to confidently deconvolve particle size distribution functions.

Recognized biases introduced by particle capturing techniques led to the design of the supersonic shock-swallowing particle collection probe described within the report. Of the collected particles, an interesting phenomena arises: apparently hollow particles embellished with a hole. Higher effective emissivities, particle nonsphericity and a larger number of particles for a constant mass loading are possible results of this.

Plume temperatures and partial pressure proved analytically impossible to derive from multispectral scan results due mainly to an insufficient emission/absorption path variation with wavelength in particle-loaded plumes. The scanning monochromator was then locked at the $2.7 \mu\text{m}$ H_2O p branch band to gauge the time trace of H_2O emission and absorption. It is clearly shown to follow the pressure trace, remaining practically invariant during the firing's steady state portion. This information was used in the time resolution specification of an AFRPL procurement of a later infrared signature measurement device, a Fourier Transform Spectrometer. Unfortunately, because of the uncertainty in calibration procedures, single-wavelength and line-of-

sight temperature and partial pressure retrieval could not be done from the emission-absorption measurement.

Plume UV emission spectroscopy was accomplished from 2750 to 4100 Å⁰ for three reduced smoke composite propellant series. The UV spectra time evolution was shown with single scan contours plotted along a time axis. An observed continuum effect was due more to chemiluminescence than thermal emission because exhaust particulates were not present, with the exception of carbon ablation from nozzle erosion. Several expected OH and NO bands are not present in the data; although NH and violet CN emission bands features were identified. Trace Pb or PbO and Fe elements were perceived to be present within the UV signature. Because UV modeling is still in its early developmental stages future and better-resolved UV spectra in similar field applications would yield data to supplement these results.

4.2 Future Work

The follow-on in-house effort is tailored more specifically after better characterizing the sensitive input files to various JANNAF signature prediction codes. The particle sizing effort will still be pursued by supplementing the laser transmissometer experiment with the supersonic shock swallowing quench probe described in Section 2.3. Analytical and experimental particle sizing methods will continue to be investigated to eventually retrieve ensemble particle size distributions within the plume flowfield. Of more driving concern, however, are other particle properties, specifically, the infrared optical properties of particle indices of refraction and emissivities. This dictated the supersonic inlet probe design.

AFRPL is in the process of acquiring more field instrumentation for code verification. Instruments include a high resolution infrared Fourier Transform Spectrometer, an ultraviolet-visible flat field spectrograph, plus a host of other infrared and ultraviolet radiometric and support devices. These instruments will be transported to different test stands aboard the just-renovated Mobile Radiometry Trailer (MRT). Appendix D describes plume measurements to be done on 15-lb BATES motors before these plans and MRT are implemented.

REFERENCES

1. Beckman, C. W., Evaluation of Air Launch Missile Propellants, AFRPL-TR-81-34, Air Force Rocket Propulsion Laboratory, Edwards Air Force Base, Calif., January 1982.
2. Nack, K. K., Beckman, C. W., and Weaver, D. P., "Plume Measurements of Test Motors," 1982 JANNAF Propulsion Meeting, CPIA Publication 370, Vol. IV, February 1983, pp. 535-543.
3. Nelson, H. F., "Scattering of Infrared Radiation in Rocket Exhaust Plumes," 13th JANNAF Plume Technology Meeting, CPIA Publication 357, Vol. 2, April 1982, pp. 201-210.
4. Nelson, H. F., "Effect of Radiation Scattering on IR Signatures of Low Altitude Rocket Plumes," 14th JANNAF Plume Technology Meeting, CPIA Publication 384, Vol. II, November 1983, pp. 41-51.
5. Lewis, J. W. L., Curry, B. P., and Weaver, D. P., Determination of the Size Distribution Function for Particles in a Hypersonic Flow Field, AEDC-TR-77-101, Arnold Engineering Development Center, Arnold Air Force Station, Tenn., July 1978.
6. Meserve, G. S., Upgrading of Laser Mie Scattering Measurement System, AFRPL-TM-82-07, Air Force Rocket Propulsion Laboratory, Edwards Air Force Base, Calif., July 1982.
7. Brower Engineering, Inc., Practical Calibration of Optical Spectrometers for Field Measurements, DNA-TR-3152T, Defense Nuclear Agency, Washington, D. C., January 1973.
8. Hoshizaki, H., et. al., Plume Visibility Detection Study, Volume 1: Technical Analysis, AFRPL-TR-78-32, Air Force Rocket Propulsion Laboratory, Edwards Air Force Base, Calif., November 1978.

REFERENCES (CONT'D)

9. Cramer, R. G., et. al., An Investigation of Experimental Techniques for Obtaining Particulate Behavior in Metallized Solid Propellant Combustion, AFRPL-TR-84-14, Air Force Rocket Propulsion Laboratory, Edwards Air Force Base, Calif., February 1984.
10. Beckman, C. W., Solid Propellant Impulse Scaling Prediction Techniques, AFRPL-TR-71-7, Air Force Rocket Propulsion Laboratory, Edwards Air Force Base, Calif., February 1971 (CONFIDENTIAL)
11. Stephen, W. A., Warren, T. C., and Scannel, P. R., Ballistic Missile Propellant Evaluation Test Motor System--Super BATES, AFRPL-TR-77-5, Air Force Rocket Propulsion Laboratory, Edwards Air Force Base, Calif., February 1977.
12. Meserve, G. S., Platinum Wire Particle Catcher, AFRPL-TM-82-08, Air Force Rocket Propulsion Laboratory, Edwards Air Force Base, Calif., July 1982.
13. Limbaugh, C. C., et. al., Nozzle Exit Plane Radiation Diagnostics Measurements of the Improved Transtage Liquid Rocket Injector Program, AEDC-TR-79-29, Arnold Engineering Development Center, Arnold Air Force Station, Tenn., March 1980.
14. McGregor, W. K., Assessment of the Infrared Emission/Absorption Method for Temperature and Species Partial Pressure Determination in Rocket Exhausts, AEDC-TR-79-61, Arnold Engineering Development Center, Arnold Air Force Station, Tenn., January 1981.
15. Wolfe, W. L., and Zissis, G. J., eds., "Radiation Theory," The Infrared Handbook, (U. S. Government Printing Office, Washington, D. C., 1978), Chapter 1.
16. Misener, J. A., Calibration of BATES Motor Firing Radiometric Measurements (Apr 84 - Oct 84), AFRPL-TM-84-34, Air Force Rocket Propulsion Laboratory, Edwards Air Force Base, Calif., September 1984.

REFERENCES (CONT'D)

17. Edwards, T., et. al., "Investigation of High Pressure Solid Propellant Combustion Chemistry," 15th JANNAF Combustion Meeting, CPIA Publication 412, Vol. 2, October 1984, pp. 163-171.
18. Slack, M., et. al., "UV Fundamental Property Measurements," 14th JANNAF Plume Technology Meeting, CPIA Publication 384, Vol. II, November 1983, pp. 253-262.
19. Bertrand, W. T., et. al., Radiation from the Plume of Multinozzle Rocket Engines Burning Gaseous Propellants at High Simulated Altitudes, AEDC-TR-76-113, Arnold Engineering Development Center, Arnold Air Force Station, Tenn., February 1977.
20. Wormhauadt, J., and Lyons, R., IR/UV Tactical Missile Plume Signature Data Analysis: Vol. I, AFRPL-TR-81-56, Air Force Rocket Propulsion Laboratory, Edwards Air Force Base, Calif., October 1981 (SECRET).
21. Hoshizaki, H., et. al., Plume Visibility Screening Study, Technical Analysis, AFRPL-TR-80-7, Air Force Rocket Propulsion Laboratory, Edwards Air Force Base, Calif., March 1980.
22. Lindquist, G. H., et. al., Air Launched Missile Plume Detection Study (U), AFRPL-TR-84-16, Air Force Rocket Propulsion Laboratory, Edwards Air Force Base, Calif., April 1984; (SECRET-NOFORN).
23. Chou, Y. S., Hoshizaki, H., and Heier, K. L., Plume Visibility Screening Study, AFRPL-TR-80-6, Air Force Rocket Propulsion Laboratory, Edwards Air Force Base, Calif., March 1980.
24. Nickerson, G. R., A Computer Program for the Prediction of Solid Propellant Rocket Motor Performance, AFRPL-TR-80-34, Air Force Rocket Propulsion Laboratory, Edwards Air Force Base, Calif., April 1981.

REFERENCES (CONT'D)

25. Beckman, C. W., Solid Propellant Impulse Scaling Prediction Techniques (U), AFRPL-TR-71-7, Air Force Rocket Propulsion Laboratory, Edwards Air Force Base, Calif., February 1971 (CONFIDENTIAL).
26. Curry, B. P., Weaver, D. P., and Lewis, J. W. L. Development of Mie Scattering Techniques for In-Situ Particle Diagnostics at AEDC, AEDC-TR-80-3, Arnold Engineering Development Center, Arnold Air Force Station, Tenn., November 1980, Appendix A.
27. Curry, B. P., User's Manual for Codes which Deconvolve Particle Size Distribution Using Angular Mie Scattering with Known Complex Refractive Index, In-House User's Manual, Arnold Engineering Development Center, Arnold Air Force Station, Tenn., 1980.
28. Curry, B. P., Voorhees, L. C., and Kiech, E. L., Development of Computer Codes to Invert the Particle Size Distribution Function of Homogeneous Spherical Aerosols from Mie Scattering Measurements, AEDC-TR-82-11, Arnold Engineering Development Center, Arnold Air Force Station, Tenn., November 1982.
29. Young, S. J., Considerations on the Retrieval of Plume Particle Properties from the AFRPL Transmissometer and Polarization-Scattering Experiments, AFRPL-TR-84-47, Air Force Rocket Propulsion Laboratory, Edwards Air Force Base, Calif., August 1984.
30. McGay, T. D., et. al., "Laser Mie Scattering Measurements of Particle Size in Solid Rocket Motor Exhausts," 12th JANNAF Plume Technology Meeting, CPIA Publication 332, Vol. II, November 1980, pp. 145-164.
31. Young, S. J., Description and Use of the Single-Color Transmissometer Plume Diagnostics Code A32CODE, AFRPL-TR-84-48, Air Force Rocket Propulsion Laboratory, Edwards Air Force Base, Calif., August 1984.
32. ISP, ITT Data Programming/Analysis Department, Air Force Rocket Propulsion Laboratory, Edwards Air Force Base, Calif., November 1981.

33. Dawbarn, R. and Kinslow, M., Studies of the Exhaust Products from Solid Propellant Rocket Motors, AEDC-TR-76-49, Arnold Engineering Development Center, Arnold Air Force Station, Tenn., September 1976.
34. Strand, L. D., et. al., "Characterization of Particulates in the Exhaust Plume of Large Solid-Propellant Rockets," Journal of Spacecraft and Rockets", Vol. 18, No. 4, pp 297-305.
35. Young, S. J., Multicolor Inversion Diagnostic for Tactical Motor Plumes, AFRPL-TR-80-30, Air Force Rocket Propulsion Laboratory, Edwards Air Force Base, Calif., May 1980.
36. Limbaugh, C. C., et. al., Nozzle Exit Plane Radiation Diagnostics Measurements of the Improve Transtage Liquid Rocket Injector Program, AEDC-TR-79-29, Arnold Engineering Development Center, Arnold Air Force Station, Tenn., March 1980.
37. Young, S. J., Retrieval of Flow-Field Temperature and Concentrations Low-Visibility Propellant Rocket Exhaust Plumes, AFRPL-TR-82-36, Air Force Rocket Propulsion Laboratory, Edwards Air Force Base, Calif., January 1983.
38. Young, S. J., User's Manual for the Flow-Field Diagnostics Code EMABIC, AFRPL-TR-82-37, Air Force Rocket Propulsion Laboratory, Edwards Air Force Base, Calif., January 1983.

APPENDIX A

A BRIEF REVIEW OF THE THEORETICAL BASIS OF THE AFRPL ROCKET EXHAUST PARTICLE SIZING EFFORT: ASSUMPTIONS AND MODELING

This appendix gives the basis and assumptions germane to the AFRPL particle size data reduction efforts. Only the Mie scattering theory tools needed to understand why the retrieval methods given in the text of this report (Section 3.1) were used are covered here. Whenever concepts or equations are given in this appendix, appropriate references with the necessary detailed explanation or derivations are cited. It must be remembered that the purpose of this appendix is to present a primer on the foundation of light scattering theory only as it applies to the AFRPL plume particle sizing laser transmissometer experiments and not to present a rigid dissertation of Mie theory.

1.0 ROCKET PLUME APPLICATION ASSUMPTIONS

A laser beam transmitting through a particle-laden rocket exhaust flow is but a specialized application of the more general case of electromagnetic radiation traversing any volume of particulates. Two extinction mechanisms are responsible for the portion of energy removed with the passage of the laser electromagnetic radiation through a particulate-loaded medium: particle absorption and particle scattering. These two mechanisms are highly dependent on properties of the particle cloud. The properties include particle size, shape, mass loading, density and refractive index ($m = n + ik(\lambda)$). An additional influencing parameter is the wavelength λ of incident radiation. To model these and other affecting parameters is a difficult undertaking, one which is severely constrained by assumptions in geometry, size distribution, plume density fluctuations and degree of multiple scattering--which are in turn affected by particle size, shape, mass loading, etc. (Refs. A-1 and A-2).

However, some simplifying assumptions (toward an absorption/scattering model and inversion scheme) can be applied to the special case the AFRPL laser transmissometer experiment presents. The polarized, coherent and monochromatic radiation provided by laser radiation provides known values for the incident polarization, electromagnetic radiation coherence, and wavelength parameters. Assuming optically thin plumes further simplifies the model by eliminating consideration of secondary (or multiple) scattering and density fluctuations found with optically thick media. This seems a reasonable caveat given the small particulate mass loading of low visibility plumes (Ref. A-3), especially when coupled with the small scattering focal volume defined by the AFRPL experimental design. To assume that the particle size distribution function (PSDF) $n(r)$ (given in number of particles vs size) is some continuous function also seems reasonable given the current state of knowledge of solid rocket motor plume particle properties (Ref. A-4).

A final and crucial assumption, spherical particles, is subject to some debate. Figure A-1 is a photomicrograph of some Al_2O_3 particles captured at AEDC from a 0.25-lb solid rocket motor which shows that the assumption of rocket exhaust particle sphericity may have some basis (Ref. A-5). However, surface irregularities arising from outer shell deposits, cracks on the surface, and agglomeration in addition to even slight nonuniform particle radii of curvature will render a particle nonspherical, and a cloud of polydisperse nonspherical particles illuminated by laser light may yield fluctuations in the ensuing scattered light coherence and intensity. It has also been contended that the random orientation in such a cloud renders an effective monodisperse cloud of spherical particles with some characteristic surface-equivalent diameter, but this postulate is thus far unsubstantiated (Ref. A-6). What experiments do show is that Mie theory apparently holds for approximately monodisperse nonspherical and randomly oriented particles within the size range we are interested in (Ref. A-7).

Scattering parameters from pure geometries as spheres, cylinders (Ref. A-8), arbitrary axisymmetric bodies (Ref. A-9), and arbitrary smooth convex surfaces of variable curvature (Ref. A-10) have been calculated. Single-scattering from cubic particles has also been measured (Ref. A-11). However, no rigorous analysis of the effects of discontinuities on the particulate

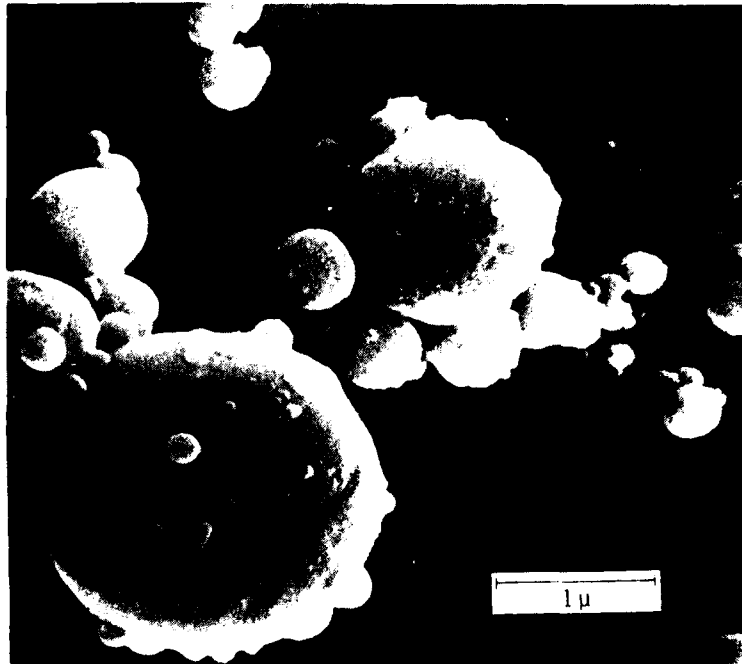


Figure A-1. Al₂O₃ Particles Captured at AEDC from a 0.25-lb
Solid Rocket Motor

surface morphology to light scattering has yet been undertaken. Given a pure geometry (with the other assumptions just outlined), the problem of describing the scattered light from small particles is exactly soluble through Mie theory, which is essentially the solution of Maxwell's equations for a plane electromagnetic wave impinging on a sphere with a known dielectric constant.

2.0 POLARIZATION STATES OF SCATTERED LIGHT (FOR PARTICLE SIZING VIA POLARIZED LIGHT AT DIFFERENT ANGLES)

If polarized laser radiation impinges on a cloud of particles bearing the above assumptions, the intensity I_s of light scattered from a single isotropic particle per unit solid angle per unit of time is

$$I_s(\alpha, m, \theta) = \hat{F}(\alpha, m, \theta) I_0 \quad (\text{A-1})$$

where

I_0 = intensity of the incident light;

α = $2\pi r/\lambda$ = dimensionless particle size parameter;

λ = laser wavelength;

m = the complex index of refraction,

θ = the aspect angle between I_0 and I_s ; and

\hat{F} = the normalized four-by-four scattering transformation matrix (often called a Mueller matrix since it is found via Mueller calculus).

Four Stokes parameters comprise I_0 , and fully describe the incoming electromagnetic radiation and its polarization states. Equation A-1 shows that it is the vector of these Stokes parameters that is transformed from incident to scattered radiation by the Mueller matrix operator \hat{F} (Ref. A-7).

The Stokes parameters, $I(\alpha, m, \theta)$, $Q(\alpha, m, \theta)$, $U(\alpha, m, \theta)$ and $V(\alpha, m, \theta)$, can be further reduced to two intensity distribution functions described by their dimensionless complex amplitudes S_1 and S_2 . These amplitudes are derived in Reference A-7, where

$$|S_1|^2 = \left| \sum_{n=1}^{\infty} \frac{2n+1}{n(n+1)} (a_n \pi_n + b_n \tau_n) \right|^2, \quad (\text{A-2})$$

giving

$$|S_1|^2 = |\text{Re}(S_1) + \text{Im}(S_1)|^2. \quad (\text{A-3})$$

Similarly,

$$|S_2|^2 = \left| \sum_{n=1}^{\infty} \frac{2n+1}{n(n+1)} (a_n \pi_n + b_n \tau_n) \right|^2. \quad (\text{A-4})$$

This can also be reduced to a relation like Equation A-3 where

$$|S_2|^2 = |\operatorname{Re}(S_2) + \operatorname{Im}(S_2)|^2. \quad (\text{A-5})$$

In Equations A-2 through A-5, n = order of electric (a_n) or magnetic (b_n) particle waves, where a_n and b_n are complex functions derived from Bessel functions and are dependent on α and m but not on θ . Conversely, the phase functions π_n and τ_n depend only on θ and use first and second derivatives of Legendre polynomials of order n and argument $\cos \theta$.

$\psi_n(z)$ and $\xi_n(z)$ are the Ricatti-Bessel functions used in determining a_n and b_n where

$$\psi_n(z) = (\frac{1}{2}\pi z)^{\frac{1}{2}} J_{n + \frac{1}{2}}(z) \quad (\text{A-6})$$

and

$$\xi_n(z) = (\frac{1}{2}\pi z) H_{n + \frac{1}{2}}^{(2)} \quad (\text{A-7})$$

$J_{n + \frac{1}{2}}$ and $H_{n + \frac{1}{2}}^{(2)}$ are Bessel functions of the first and third types. Given these definitions,

$$a_n = \frac{\psi'_n(y) + \psi_n(x) - m\psi_n(y)\psi'_n(x)}{\psi_n(y)\xi'_n(x) - m\psi_n(y)\xi_n(x)} \quad (\text{A-8})$$

and

$$b_n = \frac{m\psi'_n(y)\psi_n(\alpha) - \psi_n(y)\psi'_n(\alpha)}{m\psi'_n(y)\xi_n(\alpha) - \psi_n(y)\xi'_n(\alpha)} \quad (\text{A-9})$$

where, as defined earlier,

$$\alpha = 2\pi r/\lambda ;$$

m = complex index of refraction; and

$$y = m\alpha .$$

Reference A-2 provides a derivation for Equations A-8 and A-9.

Also appearing in Equations A-2 and A-4 are π_n and τ_n . Expressed in terms of first and second derivatives of the Legendre polynomials p , they are

$$\pi_n(\cos \theta) = \frac{dP_n(\cos \theta)}{d \cos \theta} \quad (\text{A-10})$$

and

$$\tau_n(\cos \theta) = \cos \pi_n(\cos \theta) - \sin^2 \theta \frac{d\pi_n(\cos \theta)}{d \cos \theta} \quad (\text{A-11})$$

3.0 SINGLE PARTICLE EFFICIENCY FACTORS

We can define efficiency factors for scattering $Q_{sc}(\alpha, m)$ and extinction $Q_e(\alpha, m)$. Efficiency Q is the ratio of energy removed by particle extinction or scattering to its geometric cross section. The Q_{sc} relation is written as

$$Q_{sc} = \frac{\sigma_p}{\pi r^2} \quad (\text{A-12})$$

where

$$\sigma_p = 2\pi \int_0^\pi \sigma_p(\theta) \sin \theta d\theta \quad (\text{A-13})$$

and σ_p represents the total scattering cross section. The differential scattering coefficient is defined as

$$\sigma_p(\theta) = \pi \int_{r_{\min}}^{r_{\max}} \frac{dQ_{sc}}{d\Omega} r^2 n(r) dr \quad (\text{A-14})$$

where Ω is the unit solid angle of scattered light. Using the σ_p relation given in Equation A-13, Equation A-12 becomes

$$Q_{sc} = \frac{2}{r^2} \int_0^\pi \sigma_p(\theta) \sin \theta d\theta \quad (\text{A-15})$$

and can be expressed in discrete form as

$$Q_{sc}(\alpha, m) = \frac{2}{\alpha^2} \sum_{n=1}^{\infty} (2n + 1) \left[|a_n|^2 + |b_n|^2 \right]^2. \quad (A-16)$$

Similarly,

$$Q_e(\alpha, n) = \frac{2}{\alpha^2} \sum_{n=1}^{\infty} (2n + 1) \left[\text{Re}(a_n + b_n) \right]^2. \quad (A-17)$$

Since energy is conserved, the absorption coefficient $Q_{abs}(\alpha, m)$ can be expressed as

$$Q_{abs}(\alpha, m) = Q_e(\alpha, m) - Q_{sc}(\alpha, m). \quad (A-18)$$

From Equations A-12 and A-14, the differential scattering cross section $\sigma_p(\theta)$ is seen to govern the amount of scattered light as a function of scattering angle. This can be made explicit:

$$E(\theta) = \sigma_p(\theta) I_o (W \text{ cm}^{-3} \text{ sr}^{-1}). \quad (A-19)$$

$E(\theta)$ is the differential scattered power per steradian for each unit scattering cross section.

An application of the Mueller transformation matrix to Equations A-1, A-14 and A-18 yields

$$E(\lambda, m, \theta) = \frac{\lambda^2 I_o}{4\pi^2} \int_{r_{\min}}^{r_{\max}} \hat{F}(\alpha, m, \theta) n(r) dr, \quad (A-20)$$

where

$E(\lambda, m, \theta)$ = the angular single-scattered power from a cloud of particles,

$\hat{F}(\lambda, m, \theta)$ = a normalized scattering matrix, and

$n(r)$ = some mean value for the PSDF (see Ref. A-7).

Equation A-20 is recognized as a Fredholm integral of the first kind. Applying a bistatic numerical inversion solution to solve for $n(r)$ and to account for both λ and θ is nontrivial.

4.0 SUMMARY

This appendix reviews the tenants of Mie scattering theory applicable to the AFRPL particle sizing experiment and numerical deconvolution approaches. The theory behind three particle sizing techniques tried at AFRPL--laser polarization, angular intensity and transmission/extinction--was presented in this appendix, albeit without much mention of corresponding numerical techniques. This is the intention; the numerical methods are given in the course of the report (Section 3.1). Underlying assumptions pertaining specifically to the AFRPL Mie scattering experiment were also given to further constrain the extent of this review. Full descriptions and derivations of light scattering theory, while interesting, are beyond the intention of the appendix; they are, however, included in the references.

REFERENCES

- A-1. Van de Hulst, H. C., Light Scattering by Small Particles, John Wiley and Sons, New York, 1957.
- A-2. Bohren, C. F., and Huffman, D. R., Absorption and Scattering of Light by Small Particles, John Wiley and Sons, New York, 1983.
- A-3. Young, S. J., Retrieval of Flow-Field Gas Temperature and Concentration of Low-Visibility Rocket Exhaust Plumes, AFRPL-TR-82-13, Aerospace Corporation, March 1982.
- A-4. Konopka, W., Reed, R. A., and Calia, V. S., Infrared Optical Properties of Al₂O₃ IUS Motor (DS8C) Exhaust Particles, AEDC-TR-83-19, Arnold Engineering Development Center, Arnold Air Force Station, Tenn., April 1983.
- A-5. Dawbarn, R., and Kinslow, M., Studies of the Exhaust Products from Solid Propellant Rocket Motors, AEDC-TR-76-49, Arnold Engineering Development Center, Arnold Air Force Station, Tenn., September 1976.
- A-6. Hirleman, E. D., Private communication concerning current research on ensemble particle measurement techniques, Professor Laser Diagnostics Laboratory, Mechanical Engineering Department, Arizona State University, Tempe, Ariz., 26 September 1983.
- A-7. Pinnick, R. G., Carroll, D. E., and Hofmann, D. J., "Polarized Light Scattered from Monodisperse Randomly Oriented Nonspherical Aerosol Particles: Measurements." Applied Optics, Vol. 15, 1976, pp. 384-393.

AD-A157 249

EXHAUST PLUME MEASUREMENTS OF 15-POUND BATES (BALLISTIC 2/2
TEST AND EVALUATI. (U) AIR FORCE ROCKET PROPULSION LAB
EDWARDS AFB CA J A MISENER ET AL. JUN 85

UNCLASSIFIED

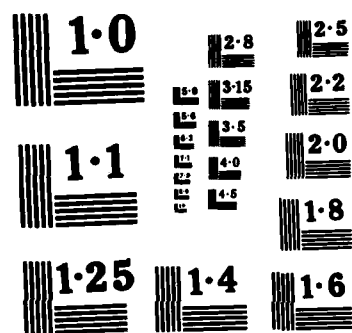
AFRPL-TR-85-013

F/G 21/9.2 NL

END

FORMED

DATA



NATIONAL BUREAU OF STANDARDS
MICROCOPY RESOLUTION TEST CHART

A-8. Kerker, M., The Scattering of Light and Other Electromagnetic Radiation, Academic Press, New York, 1969.

A-9. Barber, P., and Yeh, C., "Scattering of Electromagnetic Waves by Arbitrary Shaped Dielectric Bodies." Applied Optics, Vol. 14, 1975, pp. 2864-2872.

A-10. Ott, R. H., Scattering by a Parabolic Cylinder--A Uniform Asymptotic Expansion, SD-TR-84-31, Space Division, Los Angeles Air Force Station, Calif., August 1984.

A-11. Tang, I. N., and Munkelwitz, H. R., "Optical Size Determination for Single Cubic Particles Suspended in a Laser Beam." Journal of Colloid and Interface Science, Vol. 63, No. 2, February 1978, pp. 297-303.

APPENDIX B

A BRIEF REVIEW OF THE THEORETICAL BASIS OF THE AFRPL INFRARED EMISSION/ABSORPTION EXPERIMENT TO RETRIEVE PLUME SPECIES TEMPERATURES AND PARTIAL PRESSURES: ASSUMPTIONS AND MODELING

This appendix addresses the underlying theory behind the AFRPL BATES plume infrared emission/absorption (IR-E/A) experiment. Neither a rigid derivation of applicable radiation models, a primer on the numerical inversion techniques nor a description of the apparatus employed with the AFRPL experiment is partaken here; radiation models are derived and discussed in detail elsewhere (Refs. B-1 and B-2), the numerical deconvolution procedure is given in the text of this report (Section 3.3) and the instrumentation configuration is also described within the report (Section 2.4). The intent with this appendix is instead to familiarize the reader on the radiative transfer relationships used to determine values for plume species temperature and partial pressure profiles through application of emission and absorption spectroscopy. Three progressively realistic radiative transfer models will be discussed: the particle-free homogeneous gas case, the particle-free inhomogeneous axisymmetric gas case and the particle-laden inhomogeneous axisymmetric gas case.

1.0 TEMPERATURE AND PARTIAL PRESSURES FROM A PARTICLE-FREE HOMOGENEOUS GAS

This is the simplest case for plume IR-E/A analysis, although the restrictions imposed by assuming the absence of radiating and scattering particles and also assuming a plume gas column with no density fluctuations make the model unrealistic for particle-laden flows. Nonetheless, the first-order species-independent analysis will familiarize the reader with the necessary basis for the more stressing band model inversion schemes.

If the plume is at an equilibrium temperature T^P , its monochromatic radiance $L^P(\lambda, T^P)$ is given by the relation,

$$L_{\lambda}^P(\lambda, T^P) = \epsilon_{\lambda}^P L_{\lambda}^{BB}(\lambda, T^P) \quad (B-1)$$

where the wavelength λ and plume temperature T^P are constant and where:

ϵ^P = monochromatic emissivity of the plume and

$L_{\lambda}^{BB}(\lambda, T^P)$ = monochromatic blackbody radiance.

This blackbody radiance is governed by the Planck function,

$$L_{\lambda}^{BB}(\lambda, T^P) = \frac{c_1}{\lambda^5 (e^{c_2/\lambda T^P} - 1)} \quad (B-2)$$

where

$$c_1 = 2\pi c^2 h = 3.7419 \times 10^{-12} \text{ Wcm}^{-2} \quad \text{and}$$

$$c_2 = hc/K_b = 1.439 \text{ cmK} .$$

Furthermore, Kirchoff's law defines the equivalence,

$$\epsilon^P = \alpha_{\lambda}^P = 1 - \tau_{\lambda}^P \quad (B-3)$$

where

α_{λ}^P = monochromatic absorptivity of the plume and

τ_{λ}^P = monochromatic transmissivity of the plume.

Combining Equations B-1, B-2 and B-3 yields an expression for the plume temperature

$$T^P = \frac{c_2}{\frac{\ln \frac{c_1 (1 - \tau^P)}{L^P \lambda^5} - 1}{\lambda^5}} \quad (B-4)$$

as a function of monochromatic wavelength λ , plume transmittance τ^P and plume radiance L^P . Note that T^P is independent of λ .

According to the Beer-Lambert principle, a specific relation exists between transmittance and partial pressure for purely absorbent low concentration media, i. e.,

$$\ln \tau_{\lambda}^P = -c^P P K_{\lambda}^P(c, p, T)L \quad (B-5)$$

where

c^P = concentration;

P = pressure of the plume;

$K_{\lambda}^P(c, p, T)$ = monochromatic absorption coefficient of the plume ($\text{cm}^{-1} \text{ atm}^{-1}$); and

L = length of transmitting path s through any arbitrary plume line of sight.

The plume monochromatic concentration c^P is easily derivable from Equation B-5, given some input value for static pressure. In the least case, the partial pressure can be extracted from the above equation.

2.0 TEMPERATURE AND PARTIAL PRESSURES PROFILES FROM A PARTICLE-FREE INHOMOGENEOUS AXISYMMETRIC GAS

For a line of sight s through a nonuniform and gaseous plume medium containing temperature and pressure gradients as illustrated in Figure B-1, the resulting monochromatic plume radiance L^P can be expressed in simplified form as

$$L^P(\lambda, T^P) = \int_0^L \frac{L_{\lambda}^{BB}(s) + L_{\lambda}^E(s)}{(L_{\lambda}^{BB}(s) + L_{\lambda}^E(s))} \frac{d\tau_{\lambda}^P(s)}{ds} ds \quad (B-6)$$

where

L = distance along line of sight s ,

$L_{\lambda}^{BB}(s)$ = monochromatic blackbody radiance at s ,

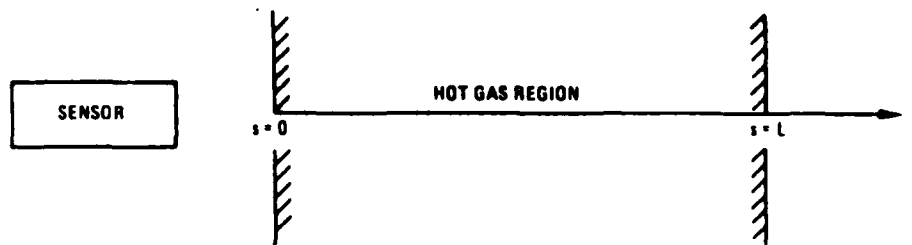


Figure B-1. Gas-Only Flow Optical Geometry

$L_{\lambda}^E(s)$ = monochromatic external radiance incident on plume boundary and

$\overline{\tau_{\lambda}^P(s)}$ = average monochromatic transmittance of the plume at s .

Substituting Equation B-2 into Equation B-6 and solving for the plume temperature profile $T^P(s)$ requires some numerical inversion to solve for $L_{\lambda}^{BB}(s)$ (Ref. B-2). $T^P(s)$ is again independent of λ .

Using the Beer-Lambert absorption law, transmittance can now be expressed as

$$\overline{\text{Int} \tau_{\lambda}^P(s)} = \int_0^L c^P(s) p^P(s) K_{\lambda}^P(s) y_{\lambda}^P(s) ds. \quad (\text{B-7})$$

with

$K_{\lambda}^P(s)$ = monochromatic absorption coefficient of the plume and

$y_{\lambda}^P(s)$ = band model function.

Equation B-7 differs from Equation B-5, as terms are written as functions of the line of sight s ; this is a concession to the plume inhomogeneity.

The band model function $y_{\lambda}^P(s)$ is necessarily inserted in Equation B-7 to describe plume species band system structure since they are highly sensitive to fluctuations in temperature, partial pressure and gas density.

The band model must have line-by-line resolution to simulate the plume species' radiative transfer (most notably with the primary combustion gases, H₂O and CO₂) because of these sensitivities. Available band models fit empirical data very well (Refs. B-3 and B-4). The particular function $y_{\lambda}^P(s)$ used here arises from the Malkmus statistical band model and the calculations are carried out with a Curtis-Goodson nonuniformity approach fully described in Reference B-4. This function accounts for the difference between the Lund and Beer-Lambert absorption models and is highly dependent on postulated spectral line shapes.

The numerical method to retrieve concentration and pressure profiles from a model reflected by Equation B-7 is discussed in the text of this report (Section 2.4) and detailed in Reference B-2.

3.0 TEMPERATURE AND PARTIAL PRESSURE PROFILES FROM A PARTICLE-LADEN INHOMOGENEOUS AXISYMMETRIC GAS

Coupling the gas-only observed radiance relation (Equation B-6) with single scattering effects of particles within the plume flowfield yields a revised monochromatic plume and radiance L^P expressed as

$$L^P(\lambda, T^P) = \int_0^L \frac{L^{BB}(s) + L^E(s)}{(L^{BB}(s) + L^E(s))} \frac{d\tau^P(s)}{ds} ds \int_0^{4\pi} \alpha(s) \beta(s) d\Omega \quad (B-8)$$

where

$\alpha(s)$ = particle absorption cross section and

$\beta(s)$ = particle scattering cross section.

These cross section terms are integrated over the solid angle defined by the scattering angles θ and ϕ shown in Figure B-2.

Equation B-7 can be likewise modified to include particle effects. The relation governing plume transmittance for a two-phase system is

$$\overline{\ln \tau^P(s)} = - \int_0^L c^P(s) p^P(s) k_{\lambda}^P(s) y_{\lambda}^P(s) ds \int_0^{4\pi} \alpha(s) \beta(s) ds. \quad (B-9)$$

The numerical algorithm to be used with Equation B-9 is very similar to that for Equation B-7. Theory and premises behind the single particle light scattering theory used in Equations B-8 and B-9 are discussed in Appendix A of this report.

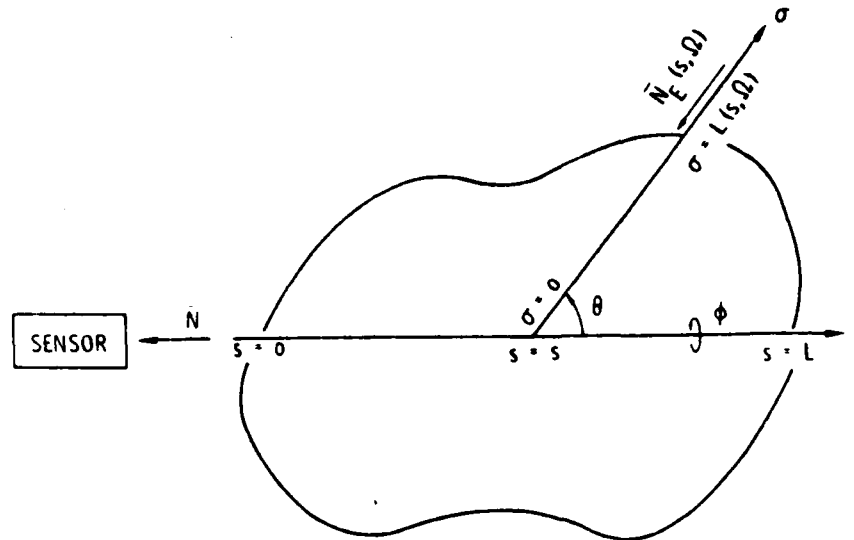


Figure B-2. Gas-Particle Flow Optical Geometry

REFERENCES

- B-1. Young, S. J., User's Manual for the Plume Signature Code EAPROF, AFRPL-TR-81-08, Aerospace Corporation, January 1981.
- B-2. Young, S. J., Retrieval of Flow-Field Gas Temperature and Concentration of Low-Visibility Rocket Exhaust Plumes, AFRPL-TR-82-13, Aerospace Corporation, March 1982.
- B-3. Ludwig, C. B., Malkmus, W., Beardon, J. E., and Thomson, J. A. L., Handbook of Infrared Radiation from Combustion Gases, NASA SP-3080, Marshall Space Flight Center, Huntsville, Ala., 1973.
- B-4. Young, S. J., "Nonisothermal Band Model Theory," Journal of Quantitative Spectroscopy and Radiative Transfer, Vol. 18, No.1, pp. 1-28, 1977.

APPENDIX C

A BRIEF REVIEW OF THE ADAPTIVE NOISE CANCELLING SIGNAL PROCESSING TECHNIQUE AS APPLIED AT AFRPL

Difficulty in reducing the noisy scattering detector data was cited in the text of the report (Section 3.1) as a practical experimental problem encountered in addition to the analytical and computational difficulties encountered with the particle size distribution retrieval algorithm. Despite the deleterious effects of not having an accurate size distribution retrieval code, a signal processing scheme to overcome low scattering detector signal-to-noise ratios was still pursued. A major reason for this was to provide a potentially useful processing technique for future AFRPL data reduction efforts (e. g., as described in the report under Section 3.2).

This appendix describes the concepts and application of a signal processing technique called adaptive noise canceling and shows result of its application to data from a scattering detector the signal test run.

1.0 THE CONCEPT OF ADAPTIVE NOISE CANCELLING (REF. C-1)

Figure C-1 describes the structure of the adaptive noise canceling system used in the AFRPL application to reduce the additive noise that corrupts desired scattering detector signals. The noise cancellation can be carried out in real time or during the post processing of the recorded signal. For the system to work effectively the following conditions are necessary:

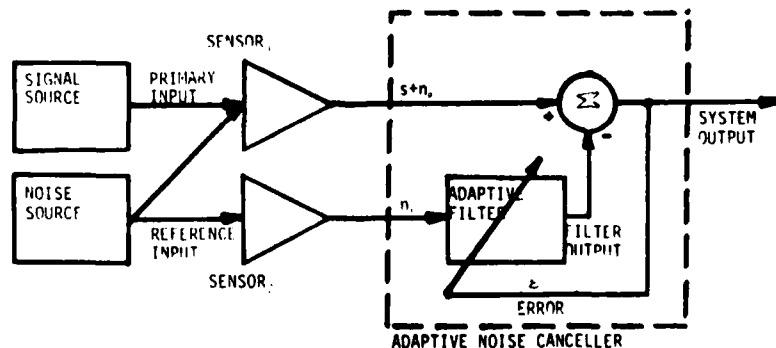


Figure C-1. An Adaptive Noise Cancelling System

(1) the desired signal s is corrupted by an additive noise n_0 uncorrelated with the signal s ; and

(2) availability of a noise n_1 uncorrelated with s but correlated in some unknown way with the noise n_0 .

Note that for the signals encountered with the scattering detector case, (1) is a reasonable assumption, and the noise signal n_1 of condition (2) can be recorded during the firing.

The idea of the adaptive noise canceler is to filter the noise signal n_1 to produce an output y that is as close a replica as possible of n_0 by dynamically and automatically adjusting the filter's own impulse response. The adjustments are carried out through an algorithm that responds to an error signal dependent, among other things, on the filter's output. Thus, with a proper algorithm the filter can operate under changing conditions and can readjust itself continuously to minimize the error signal in the Least Mean Square (LMS) sense.

To justify how the system works assume that s , n_0 , n_1 are statistically stationary and each has a mean of zero. Consider the system output z :

$$z = s + n_0 - y. \quad (\text{C-1})$$

Squaring and taking expectations gives:

$$E(z^2) = E(s^2) + E(n_0 - y)^2 + 2E(s(n_0 - y)). \quad (\text{C-2a})$$

But $E(S(n_0 - y)) = 0$ because s is uncorrelated with n_0 and with y . Hence,

$$E(z^2) = E(s^2) + E(n_0 - y)^2. \quad (\text{C-2b})$$

From Equation (C-2), note that the independent signal power $E(s^2)$ will be unaffected as the filter is adjusted to minimize the output power $E(z^2)$. Accordingly, the minimum output power can be expressed as

$$\min (E/z^2) = E(s^2) + \min (E(n_0 - y)^2). \quad (C-3)$$

Observe that when the filter is adjusted so that $E(z^2)$ is minimized, $E(n_0 - y)^2$ is also minimized. The filter output y can be then considered a best least square estimate of the primary noise n_0 .

The output z will contain the signal s plus noise. From Equation C-1, the output noise is given by $n_0 - y$. Since minimizing the output power $E(z^2)$ also minimizes the output noise power $E(n_0 - y)^2$, minimizing the total output power minimizes the output noise power. Since the signal in the output remains constant, minimizing the total output power therefore maximizes the output signal-to-noise ratio.

2.0 APPLICATION

To determine the usefulness of the adaptive noise canceling concept for AFRPL scattering detector data, we processed data from a scattering detector channel (SD1) taken in BATES 242B-015 firing.

Figure C-2 shows the signal trace from SD1 collected with AFRPL data Acquisition and Control System (DACS). The trace clearly shows a dominant effect of the noise in the post-ignition data.

To implement the adaptive scheme shown in Figure C-1, a reference signal correlated to the noise in the SD1 signal should be recorded during the entire test. But in the AFRPL laser scattering experiment such signals were not recorded because applying the scheme to the data was not considered at the time of the experiment. Under the situation, we generated an a-posteriori reference noise signal based on the following assumptions:

- (1) the pre-ignition signal shown in Figure C-2 is a noise that corrupts additively the desired signal; and

- (2) the pre-ignition noise characteristic remains the same during the entire firing.

Using the above assumptions, we generated the reference noise signal shown in Figure C-3 by a periodic extension of the pre-ignition signal which was long enough to match the entire SDI signal.

Figure C-4 shows the adaptive noise canceler output. As can be seen, the adaptive filter rapidly adapts to the noise to produce zero-level pre-ignition signal and continues working in the post-ignition period to produce output signal that is considerably different from the original SDI signal.

It is impossible to judge quantitatively how good the result is because we do not know for certain how realistic the a-posteriori reference signal is. However, if in the future we plan to use such a signal processing technique from the start of an experiment, we can record a more realistic noise signal correlated to the corrupting noise and obtain a final signal with much less noise. Although we have only shown results from one scatter detector channels there is a dramatic signal-to-noise improvement over the unconditioned signal.

REFERENCE

- C-1. Widrow, B. et. al., "Adaptive Noise Cancelling: Principles and Applications" Proceedings of the IEEE, Vol. 63, No. 12, December 1975, pp. 1692-1716.

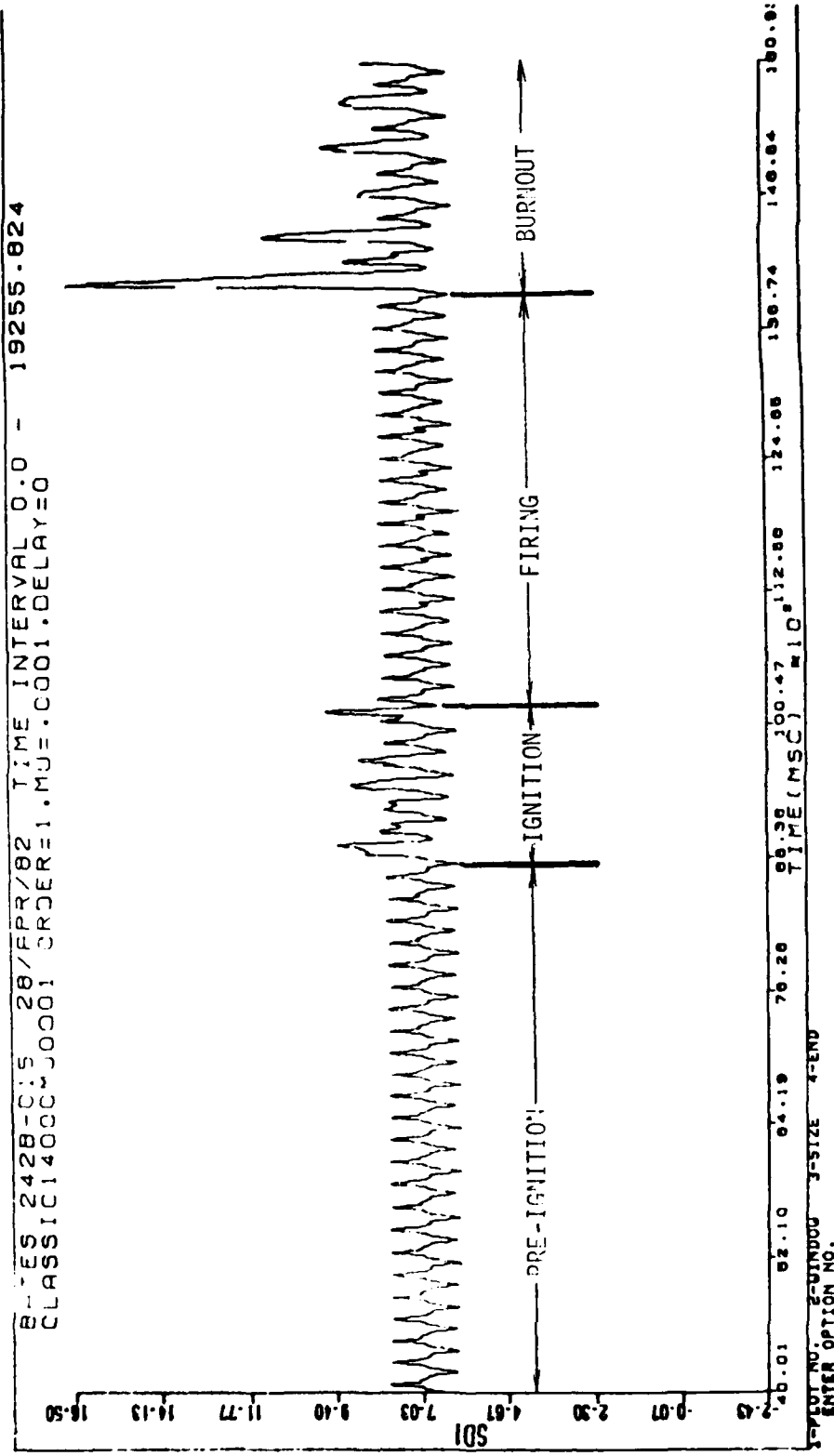


Figure C-2. SDI Signal.

BATES 2428-015 28/APR/82 TIME INTERVAL 0.0 - 19255.824
 CLASSIC14000MU0001 ORDER=1.MU=.0001.DELAY=0

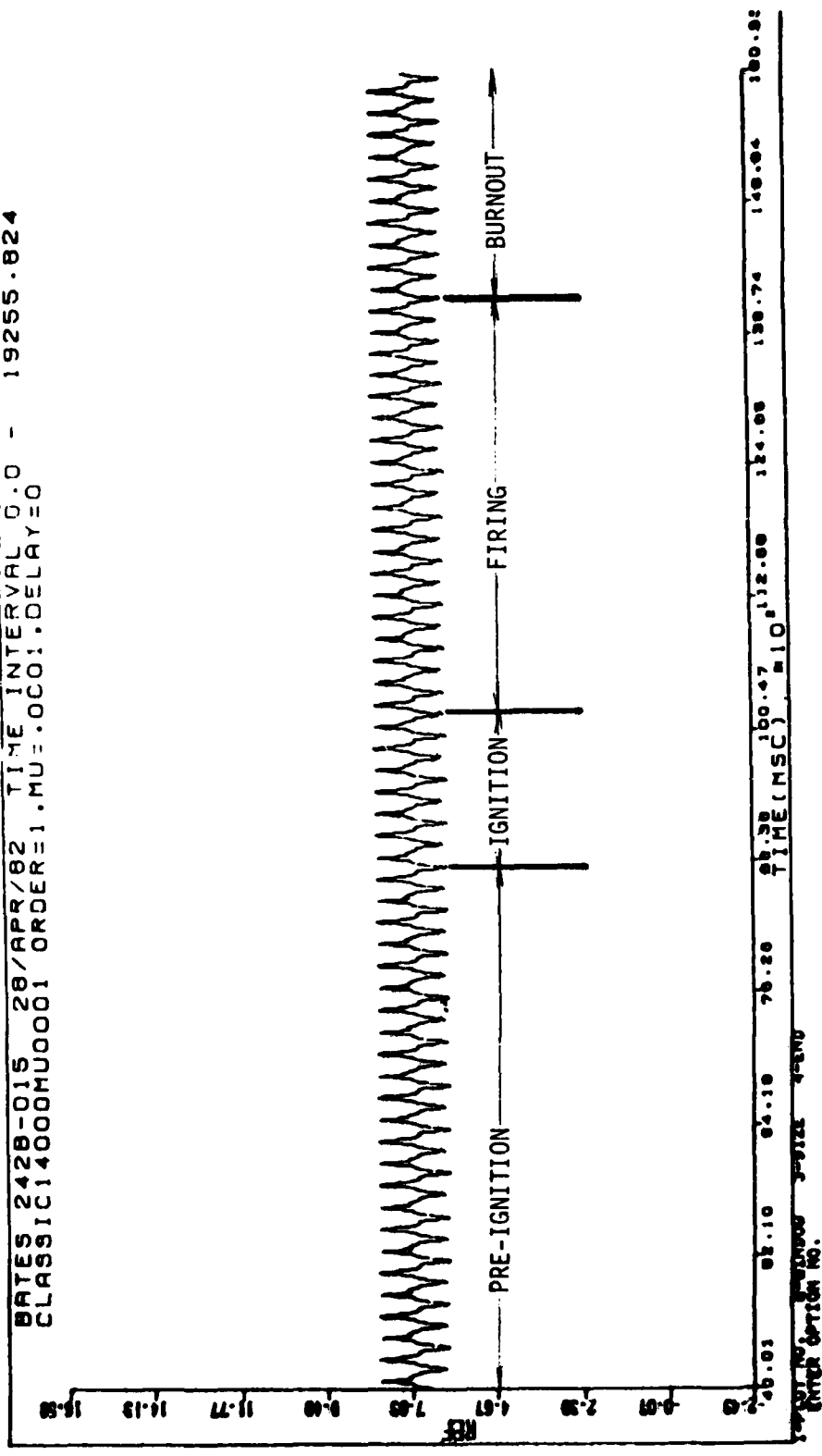


Figure C-3. A-Posteriori Reference Signal.

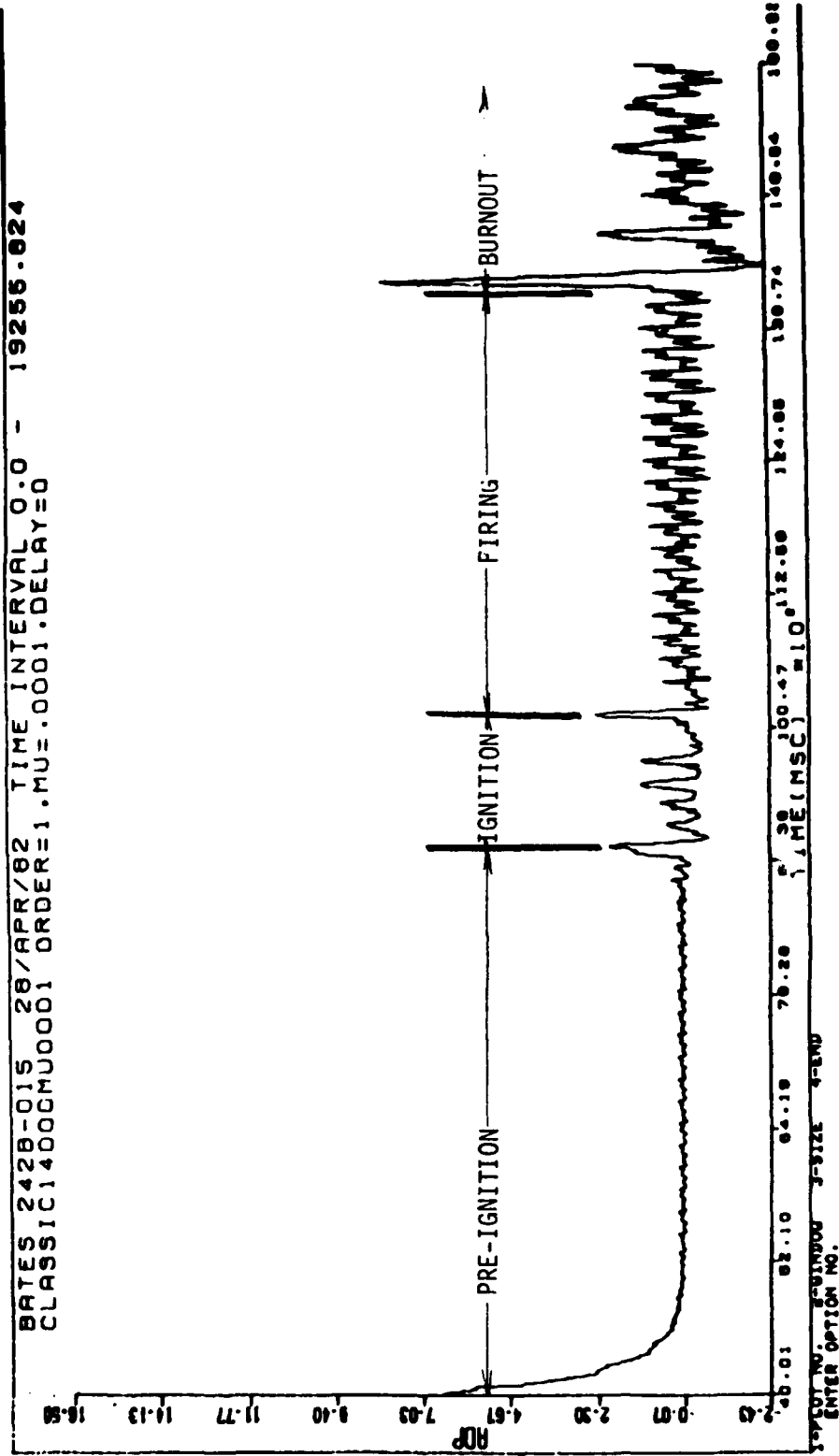


Figure C-4. Adaptive Noise Canceling System Output.

APPENDIX D

DESCRIPTION OF THE AFRPL PLUME RADIOMETRIC MEASUREMENTS PLANNED FOR 1984

This appendix addresses the few follow-on and ancillary plume radiometric measurements to be done at AFRPL before the major follow-on project described in Section 4.2. Several reduced smoke GAP polymer propellants are scheduled to be fired at the same Pad 5a of Experimental Area 1-32 where the other measurements were taken. A radiometer has been added to the AFRPL plume instrumentation ensemble described in the report to measure plume afterburning. Once these measurements are taken they are to serve as the basis for an AFRPL plume infrared signature data base to be used eventually to evaluate plume infrared signature. Follow-on efforts mentioned in Section 2.2 of the report will use more instruments to measure plume infrared signatures, providing a number of options including a variety of aspect angles, field of views (FOVs), optical bandpasses and spectral resolutions.

For this particular effort, however, a Barnes Model 12-880 infrared radiometer filtered at a 2.395 - 2.715 μm passband but with a full width-half maximum (FWHM) bandpass of 2.490 - 2.665 μm . This FWHM bandpass falls within the nonisobetic H_2O spectrum between 2.38 - 2.63 μm identified by Young (Ref. D-1) for the elevated temperatures and pressures encountered with BATES-type motors. Hence, the radiometer is essentially a plume constituent H_2O sensing device.

The radiometer has a pyroelectric detector with a chopper and internal reference cavity design. The 10-90% response time of this system is 50 ms. The normalized spectral response with the detector and 2.395 - 2.715 μm filter combination is shown in Figure D-1. These are the manufacturers' data.

The reason for pointing the radiometer at the plume afterburning region is that most of the plume's radiation emanates from this area, and the radiometer's 20° FOV combined with the limited space within the test pad

LITa03, KRSS, Co, 2 DEGREES, 2.59 MICROM/POS C
DEAT, S/N 132, 3/29/82

INITIAL LAMBDA (MICRONS) = 2.395
FINAL LAMBDA (MICRONS) = 2.715
DELTA LAMBDA (MICRONS) = .005

MAXIMUM THRUPT = .389

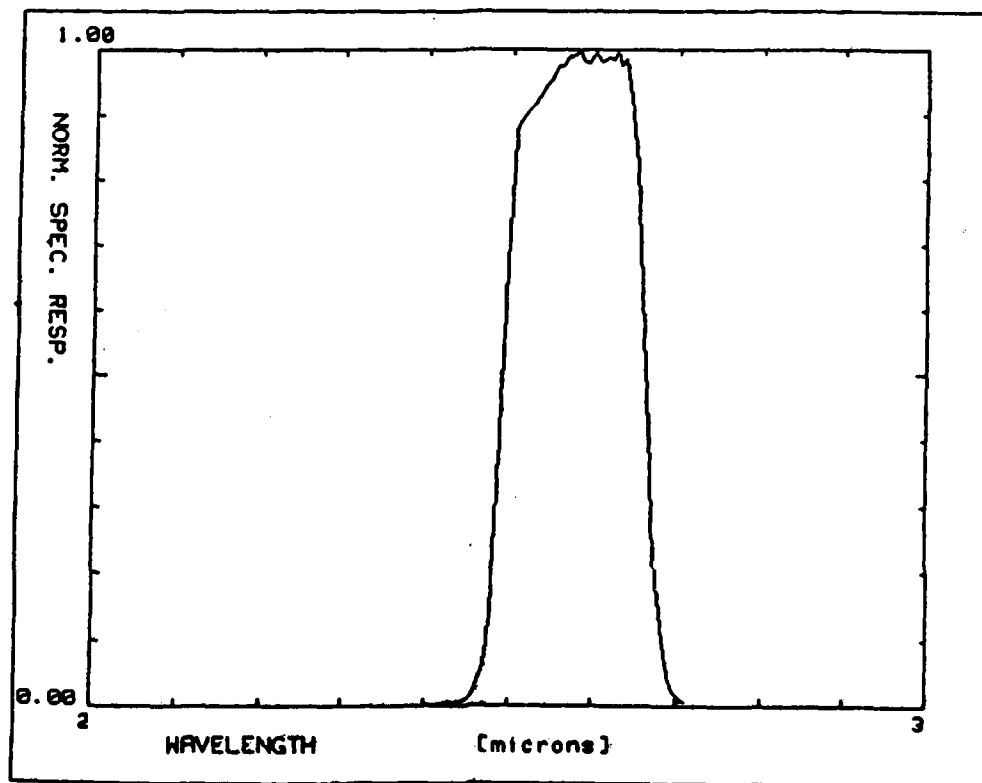


Figure D-1. Radiometer Normalized Spectral Response

necessarily constrained the measurement to only a certain portion of the plume. The radiometer was positioned 20.2 feet from the BATES motor exit plane and oriented at a 42° aspect angle from the motor centerline, away from the plume flow. The afterburning region was identified by applying the JANNAF Standardized Infrared Radiation Model (SIRRM) plume predictive code to individual BATES motor propellant, nozzle and flowfield inputs, and running the filter integration bandpass module in the spatial radiant intensity mode (Ref. D-2). Figure D-2 is an example of the SIRRM code output when run this way.

Pointing the radiometer is a relatively simple operation, done with a high intensity source placed at the plume centerline. In the case with Figure D-2, the source would be placed 2 m downstream from the motor exit plane.

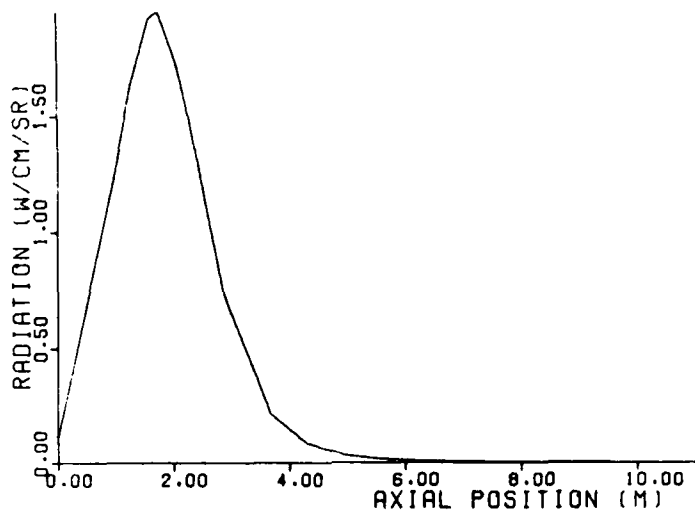


Figure D-2. In-Band Radiant Intensity vs Axial Position Along 15-lb BATES Motor Plume Centerline

At this writing no reportable data had been taken via the radiometer channel for the five reduced smoke static firings due to problems in the radiometer's output electronics and data acquisition system. However, at least 15 more test firings plus other AFRPL targets of opportunity are expected to occur soon. The following calibration section addresses how pre-firing preparations are made.

CALIBRATION

The calibration techniques applied to these measurements are detailed in Reference D-3. Essentially, an extended blackbody source calibration technique was used to calculate the calibration transfer function in the absolute responsivity calibration. Field of view mapping and background and noise level determination steps were undertaken in addition to consideration of out-of-bound rejection. These error sources plus those enumerated in

Section 2.4.3 of this report are embedded in a calibration uncertainty factor. This uncertainty factor gives the total bias error bar associated with the radiometer data. Because each of the firings was unique, no random error uncertainties could be attached to the total error margin.

REFERENCES

D-1. Young, S. J., Inversion of Plume Radiance and Absorptance Data for Temperature and Concentration, Appendix A, AFRPL-TR-78-60, Aerospace Corporation, September 1978.

D-2. Ludwig, C. B., et al. Handbook of the Standardized Infrared Radiation Model (SIRRM), Volume I: Technical Manual, AFRPL-TR-81-61, Photon Research, August 1981.

D-3. Misener, J. A., Calibration of BATES Motor Firing Radiometric Measurements, AFRPL-TM-84-34, Air Force Rocket Propulsion Laboratory, Edwards Air Force Base, Calif., September 1984.

END

FILMED

9-85

DTIC